GRAPHENE NANOMATERIAL BASED FLUORESCENCE RESONANCE ENERGY TRANSFER (FRET) BIOSENSOR FOR BIOMOLECULE AND CELL DETECTION

SHI JINGYU

M. Phil

The Hong Kong Polytechnic University

2015

The Hong Kong Polytechnic University

Interdisciplinary Division of Biomedical Engineering

Graphene Nanomaterial Based Fluorescence Resonance Energy Transfer (FRET) Biosensor for Biomolecule and Cell Detection

SHI Jingyu

A thesis submitted in partial fulfillment of the requirements for the degree of Master of Philosophy

January 2015

Certificate of originality

I hereby declare that this thesis is my own work and that, to the best of my knowledge and belief, it reproduces no material previously published or written, nor material that has been accepted for the award of any other degree or diploma, except where due acknowledgement has been made in the text.

SHI Jingyu

Abstract

Nowadays biodetection is popular in many fields, such as food safety, medical diagnostics, drug discovery and environment detection. Conventional biodetection methods including immunological assay (ELISA) and nucleic acid based assays (PCR) are primarily hampered by time-consuming and labor-intensive procedures with relatively low sensitivity. Therefore, the development of rapid, direct and sensitive biodetection methods is of great importance. Fluorescence resonance energy transfer (FRET) is a direct and sensitive method, which can detect biological phenomena in nanoscale. However, traditional based FRET is mainly based on organic fluorophores which have short fluorescence life time and low stability.

The research in this dissertation is focused on developing graphene nanomaterial based fluorescence resonance energy transfer (FRET) biosensors for rapid and ultrasensitive detection of various biological species, including staphylococcus aureus (*S. aureus*) mecA gene sequence, bacterial protein toxin and circulating tumor cells in breast cancer (MCF-7).The whole study includes three parts.

The first part of this thesis is focused on development of a FRET biosensor based on graphene quantum dots (GQDs) and gold nanoparticles (AuNPs) for rapid and sensitive detection of specific mecA gene sequence of staphylococcus aureus. This FRET biosensor platform is realized by immobilization of capture probes on GQDs and conjugation of reporter probes on AuNPs. Target oligonucleotides then co-hybridize with capture probes and reporter probes to form a sandwich structure which brings GQDs and AuNPs to close proximity to trigger FRET effect. The fluorescence signals

before and after addition of targets are measured and the fluorescence quenching efficiency could reach around 87%. The limit of detection (LOD) of this FRET biosensor was around 1 nM for *S. aureus* gene detection. Experiments with both single-base mismatched oligonucleotides and double-base mismatched oligonucleotides demonstrated the specificity of this FRET biosensor.

The second part of this study describes a graphene oxide (GO) based fluorescence resonance energy transfer (FRET) biosensor for ultrasensitive detection of botulinum neurotoxin serotype A light chain (BoNT-LcA) enzymatic activity. A green fluorescence protein (GFP) modified SNAP-25 peptide substrate (SNAP-25-GFP) is optimally designed and synthesized with the centralized recognition/cleavage sites. BoNT-LcA can specifically cleave SNAP-25-GFP substrate immobilized on GO surface, releasing the fragment connected with GFP into the solution. By monitoring fluorescence signal recovery, the target BoNT-LcA protease activity is detected sensitively and selectively with the linear detection range from 1 fg/mL to 1 pg/mL. The LOD for BoNT-LcA is around 1 fg/ml. Moreover, stability and reliability of this GO-peptide based FRET biosensor is also investigated.

In the third part of this dissertation, a fluorescence labeled epithelial cell adhesion molecule (EpCAM) aptamer/GO nanocomplex based FRET biosensor is developed for sensitive detection of breast cancer circulating tumor cells (CTCs).The FRET sensing platform is constructed by absorption of FAM-EpCAM aptamer (donor) on GO (acceptor) surface via π-π stacking interaction. Target MCF-7 cancer cells can be detected through affinity interaction between FAM-EpCAM aptamer and EpCAM

protein that expressed on the surface membrane of MCF-7 cells, resulting in the release of FAM-EpCAM aptamer from GO surface. By monitoring fluorescence signal recovery, the target MCF-7 cancer cells can be detected sensitively and selectively.

List of Publications

Journal Papers

[1] **Jingyu Shi**, Chunyu Chan, Yukting Pang, Weiwei Ye, Feng Tian, Jing Lyu, Yu Zhang, and Mo Yang*. A fluorescence resonance energy transfer (FRET) biosensor based on graphene quantum dots (GQDs) and gold nanoparticles (AuNPs) for the detection of mecA gene sequence of staphylococcus aureus. Biosensors and Bioelectronics, 2015, 67: 595–600.

[2] **Jingyu Shi**, Jiubiao Guo, Zhongxun Bai, Chunyu Chan, Xuan Liu, Weiwei Ye, Jianhua Hao, Sheng Chen, and Mo Yang*. A graphene oxide based fluorescence resonance energy transfer (FRET) biosensor for ultrasensitive detection of botulinum neurotoxin A (BoNT/A) enzymatic activity. Biosensors and Bioelectronics, 2015, 65: 238-244.

[3] Weiwei Ye, **Jingyu Shi**, Chunyu Chan, Yu Zhang, and Mo Yang*. A nanoporous membrane based impedance sensing platform for DNA sensing with gold nanoparticle amplification. Sensors and Actuators B: Chemical, 2014, 193: 877-882.

[4] Baojian Xu, Weiwei Ye, Yu Zhang, **Jingyu Shi**, Chunyu Chan, Xiaoqiang Yao, and Mo Yang*. A hydrophilic polymer based microfluidic system with planar patch clamp electrode array for electrophysiological measurement from cells. Biosensors and Bioelectronics, 2014, 53: 187-192.

Conference papers

[1] Weiwei Ye, **Jingyu Shi**, Chunyu Chan, Lidan Xiao, and Mo Yang*. "Nanoporous alumina membrane and nanoparticle based microfluidic sensing platform for direct DNA detection." Transducers 2013, Barcelona, Spain, 16-20 June 2013.

Acknowledgement

I would like to express my sincere gratitude to my supervisor, Dr. Mo Yang, for his invaluable advice, patient guidance, sustained encouragement and continuous support throughout my M. Phil study. I would not be possible to overcome the hurdles of my research without the insightful suggestions from him.

I wish to give my thanks to Dr. Jianhua Hao in Department of Applied Physics in the Hong Kong Polytechnic University for providing detection instrument. I also want to thank Dr. Sheng Chen in Department of Applied Biology & Chemical Technology in the Hong Kong Polytechnic University for protein synthesis and preparation.

I would like to thank my collaborators, Gongxun Bai from Department of Applied Physics, Jiubiao Guo from Applied Biology & Chemical Technology and Xuan Liu from Institute of Textiles & Clothing in the Hong Kong Polytechnic University. I am grateful to all the members of BME for their help, especially those in S106. I would like to thank Weiwei Ye, Chan Chun Yu, Feng Tian, Jing Lyu and Cheng Liu for inspiring discussions and suggestions on my work and life. My sincere thanks also go to my friend Jiajing Wu, Longjing Lin and Leyan Lei for their friendship and help during my stay in Hong Kong.

The financial support provided by B-Q29F is greatly acknowledged. Last but not least, I would like to thank my parents for their love and support throughout my life.

Table of Contents

List of Figures

List of Abbreviations

2-dimensional	2D
Adenine	A
Anti-Stokes photoluminescence	ASPL
Atomic force microscopy	AFM
Botulinum neurotoxin serotype A light chain	BoNT-LcA
Chloroauric acid	HAuCl4
Cytosine	C
Deionized water	DI water
Deoxyribonucleic acid	DNA
Dithiothreitol	DTT
DNA-functionalized AuNPs	AuNPs-ssDNA
DNA-functionalized GQDs	GQDs-ssDNA
Double-strand DNA	dsDNA
Energy dispersive X-ray spectroscopy	EDX
Enzyme-linked immunoabsorbent assay	ELISA
Epithelial cell adhesion molecule	EpCAM
Escherichia coli	E. coli
Fluorescent intensity after quenching effect	F_q
Fluorescent intensity before quenching effect	F_0
Fluorescent intensity of recovery	F_r
Fluorophore carboxy fluorescein	FAM
Förster resonance energy transfer / fluorescence	FRET

resonance energy transfer	
Fourier transform infrared spectrum	FTIR
Gold nanoparticles	AuNPs
Graphene oxide quantum dots	GOQDs
Graphene quantum dots	GQDs
Green fluorescence protein	GFP
Guanine	G
High resolution TEM	HRTEM
Highest occupied molecular orbital	HOMO
Hydrochloric acid	HCl
Immunomagnetic separation	IMS
Integrated DNA Technologies incorporated	IDT Inc.
Limit of detection	LOD
Lowest unoccupied molecular orbital	LUMO
Methylthiazolyldiphenyl-tetrazolium bromide	MTT
Molecular beacons	MBs
N-(3-dimethylaminopropyl)-N’-ethyl-carbodiimide	EDC
N, N-dimethylformamide	DMF
Nanoparticle	NP
Near-infrared	NIR
N-hydroxysuccinimide	NHS
Phosphate buffer solution	PBS
Photoluminescence	PL

Polymerase chain reaction	PCR
Quantum dots	QDs
Scanning electron microscopy	SEM
Single-strand DNA	ssDNA
Staphylococcus aureus	*S. aureus*
Surface plasmon resonance	SPR
Tetrahydrofuran	THF
Thymine	T
Transmission electron microscopy	TEM
Ultraviolet	UV
X-ray diffraction	XRD

Chapter 1 Introduction

Fluorescence resonance energy transfer (FRET) is a widely used technique with the advantage of simplicity and direct response in biosensing fields. It provides distance information between two molecules in angstrom range, which is not easily accessible. However, the photobleaching effect, low stability and short fluorescence life time of traditional organic florescence donor molecules hinders the applications of typical FRET in biosensing fields. The quenching efficiency of acceptor molecules in FRET assay is also needed to improve. Therefore, in order to achieve more efficient and reliable FRET biosensors, novel nanomaterials have been used in FRET assays as both donors and acceptors with advantages of long fluorescence life time, high stability and high quantum yield and high energy transfer efficiency. In this dissertation, graphene based nanomaterial including graphene quantum dots (GQDs) and graphene oxide (GO) are investigated as donors and acceptors in FRET assay, respectively. GQDs are regarded as novel fluorescent donor with strong and stable photoluminescence (PL). GO is considered to be an excellent platform for biosensing because of its high surface to volume ratio with super quenching ability. Moreover, the greatest advantages of both GQDs and GO are their low toxicity as well as easy functionalization with different biomolecules, which enhance their applications in FRET biosensor for various biomolecules detection.

The introduction of FRET mechanism and FRET biosensors are presented in Section 1.1. Then, the structure, synthesis and properties of graphene quantum dots (GQDs) are introduced in Section 1.2. This is followed by introduction of graphene

oxide (GO) in Section 1.3. The application of GQDs and GO in FRET biosensors are then described in Section 1.4. Finally, the objectives of this study are stated in Section 1.5.

1.1 Fluorescence Resonance Energy Transfer (FRET) Biosensor

1.1.1 Fluorescence Resonance Energy Transfer (FRET)

Fluorescence resonance energy transfer (FRET) is a distance-dependent phenomenon with the energy transfer from a donor fluorophore to an acceptor fluorophore [1]. When FRET occurs, it always involves the change of fluorescence signal, such as intensity change and emission peak shift. There are two types of acceptor molecules including fluorophore and non-fluorescent molecule. When a fluorophore molecule acts as the acceptor, the transferred energy can be emitted as fluorescent light with the emission peak shift. Otherwise, the transferred energy is lost when the acceptor molecule is not a fluorophore. Such phenomenon without emitted fluorescent light is also called fluorescence quenching effect.

Fig. 1.1.1 shows the sketch of traditional FRET phenomenon. The donor fluorophore is excited by incident light, while an acceptor is in close proximity. Thus, the excited state energy can be transferred from the donor to the acceptor through non-radiative dipole-dipole coupling [2]. It is worth noticing that this fluorescence energy transfer occurs only when the distance between donor and acceptor is highly strict within 8 nm. Therefore, in some ways, the ability of providing accurate small distance

information (10–80 Å) makestypical FRET to be a valuable tool for nano-scaled biological research [3].

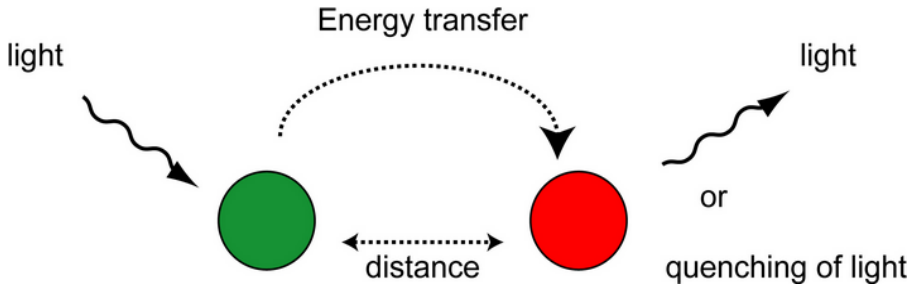

Fig. 1.1.1 Sketch of a typical FRET phenomenon (Adapted from [2]).

The efficiency of this energy transfer is susceptible to the distance between two interacted molecules. The equation of FRET efficiency is illustrated as following [4]:

$$E=\frac{1}{1+(\frac{r}{R})^6} \quad (1)$$

Where r is the distance between donor and acceptor, and R is the fluorescent distance of donor and acceptor, i.e. the distance at which the energy transfer efficiency is 50%. From equation (1), it can be seen that the energy transfer efficiency is in inverse proportion to the sixth power of the distance between donor and acceptor, which demonstrates that traditional FRET is a highly distance-dependent phenomenon. As shown in Fig.1.1.2, FRET efficiency decreases dramatically with the increasing distance of r [7]. Moreover, one essential requirement of FRET is that the emission spectrum of the donor must overlap with the absorption spectrum of the acceptor (Fig.1.1.2) [5, 6, 7]. Only when these necessary conditions are met, FRET can happen. Fig.1.1.3 displays some common organic fluorescent dyes and fluorescence proteins as FRET donor/acceptor pairs [8, 9]. Besides, quantum dots (QDs) [10, 11] are also served as

FRET donor. In summary, FRET effect is a highly distance-dependent phenomenon with matching donor/acceptor pairs.

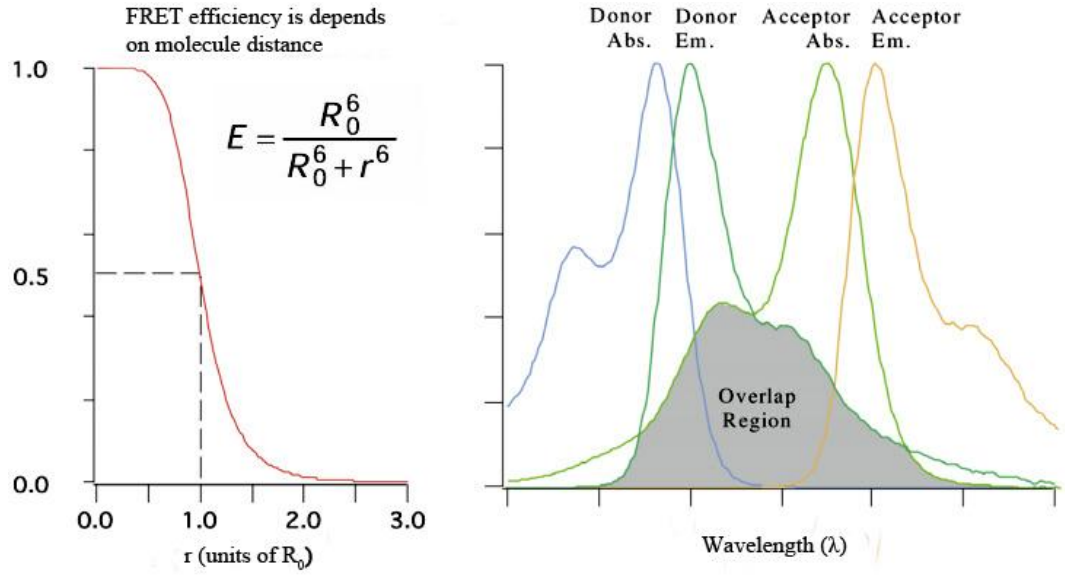

Fig. 1.1.2 FRET efficiency with the increasing distance between donor and acceptor (left); Absorbance and emission spectra of both donor and acceptor, respectively (right) (Adapted from [7]).

Donor	Acceptor
7-Methoxycoumarin	DABCYL
Amino Methyl Coumarin	DABCYL, QSY-35
Blue Fluorescent Protein	Ds Red Fluorescent Protein
BODIPY-FL	DABCYL, QSY-7, QSY-9, BHQ-1
B-Phycoerythrin	Cy5
Cy3	Cy5, QSY-7, QSY-9, BHQ-2
Cy5	Cy5.5, QSY-35, BHQ-2
Dansyl	FITC
EDANS	DABCYL
FITC	Eosin Thiosemicarbazide
Fluorescein	Tetramethylrhodamine
Green fluorescent Protein	Yellow Fluorescent Protein
Pacific Blue	DABCYL, QSY-35
Tryptophan	Dansyl

Fig. 1.1.3 Examples for common FRET donor / acceptor pairs (Adapted from [8]).

1.1.2 FRET based biosensor

Biosensor is an analytical device that usually consists of three parts, including biorecognition component, biotransducer component, and electronic system [12]. As shown in Fig. 1.1.4, biosensors can be classified by both bioreceptors and transducers [13]. The bio-recognition components include antibodies, enzymes, cells, nucleic acids, biomimetic and phage, and they can specifically recognize various disease markers. Biosensor has widely been used for detection of biomolecules associated with varied diseases in human body, such as foodborne disease [13-15], neurotoxin disease [16-18], and cancer [19]. On the other hand, the transduction methods are classified as optical approach [15, 20-21], mass-based approach [22-23] or electrochemical approach [24-25]. Among numerous types of biosensors, this thesis is mainly focused on optical biosensor centered at FRET approach.

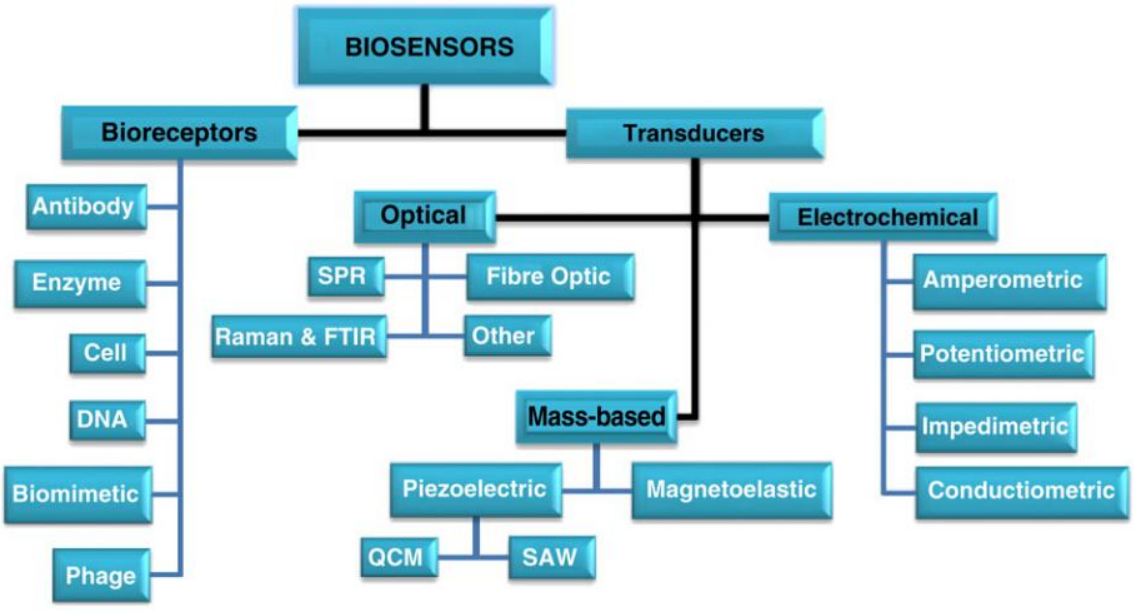

Fig. 1.1.4 Classification of biosensor (Adapted from [13]).

Principle of FRET biosensor is tied to the change of distance-dependent fluorescence signal, which is used to monitor quantitative and dynamic molecular interactions *in vitro* [10, 26-27] or *in vivo* [28-29].For instance, nucleic acid FRET biosensor can be easily established between fluorescent dye labeled oligonucleotides and corresponding fluorescent acceptor labeled complementary oligonucleotides for DNA hybridization detection via monitoring the change of fluorescence signal [1, 26]. Dong et al. designed an effective sensing platform via FRET effect between QDs (donor) and GO (acceptor) for target DNA detection [10]. As shown in Fig. 1.1.5, before hybridization with target DNA, the fluorescence of QD is quenched by GO due to the close distance. However, the energy transfer between QD and GO was aborted after DNA hybridization, which enlarges the distance between the donor/acceptor pair. Based on the change of fluorescence intensity, the limit of detection for target DNA was measured to be 12 nM. Noticeably, Dong et al. also applied this FRET biosensor for protein detection through specific aptamer-protein binding interaction, which demonstrated the promising feasibility of the FRET biosensing in different fields [10]. Eunkeu et al. investigated the FRET efficiency between QDs and AuNPs, and demonstrated this sensing system could be used as bimolecular inhibition assay. The limit of detection (LOD) of avid in was around 10 nm (Fig. 1.1.6) [26]. Thus FRET biosensor is able to offer a simple and rapid sensing platform for various biological molecules detection with high efficiency and sensitivity.

However, despite all the observable advantages, the limitations of typical FRET biosensing cannot be ignored. High specificity and dependence of the overlapping spectrum between donor and acceptor make FRET to be “one to one” phenomenon,

which hampers the wide applications of FRET. Furthermore, conventional FRET pairs' modification process remains to be a continuous challenge. It is always quite challenging to achieve 100% quenching efficiency since not all the donor-acceptor pairs can be brought into close proximity. When the distance between a pair of fluorophores doesn't meet the requirement (within 80 Å), FRET effect cannot be observed. So the efficiency of FRET is largely dependent on short-range distance. In this case, we need to find some way to obtain a flexible long-range FRET biosensor with high efficiency.

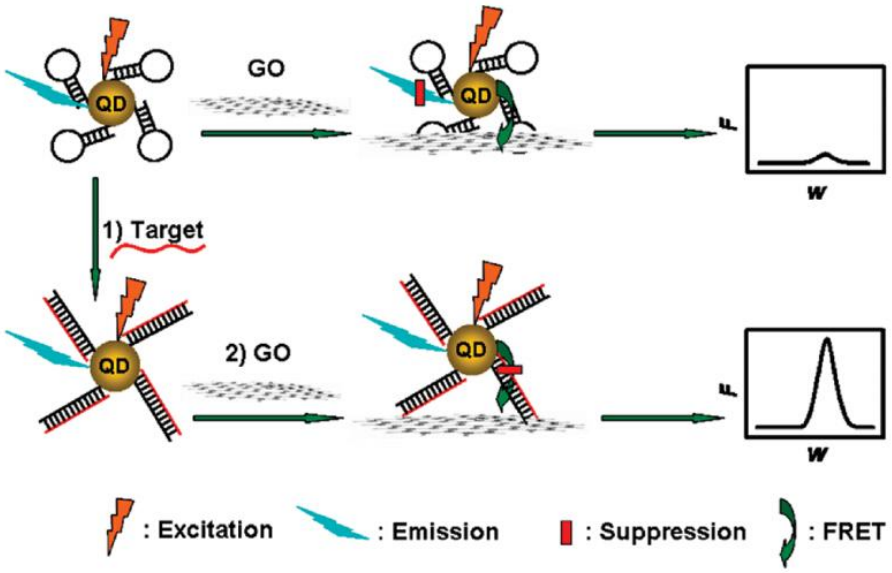

Fig. 1.1.5 Schematic illustration of the fluorescence quenching mechanism between GO and MB-QDs (Adapted from [10]).

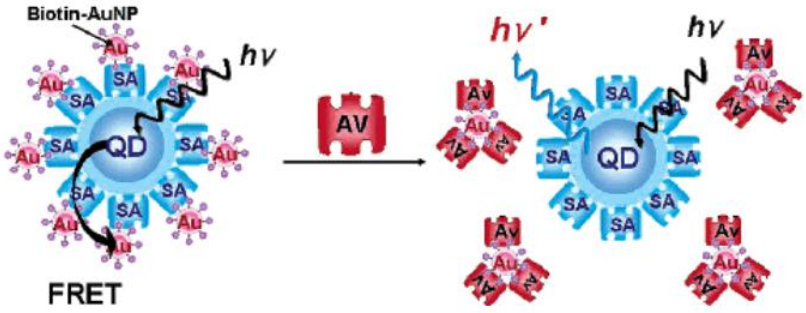

Fig. 1.1.6 Schematic representation of fluorescence quenching effect of SA-QDs by biotin-AuNPs for inhibition assay (Adapted from [26]).

1.2 Graphene quantum dots (GQDs)

1.2.1 Graphene quantum dots and its structure

Since the discovery of graphene by Geim and Novoselov et al. in 2004, researches associated with graphene bloom due to its unique thermal, mechanical and electronic properties. As graphene sheet is zero band-gap semiconductors with the infinite exciton Bohr diameter, luminescence is nearly impossible to be observed. By converting 2D graphene sheet to 0D small pieces of graphene fragments, the 0D graphene fragments obtain luminescence properties due to the quantum confinements and edge effects. These 0D small pieces of graphene fragments are called graphene quantum dots (GQDs), which have emerged as extremely promising fluorescent nanoparticles with considerable research interests in tremendous fields.

Typically, the diameter of GQDs is under 20 nm. As shown in Fig. 1.2.1, the TEM and AFM images indicate that solvothermal treatment and separation method fabricated GQDs are equipped with lattices of 3.1 nm diameter and 1 nm height [30]. As a result, the nano-scaled GQDs, confining excitons in all three spacial dimensions, would be small enough to trigger pronounced quantum confinement effect and edge effect. These two pronounced effects will feature GQDs with non-zero and tunable bandgap, and introduce unique physical, electronic and optical properties to GQDs. Nevertheless, the most characteristic advantages of carbon based quantum dots are their non-toxicity and excellent biocompatibility, which promote the application of GQDs in medicine and biology. Thus, it is widely believed that GQDs with extraordinary properties will gradually replace traditional semiconductor quantum dots (QDs).

Because the synthetic procedures of conventional QDs, such as CdSe and CdSe-Zns, always involve toxic components, it hampers their developments in biological field [31-34]. Furthermore, another benefit of GQDs is that carbon based materials are theoretically abundantly available, and they are easy to be obtained and prepared with high solubility in various solvents. So it is feasible to employ GQDs in many kinds of biomedical applications.

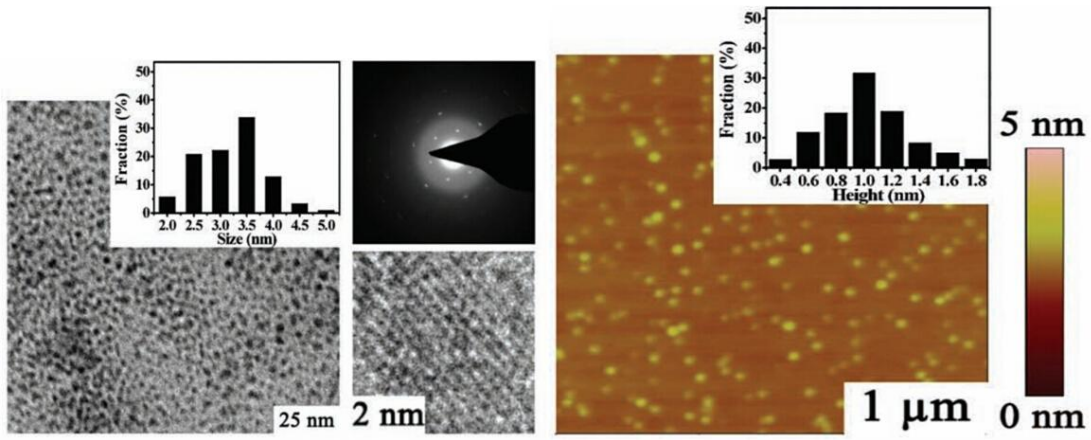

Fig. 1.2.1 TEM image (left) and AFM image (right) of GQDs (adapted from [30]).

1.2.2 Properties of graphene quantum dots

1.2.2.1 Absorption

For the UV-vis absorption of GQDs, strong absorption mostly centers in UV region and extends a long absorption edge up to the visible range (Fig.1.2.2) [35]. The characteristic peak of GQDs appeared around 230 nm is attributed to π-π* absorption of aromatic C=C bond. However, according to Pan et al., another absorption band of GQDs is also observed at 320 nm, which is assigned to n-π* transition of C=O [36]. This small difference mainly depends on the ratio of carbon to oxygen in GQDs, which is

determined by various synthesis methods. The lower ratio of oxygen content exists in GQDs, the weaker absorption peak can be observed around 320 nm. For example, if GQDs are prepared by exfoliation method, the oxygen groups will break up completely, then the π-π* transition of aromatic C=C bond will red shift to 270 nm with the disappearance of n-π* transition of C=O bond [37].

1.2.2.2 Photoluminescence

For the photoluminescence, GQDs possess excitation wavelength dependent PL emission behavior, which is consistent with most luminescent carbon nanoparticles [36]. As shown in Fig 1.2.2, the PL of GQD displays red-shifted peak accompanied with decreasing intensity, when the excitation wavelength increases from 300 to 470 nm [35]. Especially, the brightest and strongest blue luminescence of GQDs can be observed under UV excitation at 360 nm (Fig.1.2.2 inset).

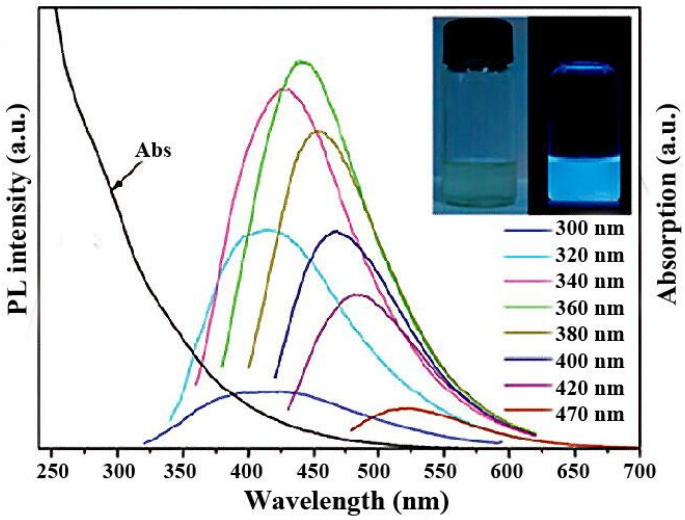

Fig. 1.2.2 Absorption spectrum of GQDs and PL spectra of GQDs under different excitation wavelengths range from 300 to 370 nm. Inset: image of GQD solution under visible light (left) and 360 nm UV light (right) (Adapted from [35]).

This strong blue luminescence is caused by the considerably large bandgap between lowest unoccupied molecular orbital (LUMO) and highest occupied molecular orbital (HOMO). As shown in Fig.1.2.3, the energy gap generally depends on the size of sp^2 clusters. The fewer number of aromatic rings exists in GQDs, the smaller sp^2 fragments are presented, and this could lead to larger energy gap followed by stronger PL of GQDs [38]. On the other hand, it suggests that the bandgap of nano-scaled GQD is tunable from 0 eV to that of benzene by the modification of nanocrystals' size, shape and surface chemistry [38]. Thus, the PL emission of GQDs can also be tailored by size and surface modification, including controlled reduction and oxidation [39].

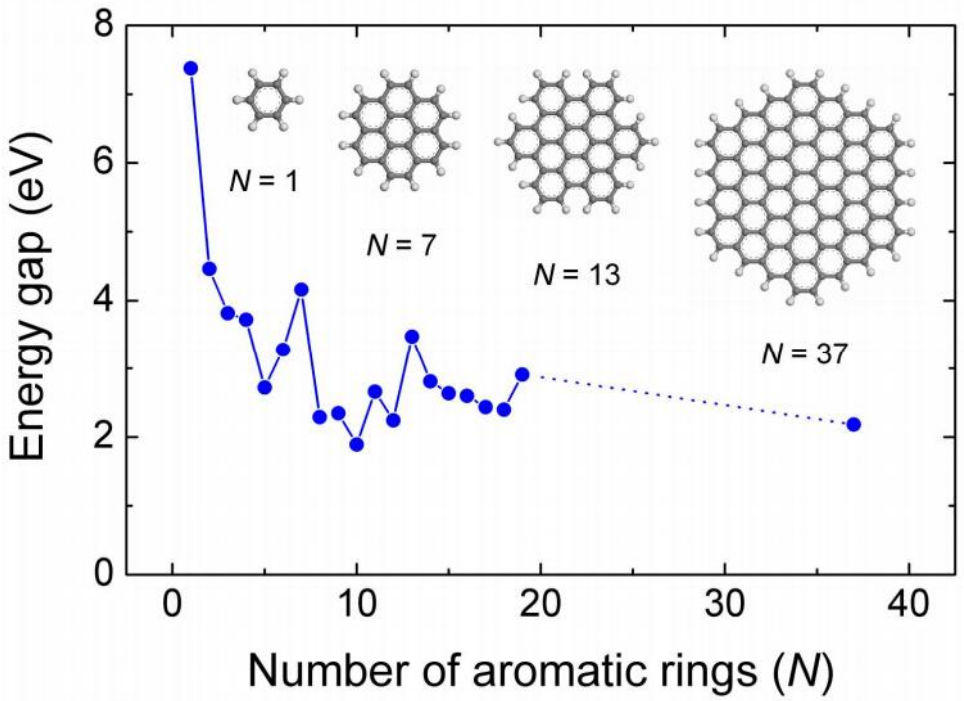

Fig. 1.2.3 Calculated energy gap of π-π* transitions with increasing number of aromatic rings (N) by density functional theory (DFT). Inset: structures of graphene used for calculation (Adapted from [38]).

The size-dependent PL property of GQDs is largely due to quantum confinement effect, which is a primary feature of quantum dots. With the decreasing size of GQDs, the bandgap increases and short wavelength of high energy emission can be observed. It is impossible for micrometer-sized graphene sheet or graphene nanoribbon to observe luminescence because of their large lateral size [39]. Generally, when the size of GQDs is smaller than 20 nm, it is small enough to trigger strong quantum confinement effect and edge effect leading to the photoluminescence [40].

Functional groups on GQDs surface can induce further properties and influence the PL, and this phenomenon is also called edge effect. GQDs with barren oxygen groups can emit blue fluorescence. In contrast, if GQDs has rich oxygen groups on the surface, it can emit green luminescence. The color distinction of luminescence is resulted from varied fabrication methods of GQDs. For instance, Pan et al. used a hydrothermal route to cut micrometer-sized graphene sheets into GQDs fragments with strong blue luminescent [40]. This blue luminescence was attributed to the intrinsic state emission of GQDs because of the complete breakup of oxygen groups during the cutting process. However, according to Zhu et al. [41] and Li et al. [42], solvothermally and electrochemically synthesized GQDs can emit green fluorescence under excitation of 365~375 nm because of the abundant hydroxyl, carbonyl and carboxylic acid groups appeared on GQDs surfaces. Strictly speaking, GQDs with rich oxygen groups were considered to be graphene oxide quantum dots (GOQD) [43]. The existence of oxygen groups can disturb fraction of sp^2 bonded carbon atoms by introducing the sp^3 matrix, which contributes to the surface defect of GQDs. The higher degree of oxidation or modification would lead to much more surface defect, and result in defect state emission

with red-shifted wavelength. Thus, tunable bandgap can also be achieved by controlling the sp^2 domain to manipulate the competition between intrinsic state emission and defect state emission, which could affect the PL emission of GQDs. Zhu et al. tailored the fluorescence color of GQDs from green to blue by controlling the bandgap between LUMO and HOMO via reduction of oxygen groups and surface modification by methylamine coupling (Fig. 1.2.4) [30]. Since both the reduction of oxygen group and surface modification could enhance the sp^2 domain, the r-GQD and m-GQD can both emit blue luminescence by tuning defect state emission into intrinsic state emission. According to Tetsuka et al. [44], amine functionalized GQDs can emit green light with high quantum yield around 29~19%. Zhang et al. [45] obtained water-soluble GQDs with yellow luminescence by electrochemically exfoliating graphite followed by reduction with hydrazine at room temperature. The excessive functioned hydrazide groups on GQDs were served as the leading role of surface defect emission, resulting in bright yellow fluorescence.

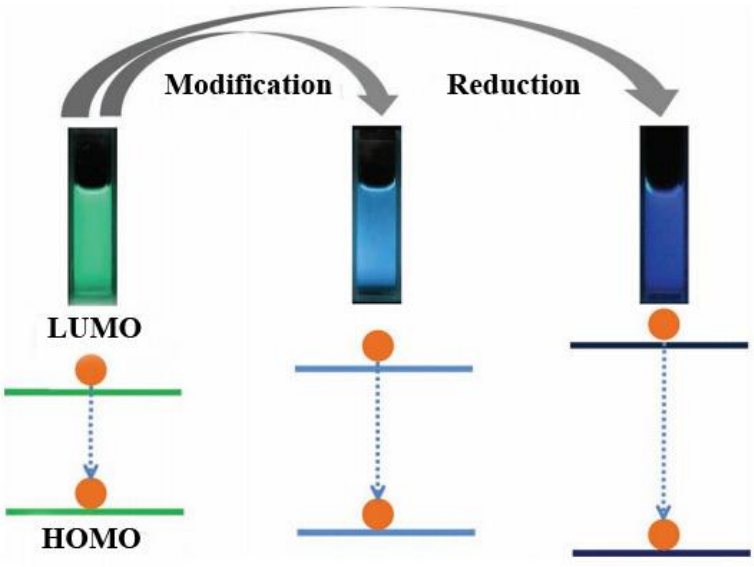

Fig. 1.2.4 Scheme of PL emission control by bandgap tailoring of GQDs, m-GQDs and r-GQDs (Adapted from [30]).

The photoluminescence of GQDs is a complicated phenomenon. Apart from the size of nanocrystal and the functional groups on GQDs surface, the PL of GQDs is also dependent on pH environment. Pan et al. [40] claimed that PL intensity of hydrothermal synthesized GQDs decreased dramatically or even be quenched with the decreasing pH value in acidic solution. But in alkaline solution, PL intensity of GQDs was significantly enhanced (Fig. 1.2.5). And the PL intensity was reversible in changing pH environment. Similar results were obtained by other groups [46, 47]. Generally, it is believed that the pH dependence in GQDs is originated from the free zigzag sites in GQDs. As shown in Fig. 1.2.6, free zigzag sites of the GQDs can interact with H^+ under acidic condition, which breaks the emissive triple carbene and hampers the emissive state in PL. Under alkaline condition, the fluorescence is recovered by the release of free zigzag sites.

However, according to the work by Zhu et al. for the pH dependent emission of GQDs, the PL intensity of solvothermally prepared GQD decreased and was accompanied with red shift or blue shift of emission peak regardless of acidic or alkaline environments [41]. Only in neutral condition, the PL intensity remained stable [41, 48] (Fig. 1.2.7). This phenomenon cannot be explained by the zigzag effect obviously. Latterly, Zhu et al. discovered that surface modified GQDs were much more stable in changing environment comparing to bare GQDs (Fig. 1.2.8) [30]. Alkylamines modified GQDs can keep the blue emission in both acidic or alkali solution, and reduced GQDs can maintain the PL emission peak with pH valve ranging from 0 to 14. They explained these phenomena by the defect surface in GQDs caused by functional groups, which were easy to trap ions. According to Shen et al. [49], in neutral solution, surface passivated GQDs (such as PEG grafted GQDs) showed enhanced PL with quantum yield

of ~28%, which was almost three times higher than that of bare GQDs. The enhanced PL was attributed to higher quantum confinement effect which was induced by the trapped energy in GQDs surface through surface passivation [50].

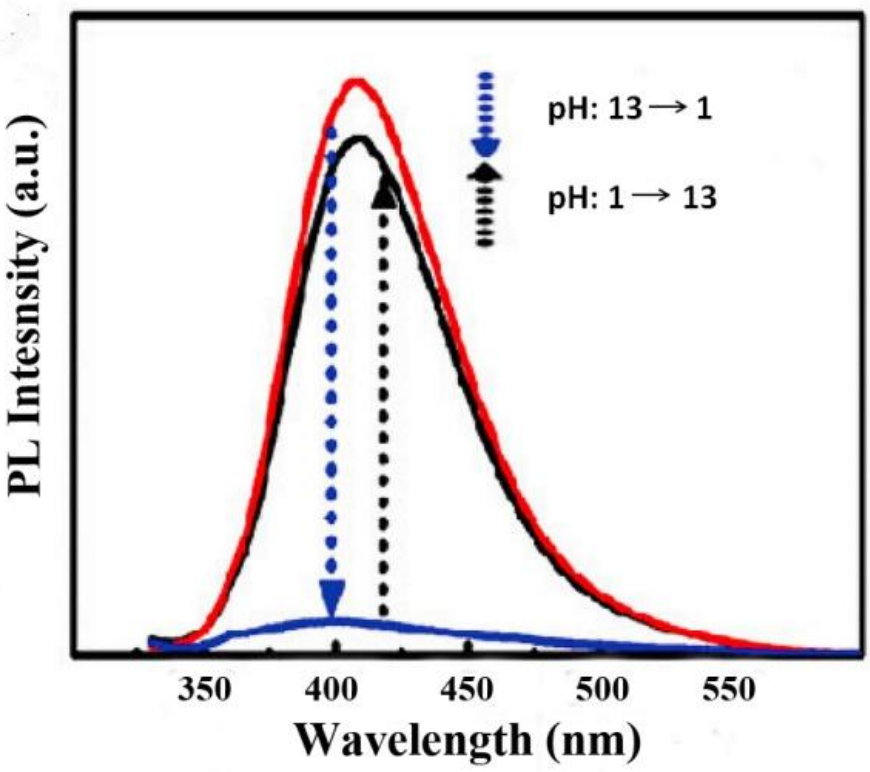

Fig. 1.2.5 PL intensity of GQDs with switched pH value between 13 and 1 (Adapted from [40]).

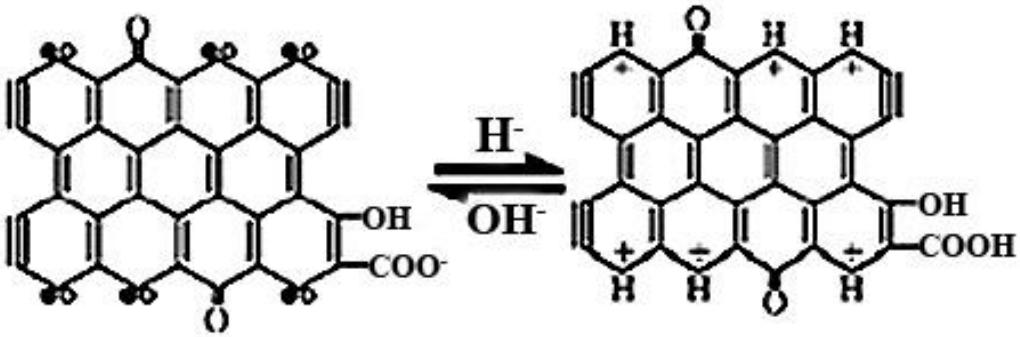

Fig. 1.2.6 Reversible models of the GQDs in acidic (right) and alkali (left) solution (Adapted from [46]).

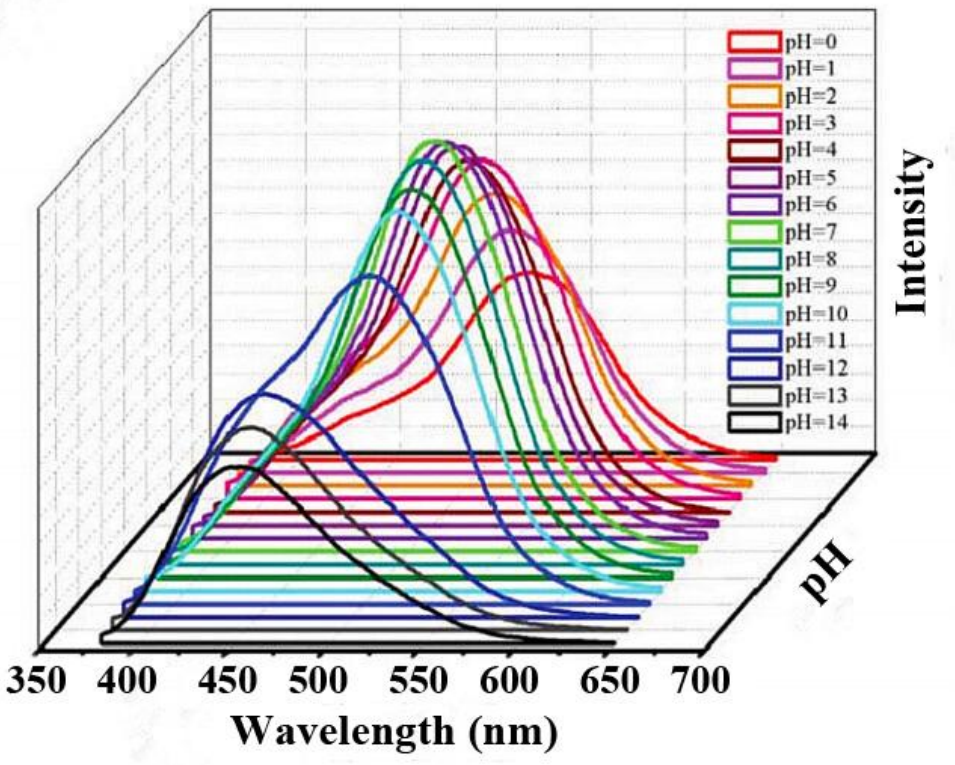

Fig. 1.2.7 The pH-dependent PL behavior of GQDs (Adapted from [41]).

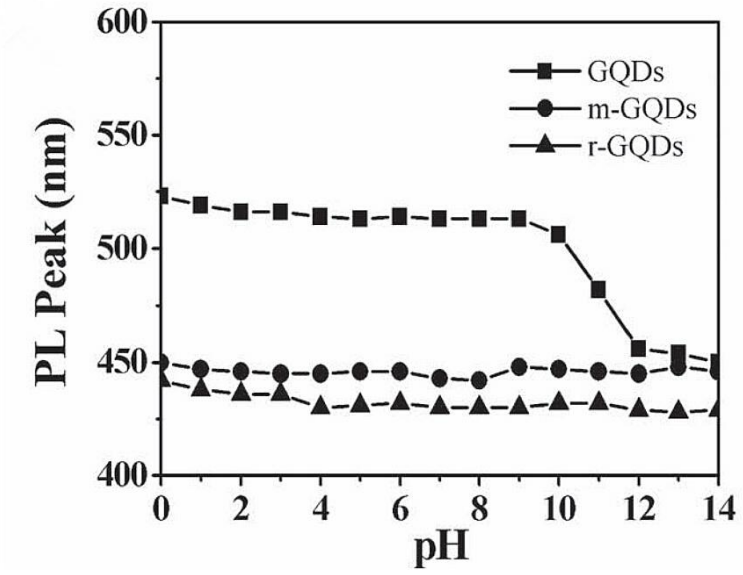

Fig. 1.2.8 PL peak of GQDs, m-GQDs, and r-GQDs with increasing pH value (Adapted from [30]).

Beside the factors described above, photoluminescence of GQDs is also influenced by various solvents. As shown in Fig. 1.2.9, the PL wavelength peak of GQDs shows gradually blue shift from 515 nm to 475 nm in various solutions, including water, DMF, acetone, and tetrahydrofuran (THF), successively. Whereas, the solvent-dependent behavior is negligible in surface modified GQDs (m-GQDs) and reduced GQDs (r-GQDs) [30]. This solvent-dependent effect is largely attributed to the highly soluble properties of GQDs in both water and polar organic solvents. Nevertheless, the reason for the highly soluble properties of GQDs is the existence of surface oxygen groups, which could switch the electron state in defect region.

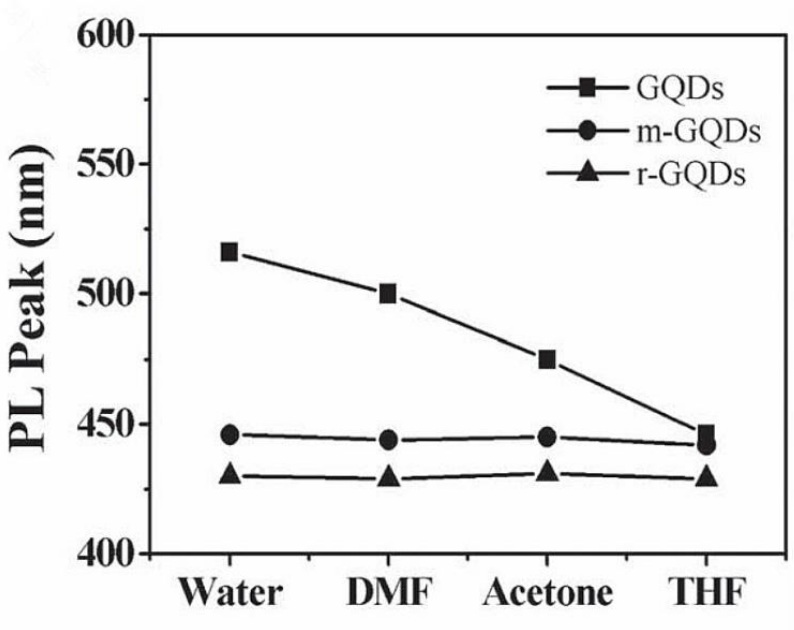

Fig. 1.2.9 Solvent dependent PL of GQDs, m-GQDs, and r-GQDs (Adapted from [30]).

Therefore, those different PL mechanisms clearly indicate that GQDs are of complicated PL properties, relating to varied fabrication and modification methods. Since the discovery of GQDs is still in the initial phase, dependent effect of PL is still a problem that remains to be eliminated in order to obtain various applications for GQDs.

1.2.2.3 Upconversion luminescence

The first upconversion luminescence GQDs was reported by Shen et al. [35]. They synthesized surface passivated GQDs with PEG through hydrazine hydrate reduction of GO. When exciting these PEG-GQDs with excitation wavelength ranging from 600 to 800 nm, the wavelength peak of upconverted emission showed red-shift from 390 to 468 nm, respectively. Similar results were also reported by Zhu et al. and Zhuo et al. [30, 51]. The reason for the upconversion luminescence can be attributed to not only multi photon active process, but also anti-stokes photoluminescence (ASPL) [35]. Briefly, normal PL occurs when electrons transit from the LUMO to the HOMO (Fig.1.2.10 a, b). However, when the electrons get excited at π orbital, they can jump to LUMO, and then drop back to the low energy state (σ orbital) (Fig.1.2.10 c, d). This PL caused by electrons transition from π orbital to σ orbital is considered to be upconversion luminescence. Although it is not the major focus in this article, it is still worth mentioning that upconversion luminescence property of GQDs is an interesting phenomenon. It opens a door for near-IR light diagnostics using multi-photon excitation, which is less harmful to living bio-systems.

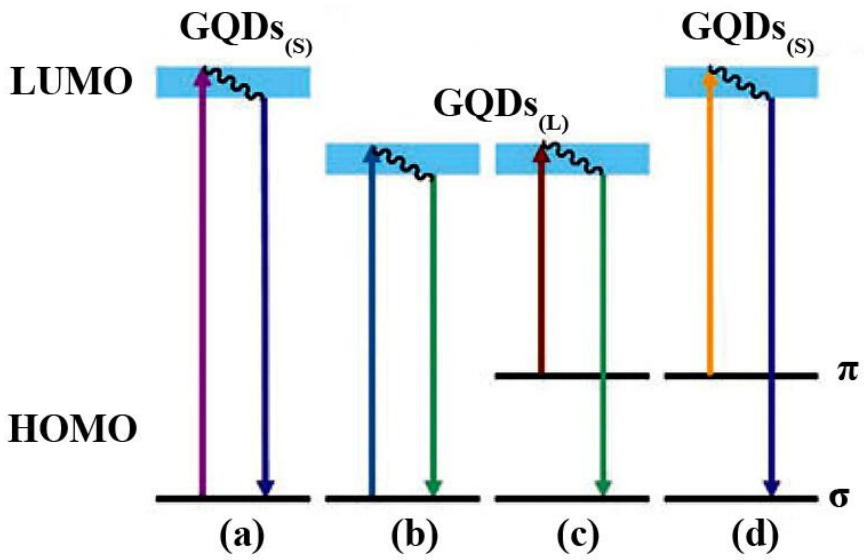

Fig. 1.2.10 Mechanism of different electronic transitions processes in GQDs. Normal PL (a, b) and upconverted PL (c, d) mechanisms in both small and large sized GQDs, respectively (Adapted from [35]).

1.2.2.4 Cytotoxicity

GQDs possess high brightness, longer fluorescence lifetime and better photo-stability, In addition, the toxicity of GQDs is considerably low, making GQDs more environmental friendly and biocompatible in many fields, such as bioimaging [30, 41, 47, 48], biolabeling [45, 52], biosensing [52] and drug/gene delivery [48, 53]. The low toxicity was demonstrated by Zhu. et al. through cell viability test on human osteosarcoma cells using methylthiazolyldiphenyl-tetrazolium bromide (MTT) assay. MC3T3 cells showed more than 80% relative cell viability with 400 μg additional GQDs [30]. Consistent results were obtained by Hu et al. [47]. The low cytotoxicity of GQDs indicates the huge potential for biomedical applications.

1.3 Graphene oxide (GO)

1.3.1 Graphene oxide and its structure

Graphene is the first 2D material that is made up of a single layer of carbon atoms bonded in sp^2 hybridization [54]. Although scientists tried to obtain graphene through different complex methods since 1859 [55, 56], graphene remained as a mysterious material existed only in theory and was firstly fabricated in 2004 [57]. Crystal graphene was discovered by Andre Geim and Konstantin Nlovoselov using a very simple and effective method, which involved the repeating adhesion by scotch tape. The two scientists were awarded the Physics Nobel price at 2010. After that, graphene has been noticed in multi-disciplinary and it is considered to be the greatest material that may change the world in decades.

Graphene oxide (GO) is the derivative of graphene, but it has longer and independent history comparing to graphene. The history of GO can be traced back to the studies associated with graphite oxidation almost 150 years ago. The first GO was synthesized from graphite by Brodie via $KClO_3$-fuming HNO_3method at 1860 [58]. At that time, GO was termed to be "graphon". Later, Staudenmaier improved Brodie's study by multi-addition approach [59]. However, both Brodie and Staudenmaier method involved ClO_2 gas, which was of high toxicity to human and environment. At 1958, Hummers and Offeman developed another oxidation method to prepare graphene oxide, involving the reaction of graphite with a mixture of potassium permanganate ($KMnO_4$) and concentrated sulfuric acid (H_2SO_4) [60]. Among these three principal oxidative treatments, Hummer's method has been widely used till today due to its low toxicity.

The formation of Hummer's method is shown as following [60]:

$$KMnO_4 + 3\,H_2SO_4 \longrightarrow K^+ + MnO_3^+ + H_3O^+ + 3\,HSO_4^-$$

$$MnO_3^+ + MnO_4^- \longrightarrow \mathbf{Mn_2O_7}$$

From the long history of GO, it can be seen that GO has regarded as a precursor of graphene related material. As shown in Figure 1.3.1, GO is a similar 2D single layer to graphene, but equipped with carboxyl groups on the edges, hydroxyls and epoxies groups on the basal plane [61]. The ratio of carbon to oxygen is determined by various preparation methods [62].

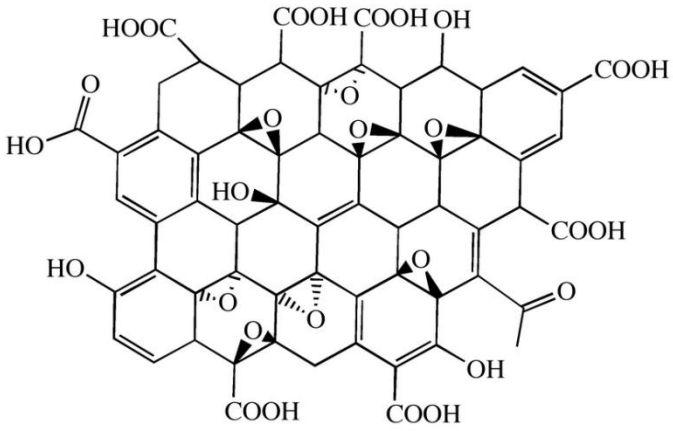

Fig. 1.3.1 Sketch of chemical structure of graphene oxide (Adapted from [61]).

The existences of oxygen groups bring disordered electron structures to GO. In details, graphene sheet are constructed by ordered sp^2 hybridized carbon atom arranged in honeycomb-shaped lattice. After oxidation of graphite to graphene oxide, the induced oxygen groups can break previous sp^2 bonded structure in graphene sheets via the disturbance of sp^3 C-O matrix [61]. Thus GO is a network that contains both sp^2 and sp^3 concentrations. From atomic study, the thicknesses of monolayer GO was around 1 nm, which was larger than that of graphene sheet (around 0.6 nm) [63, 64]. Consistent results

were also be obtained by Huang et al. [65].They examined GO sheet with thickness around 1 nm by typing-mode AFM (Fig.1.3.2 (a), (b)), and the paper-like structure of GO was also indicated by TEM and SEM image (Fig.1.3.2 (c), (d)). It is widely considered that the induced functional groups located slightly above or below graphene flat are mainly attributed to the atomic roughness in GO.

Nevertheless, despite the disturbance caused by functional groups on basal plane, GO still preserves the structure of graphene lattice, standing with strain and disorder. Numerous works readily observed the co-existence of π state from sp^2 carbon clusters and σ state from sp^3 bonded matrix in GO. Wilson et al. compared the Raman spectroscopy between monolayer GO and monolayer graphene, as shown in Fig. 1.3.3, the emerged intense D band (1350 cm^{-1}) and broadened G band (1600 cm^{-1}) identify the disorder-induced sp^3 C-O bond that co-exists with sp^2 clusters in GO [66]. Mattevi et al. demonstrated the size of sp^2 clusters in GO and reduced GO by Raman spectroscopy [67]. And they found that the oxidation degree determined the ratio of sp^2 carbon-bonds and sp^3 C-O bond in GO. Paredes et al. [64] used atomic force and scanning tunneling microscopy (AFM/STM) to investigate oxygen distortion in GO comparing to reduced graphene oxide (rGO). The results indicated that the height of rGO was lower than GO due to the absence of functional groups. Wilson et al. testified the honeycomb lattice along with disorder in GO by high resolution transmission electron microscopy (HR-TEM) and the sharp selected-area electron diffraction (SAED) [66]. The highly defective regions appeared to be intact with the presence of oxygen groups.

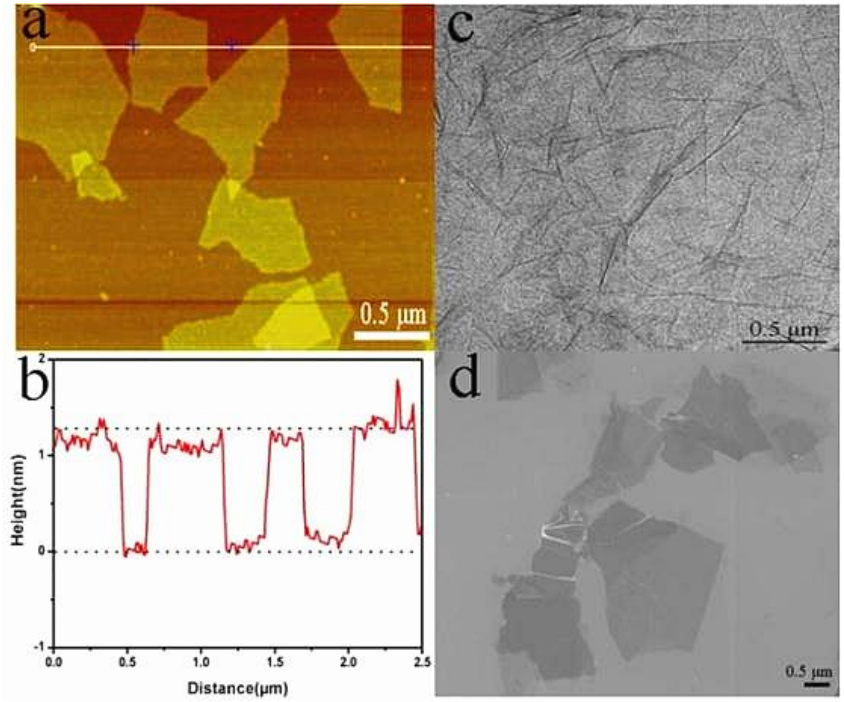

Fig. 1.3.2 Typical AFM image and height profile of GO sheet (a, b); TEM (c) and SEM (d) image of GO (Adapted from [65]).

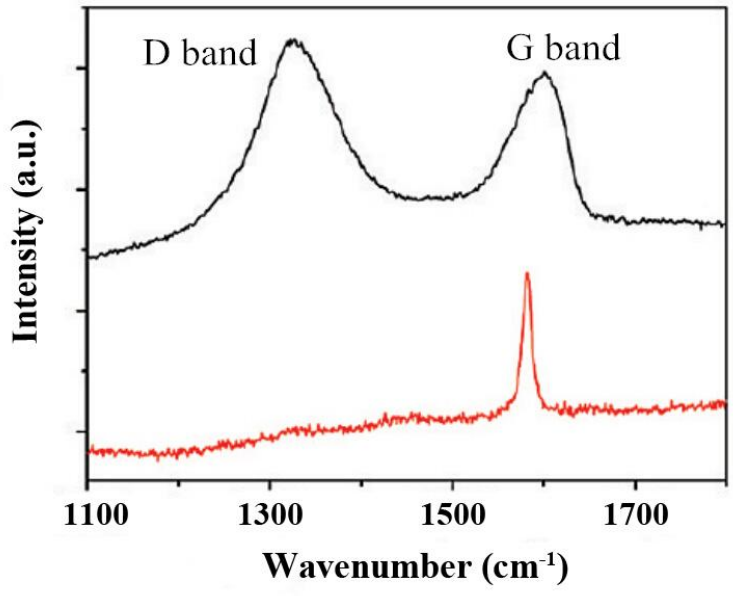

Fig. 1.3.3 Raman spectra of GO (black line) and graphene (red line) (Adapted from [66]).

Since optical and electrical properties of carbon based material are mainly determined by π electrons from sp^2 carbon, the fraction of sp^2 clusters is a crutial parameter to control the optoelectronic properties of GO. Thus in order to achieve tailorable optoelectronic properties of GO, various oxidation methods can be used to tune the fraction of sp^2 clusters by carefully controlling the presence of oxygen functional groups on GO surface [68]. As a consequence, the hybridization of sp^2 and sp^3 carbon bonded site even enables the tunable transfer of GO from an insulator to a semi-conductor and even to a graphene-like semi-metal [69]. On the other hand, this disturbance of sp^3 carbon matrix is regarded as surface defect in GO, which makes it possible to cleave GO into small size (nano-scaled GO). Noticablely, small graphene fragments are equipped with entirely different properties compared to micro-scaled GO. According to Shen et al., if the size of GO is smaller than 20 nm, the nanoscaled GO is considered to be graphene quantum dots (GQDs), which possess unique optical properties [35]. Structures and properties of GQDs are described in Section 1.2.

1.3.2Properties of graphene oxide

GO is often regarded as a disordered material due to the presence of functional groups, providing itself with numerous excellent properties as a novel biomaterial.

1.3.2.1 Hydrophilic

The existence of oxygen groups at edge or basil plane improves the hydrophilic capability of GO, thus GO can be well dispersed in water and certain organic solvents by simply sonication. Cai et al. initially reported the stable GO suspension in highly polar organic solvents, such as N, N-dimethylformamide (DMF) and dimethyl sulfoxide

(DMSO), without surface modification [70]. Paredes et al. comprehensively investigated the dispensability of GO in various organic solvents [71]. As shown in Fig. 1.3.4, GO was dispersed in water and 13 kinds of organic solvents, respectively. By comparing the dispersions before and after 3 weeks, it readily to conclude only water, ethylene glycol, DMF, NMP and THF can exhibit long-term stability with GO. Excellent dispersion in water gives opportunities to GO to be more water friendly, and has great potential to be used as biocompatible functional nanomaterials. Stable dispersion behavior in organic solvents facilitates the development of hybridized materials based on graphene oxide.

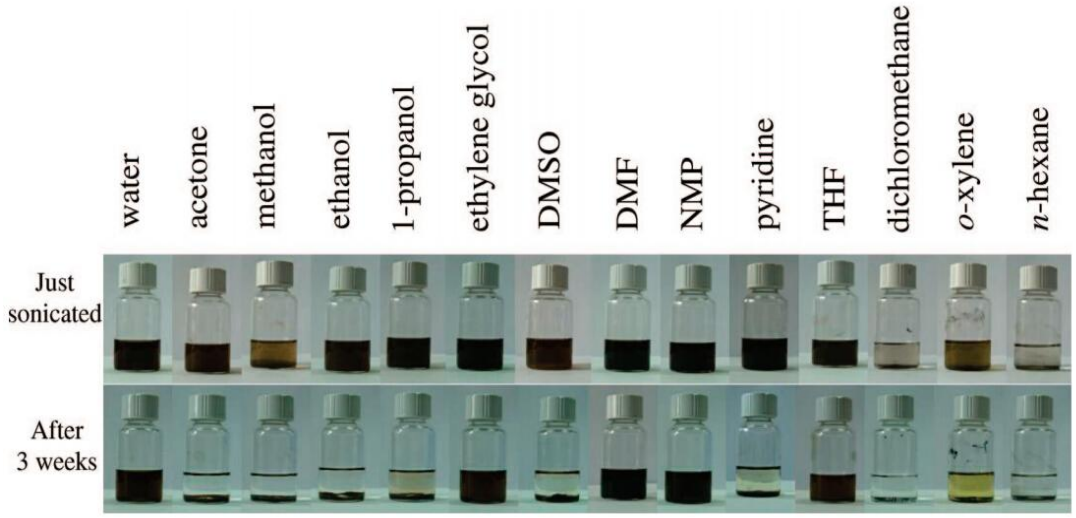

Fig. 1.3.4 Pictures of GO dispersed in various solvents after1 h bath ultrasonication. Top: dispersions images after just sonication. Bottom: dispersions images after 3 weeks standing (Adapted from [70]).

1.3.2.2 High surface-to-volume ratio.

The single atomic layer of graphene means that "bulk" theoretically does not exist when all carbon atoms are exposing to the environment [72]. In the same manner, paper-liked graphene could serve as flat substrate interacting with diversity

biomolecules simultaneously. According to AFM image and height profiles, the thickness of GO is around 1 nm, while the width of GO can range from micro to nano scale. These properties emphasize the flat sheet structure of GO with giant surface areas, which provides numerous interaction sites with abundant biomolecules at the same time [64, 65]. Besides, most of the biosensing approaches generate response according to the interaction between substrate and analyte, which interacts only with the surface of substrate. Nanomaterials with surface-area-to-volume ratio sensibly higher than their bulk counterpart can be expected to increase sensitivity and response time significantly. Examples are FET biosensing, fluorescence resonance energy transfer (FRET) biosensing and cellular activity sensing platform. Thus the property of high surface to volume ratio poses a great advantage with GO as a biosensing platform.

1.3.2.3 Multiple physical and chemical mobilizations.

The functional oxygen groups also give GO more opportunities to chemical and physical immobilization (Fig. 1.3.5) [73]. For chemical functionalization, carboxylic acid groups (-COOH) enable the covalent bonding with nucleophilic species, which offer multiple surface modifications. In specific, the carboxylic acid groups of GO are usually activated by thionylchloride ($SOCl_2$) [74-76], 1-ethyl-3-(3-dimethylaminopropyl)-carbodiimide (EDC) [77, 78], N, N'-dicyclohexylcarbodiimide (DCC) [79], and 2-(7-aza-1H-benzotriazole-1-yl)-1,1,3,3-tetramethyluronium hexafluorophosphate (HATU) [73]. In this case, amines or hydroxyls are applicable to covalently link functional groups and GO through the formation of amines or esters. This also facilitates the chemically grafting of various biomolecules on GO surface, such

as amine modified nucleic acid or peptide. Epoxy groups (-O-) on the basal plane are possible to be modified via ring-opening reactions. For instance, silane groups can interact with epoxy groups in GO forming mechanically robust silica composites.

For non-covalent interaction, GO can absorb various molecules via different ways, including electrostatic interactions, hydrogen bonding, π-π stacking interactions and hydrophobic interactions. Specifically, electrostatic interactions with charged biomolecules are allowed by ionic groups such as O^- and COO^- located on the planes and edges of GO. Large amount of oxygen groups located on GO surface make GO to be highly hydrophilic, which enables hydrogen bonding network with water molecules. The aromatic scaffold of GO could act as a platform exhibiting non-covalent binding with universal biomolecules, such as single-stranded DNA (ssDNA), aptamer and peptide. Because the basal plane of GO is consisted of aromatic ring arranged by isolated sp^2 network without oxidization, it can interact with the backbone of DNA or peptide via π-π stacking interactions or hydrophobic interactions [80]. The intrinsic π-π stacking property facilitates the fabrication process of biosensors to be free from complex chemical immobilization, such as GO based FRET biosensor and electrochemical biosensor [81, 82].

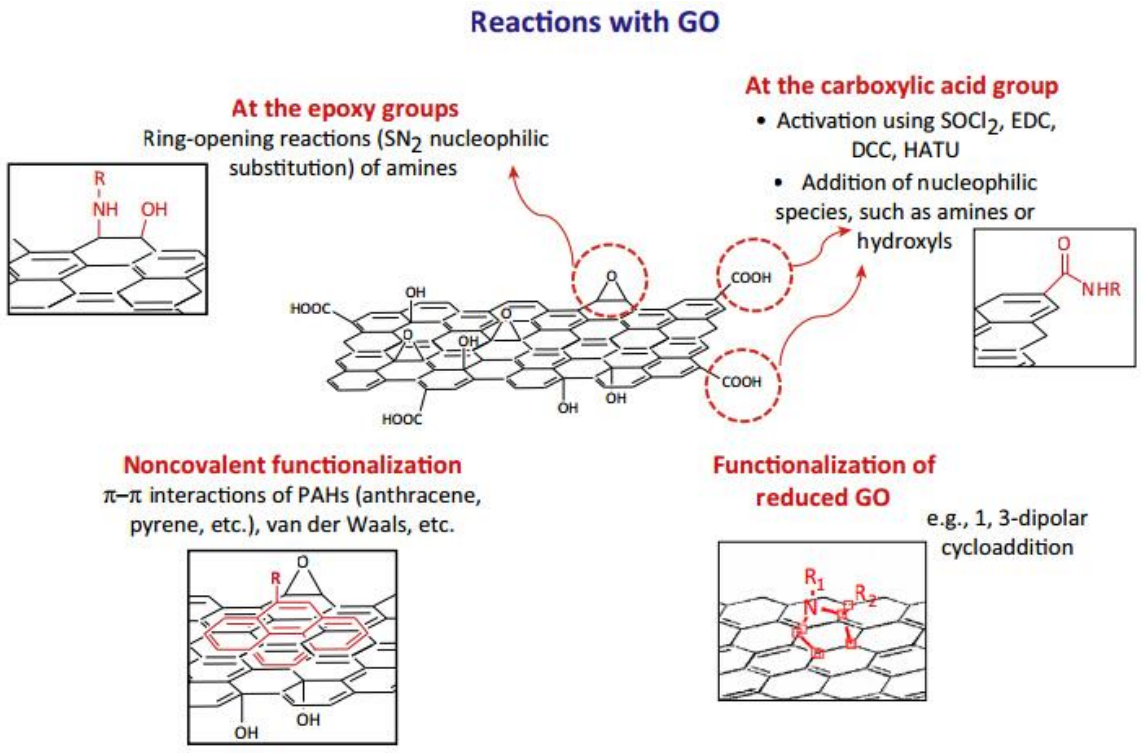

Fig. 1.3.5 Different approaches for the functionalization of GO (Adapted from [73]).

1.3.2.4 Wide absorbance spectrum

GO has a wide absorbance spectrum, which centers at UV region with a long extension up to 800 nm (Fig. 1.3.6) [37, 83]. The characteristic absorption peak at 229 nm is attributed to π-π* transition of C=C bonds, a small shoulder peak around 300 nm is owing to n-π* transition of C=O bonds. The wide absorption band ranging from 200 to 800 nm benefits GO to be independent from the emission spectra of donor in FRET assay.

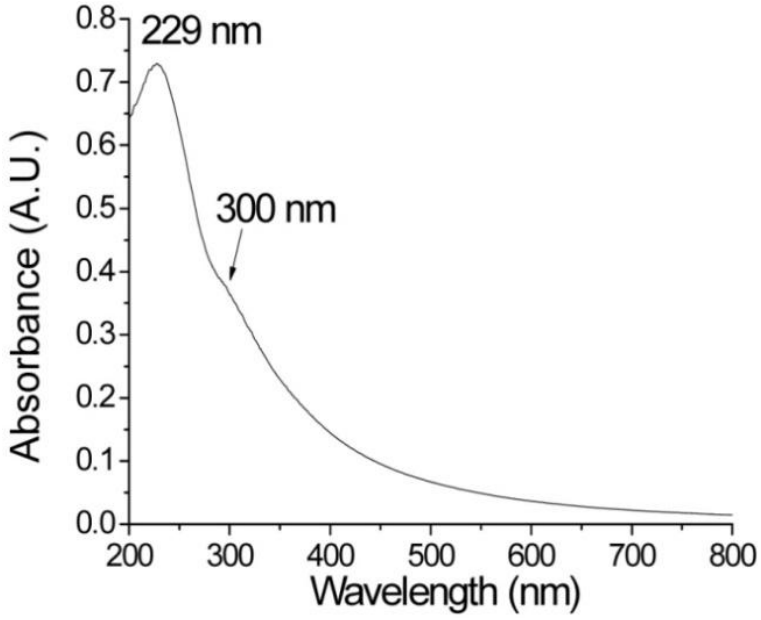

Fig. 1.3.6 Absorption spectrum of GO (Adapted from [83]).

1.3.2.5 Super quenching ability

In previous works, Kagan et al. demonstrated that graphitic carbon with numerous adsorption sites could adsorb varied molecules and permit elimination of fluorescence from dye molecules [84]. Thus, in the same principle, graphene oxide (GO), a 2D atomically thin structure of carbon lattice with functional groups exposed on the edges or basal plane, could acted as a super nano quencher for universal fluorescent dyes because of its unique heterogeneous electronic structure and its wide absorption band (200-800 nm) [83]. It is reported that the GO could quench universal fluorescence molecules, such as organic fluorescent dyes [6, 80, 83, 86-87], fluorescence proteins [9], and quantum dots [10, 11]. The reason for this extraordinary quenching property can be complex. As described in section 1.3.1, GO maintain residual graphene-liked properties by isolated sp^2 domains on the basal plane, which are mainly responsible for fluorescence quenching [85]. Thus, the quenching ability of GO can be remarkably

enhanced via the reduction and surface modification procedures, which could restore the fraction of sp^2 cluster (Fig. 1.3.7) [6]. Meanwhile, the wide absorption band of GO allow FRET to occur without restrict engagement in some degree. The thin film structure with large contact area makes GO to be a perfect candidate for multiple fluorophores' acceptors in FRET sensing [11]. Additionally, as an excellent quencher, GO provides longer range resonance energy transfer with a higher FRET efficiency comparing to typical FRET [87] (details will be described in Section 1.4.2.4). Kim et al. observed an effective quenching effect of fluorescence dye molecules by GO with polystyrene polymer interlayer, which was around 20 nm thick [6]. Swathi et al., calculated that the distance for efficient quenching was as long as 30 nm in the presence of GO [88, 89]. Therefore, GO based biosensor associated with enhanced FRET effect has been widely used for sensitive detection of ssDNA, ions, peptide or other biomolecules [10, 11, 86-87, 90, 91].

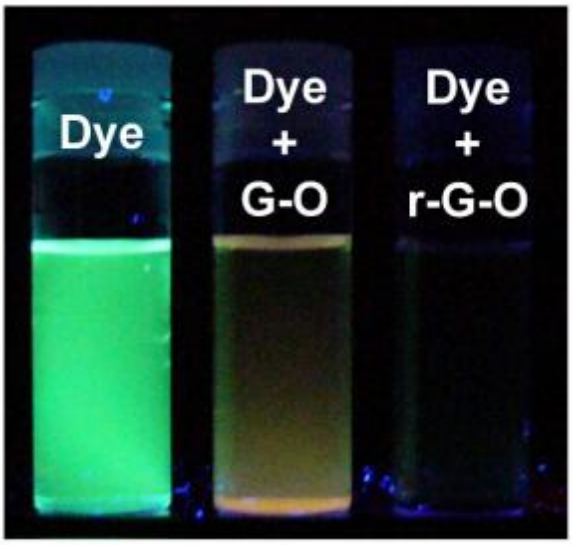

Fig. 1.3.7 Fluorescence image of fluoresce in solution with GO and reduced GO (Adapted from [6])

1.4 GO or GQDs in FRET biosensing applications

1.4.1 GQD as a donor in FRET biosensor for mecA sequence of Staphylococcus aureus

1.4.1.1 Staphylococcus aureus

Staphylococcus aureus (*S. aureus*) is a bacterium with appearance of golden-yellow grape-like clusters, discovered by the surgeon Alexander Ogston in Scotland at 1880 (Fig.1.4.1) [92]. *S. aureus* usually exists in the environment, especially in food. Miao et al. claimed that *S. aureus* has become the second major bacteria in food-borne pathogens for food poisoning, which threatens the health of both human and animals [93]. According to the USDA's economic research service, the infectious foodborne illness caused by staphylococcus poisoning is over 180 thousand cases annually in US [94]. Symptoms of staphylococcal food poisoning include nausea, vomiting, abdominal cramps, and diarrheal that last for 1 to 2 days, and it usually takes several days to recover completely [95].

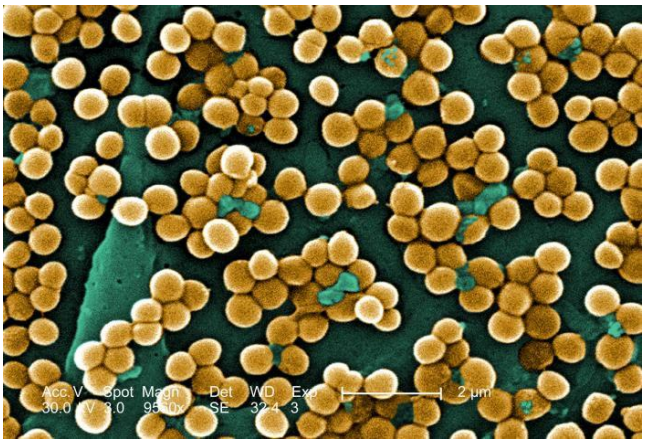

Fig. 1.4.1 Image of Staphylococcus aureus under 9500X microscope.

1.4.1.2 Existing detection systems for staphylococcus aureus

Traditional methods to detect *S. aureus* in food samples are usually complex, expensive, time-consuming and labor-intensive. Generally, bacteria isolation is sensitive and inexpensive but bears the limitation of time-consuming and labor-intensive procedures [96-98]. Immunological assay such as enzyme-linked immunoabsorbent assay (ELISA) is a rapid method but suffers from relatively low sensitivity [99-101]. Although PCR is powerful method with the LOD for *S. aureus* DNA at pM scale, it has some inevitable drawbacks [102-104]. It is susceptible to contamination due to its amplification nature, and hence the sample must be handled with great care. Moreover, PCR can hardly be applied to point-of-care use owing to its cumbersome set-up. Other limitation also includes expensive equipment, long testing time, and demanding technical skills.

In the past decades, nucleic acid biosensors based on DNA hybridization enable the direct, sensitive, and rapid detection of bacterial DNA via different sensing techniques, such as fluorescence [105-106], electroluminescence [107], quartz crystal microbalance (QCM) [108] and surface plasmon resonance (SPR) [109]. Among them, the fluorescence detection method has played an important role in detection of *S. aureus* due to the advantages of easy operation, direct readout and good specificity [105, 106]. However, the sensitivity of optical detection method is relatively low with LOD from tens of nM to mM, because typical fluorophores, such as organic dyes and fluorescence proteins, always have low fluorescence brightness and short fluorescence lifetime, which are not that suitable for reliable and long term detection [110]. Considering the significance of quality management in the food safety, the methods used for bacterial

contaminants detection need to be simple, sensitive, and reliable. Therefore, there remains a demand to develop a simple detection method of *S. aureus* with good sensitivity.

1.4.1.3 GQDs as a donor in FRET biosensor for mecA sequence of Staphylococcus aureus

In most recent years, graphene quantum dot (GQD) has received considerable attentions due to its high brightness, good photo-stability, better surface grafting and non-toxicity [39-55]. Dong et al. demonstrated that GQDs can be excited with a short-wavelength light source, usually in the UV region which is far away from acceptor emission spectrum and thus acceptor excitation can be minimized. Considerable research has demonstrated the strong and stable photoluminescence of GQDs, the color of PL could be blue, green and yellow according to different fabrication and modification methods [40, 42, 45, 47]. Zhu et al. observed stable brightness of GQDs under continuous excitation for more than 20 min, which highlights the long fluorescence life-time of GQDs with negligible photobleaching effect [30]. On the other hand, the low cytotoxicity of GQDs is remarkable, according to Zhu et al. and Hu at al., MTT assay indicated that cells remain activity in the presence of additional 400 μg GQDs [30, 47], thus GQDs are more suitable for biological assay due to its biocompatibility. Moreover, as carbon based luminescent nanomaterials, GQDs possess easy fabrication method with relatively low cost. However, most studies are focused on facile fabrication method for GQDs in recent years, the further biomedical applications for GQD just get started to make a figure, such as bioimaging [30, 41, 47, 48], biolabeling [45, 52] and drug/gene

delivery [48, 53]. Therefore, GQDs are perfect fluorescence donors for reliable FRET system to detect *S. aureus* DNA, However, the usage of GQD based FRET sensor for *S. aureus* DNA detection has not been explored.

1.4.2 GO as an acceptor in FRET biosensor for bacterial protein toxin (BoNT-LcA) and circulating tumor cells (CTCs) detection

1.4.2.1 Bacterial protein toxin (BoNT-LcA)

Botulinum toxin is protein neurotoxin produced by the bacteriumClostridium botulinum, which is first discovered as a contaminant of poorly preserved ham in the last 19th century [111]. It is considered to be the most widely known toxic substance in the world, and has the potential to be used as biological weapon [112]. The human median lethal dose (LD-50) of BoNTs is 10–13 ng/kg when inhaled [113]. There are seven serotypes of botulinum neurotoxins (A to G), among which BoNT serotype A (BoNT/A) is the most commonly involved in human illness. The toxicity caused by botulinum neurotoxins is called botulism, a serious and life-threatening paralyticillness. On molecular level, BoNTs neurotoxicity results from the cleavage of SNARE complex proteins which are critical for the release of neurotransmitter acetylcholine (ACh) from neuronal cells [114]. BoNTs consist of a heavy chain and a light chain connected by a disulfide bond. The heavy chain acts as a facilitated transmission unit and the light chain is mainly responsible for toxicity [115] (Fig. 1.4.2). Therefore, there remains an urgent need for a portable and rapid detection system of BoNT/A light chain (BoNT-LcA) in early stage.

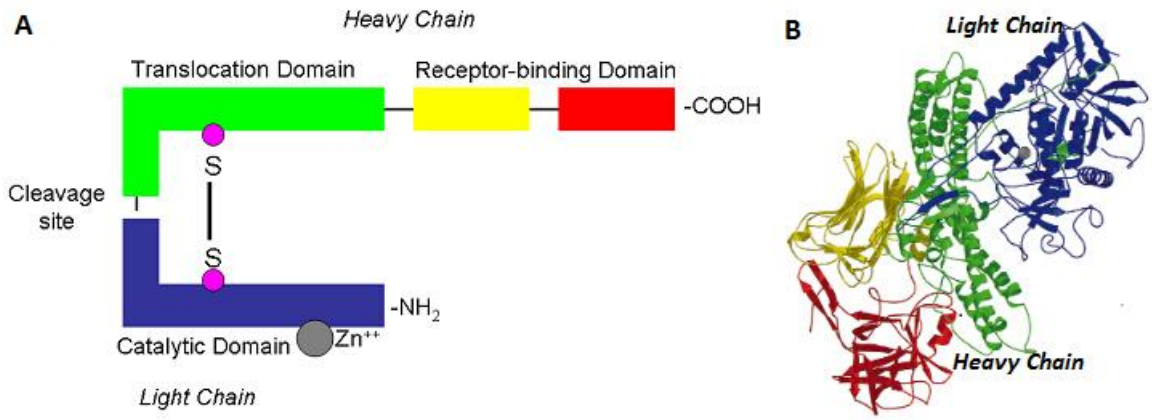

Fig. 1.4.2 Schematic representation of BoNT (A); Crystal structure of BoNT/A –PDB code: 3BTA (B) (Adapted from [115]).

1.4.2.2 Existing detection systems for BoNT-LcA

In previous studies, mouse bioassay is most commonly used and considered to be gold standard in laboratory test [116], which provides high sensitivity and reliability for BoNTs activity detection. Although mouse bioassay owns the detection limit of 1 MLD50 (20 pg/ml) for BoNT/A [117], It is still hampered by time-consuming (4-6 days), laborious procedures and expensive equipment. In this case, several *in vitro* immunoassays have been noticed, such as enzyme-linked immunosorbent assays (ELISA) [118, 119], immune-magnetic beads [120, 121], immune affinity column [122, 123] and immune-sensors [124-125]. Most immunoassays are based on the binding of antibody to the toxin strategy, and usually equipped with a faster (4-9 hours) and similar sensitive (5pg/ml~2ng/ml) performance in contrast to mouse bioassay. However, immunological assays cannot provide the activity information of BoNT-LcA protease, which means they can only detect the presence of toxin rather than the active form or inactive form of the toxin. In order to solve this problem, BoNT-LcA protease activity

assays, based on the toxins' ability to cleave specific SNARE proteins, have been developed via various detection methods such as mass spectroscopy [126], surface plasma resonance [127], and fluorimetric methods [128, 129].

Among various activity assays, fluorescence resonance energy transfer (FRET) based methods are promising with the advantage of simplicity and direct response [130-131]. For FRET assays, the existence of toxin and its enzyme activity can be determined simultaneously by fluorescent signal transduction upon one-step addition of target toxin. For instance, Gilmore et al. generated an assay combined both FRET and fluorescence polarization (FP) principle using a long SNAP-25 substrate flanked green fluorescence protein (GFP) and blue florescence protein (BFP). Before BoNTs cleavage, BFP emitted energy can transfer to GFP under excitation of 387 nm, leading to green emission at 509 nm. On cleavage by BoNTs, the FRET is abolished and emission of GFP is polarized. By monitoring the change of fluorescence emission, the activity of BoNT/A or BoNT/E can be detected (Fig. 1.4.3). However, such FRET assays for BoNT-LcA enzymatic activity detection suffer from poor sensitivity with LOD in the scale of ng/mL [130-133]. The fluorescence transfer efficiency of organic fluorophores is largely dependent on short-range distance while the cleavage activity of BoNT-LcA requires quite a long substrate sequence for cleavage on SNAP-25 peptide [134]. Moreover, the current FRET assays for BoNT-LcA enzymatic activity detection rely on single-donor versus single-acceptor configuration which has relatively low FRET transfer efficiency. Therefore, there remains an urgent need of efficient FRET assay for the detection of BoNT-LcA protease enzymatic activity with a high sensitivity and selectivity.

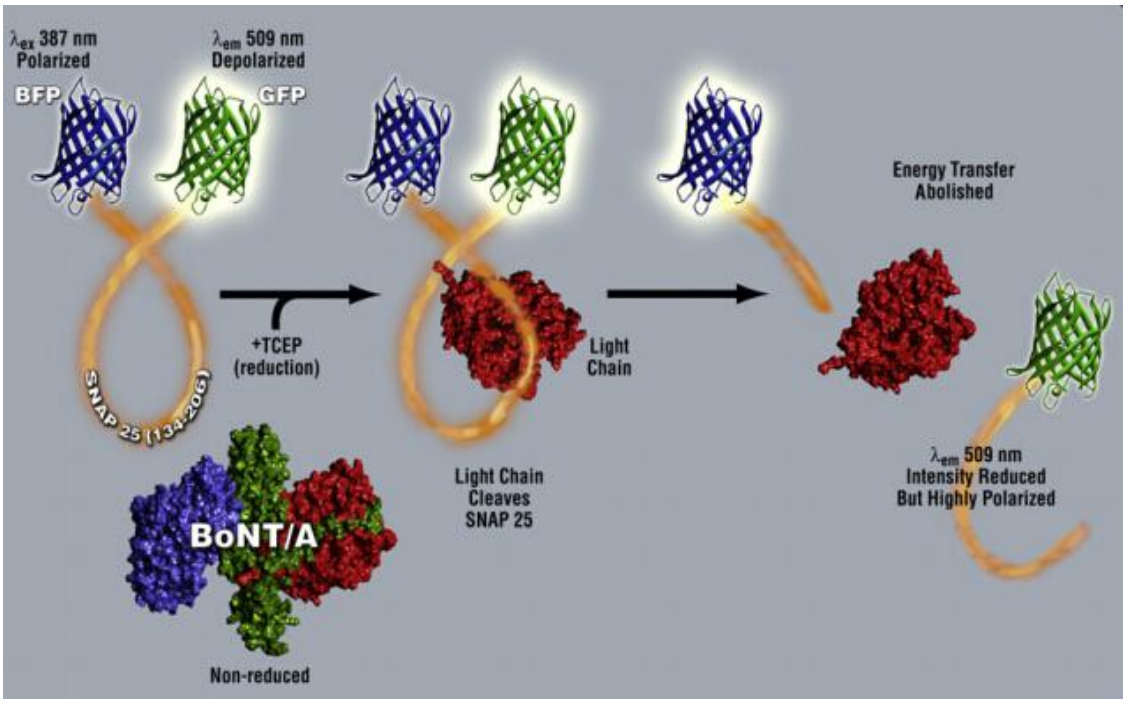

Fig. 1.4.3 Depolarization after resonance energy transfer assay for BoNT/A or BoNT/E activity detection (Adapted from [131]).

1.4.2.3 Circulating tumor cells (CTCs) in breast cancer and their existing detection systems

Circulating tumor cells (CTCs) are cells which derive from clones in the primary tumor and spread throughout the body circulating in the bloodstream. They are considered to be potential biomarkers in cancer prognostic and diagnosis due to the carried information of the primary tumor cells. Currently, the most frequently and intensely studied tumor-associated antigens is considered to be epithelial cell adhesion molecule (EpCAM), which is a glycosylated membrane protein expressed on the surface of CTCs [135]. EpCAM is overexpressed in most cancers, including colorectal cancer [136], breast cancer [137], gallbladder cancer [138], pancreatic cancer [139] and liver

cancer [140]. Thus, EpCAM has been regarded as a prognostic tumor antigen candidate for cancer diagnosis, prognosis, imaging, and therapy [135]. This thesis is focused on CTCs detection in breast cancer.

Breast cancer is a malignant tumor, usually developing from the tissue of breast. Women have100 times more chances to acquire this disease than men [141].According to World cancer report 2014, there were 1.68 million cases of breast cancer and 522000 cases of deaths in 2012[142]. Hence, there is an urgent need for rapid and efficient diagnosis of breast cancer cells in early stage. Unfortunately, although scientists have made numerous efforts to develop a sensitive and selective detection of breast cancer cells, it still remains to be a continuous challenge for early cancer diagnosis due to the low CTCs concentrations presented in blood and the complex compositions of blood [143]. Previously, cytometry techniques, nucleic-acid based techniques (PCR) and a combination method of both had been widely used for EpCAM based CTCs detection in breast cancer [144,145]. But they all suffered from the disadvantages of long analytical time, labor-intensive operation and expensive instruments, which hamper the development of point of care diagnosis [146]. Besides, the majority of EpCAM-based diagnostic and therapeutic approaches were relied on anti-EpCAM antibody, which failed to provide objective clinical response because of the large size and instability of antibody [147-149]. Therefore, small sized aptamers have been noticed. According to Song et al., specific aptamer–cell affinity interaction between EpCAM aptamer and EpCAM protein expressed on the membrane of tumor cells can be used to achieve early diagnosis of breast cancer cells [150]. Recently, fluorescence resonance energy transfer (FRET) based methods were promising with the advantage of simplicity and direct

response. Bagalkot et al. firstly reported a novel bi-FRET complex system between QD-aptamer and doxorubicin (Dox) for drug delivery and prostate cancer cells imaging (Fig. 1.4.4) [151]. The binding between QD-aptamer and Dox could trigger the self-quenching effect of QD-aptamer conjugate, and then the release of Dox inside cells would restore the fluorescence intensity of both QD and Dox, making it feasible for cancer cell image. This multifunctional nanoparticle-aptamer conjugate based FRET biosystem initiated a new method for cancer cells detection at a single cell level with sensitivity and specificity. It is of no doubt that this method still needs further efforts to realize effective cancer cells sensing with improved reliability and sensitivity.

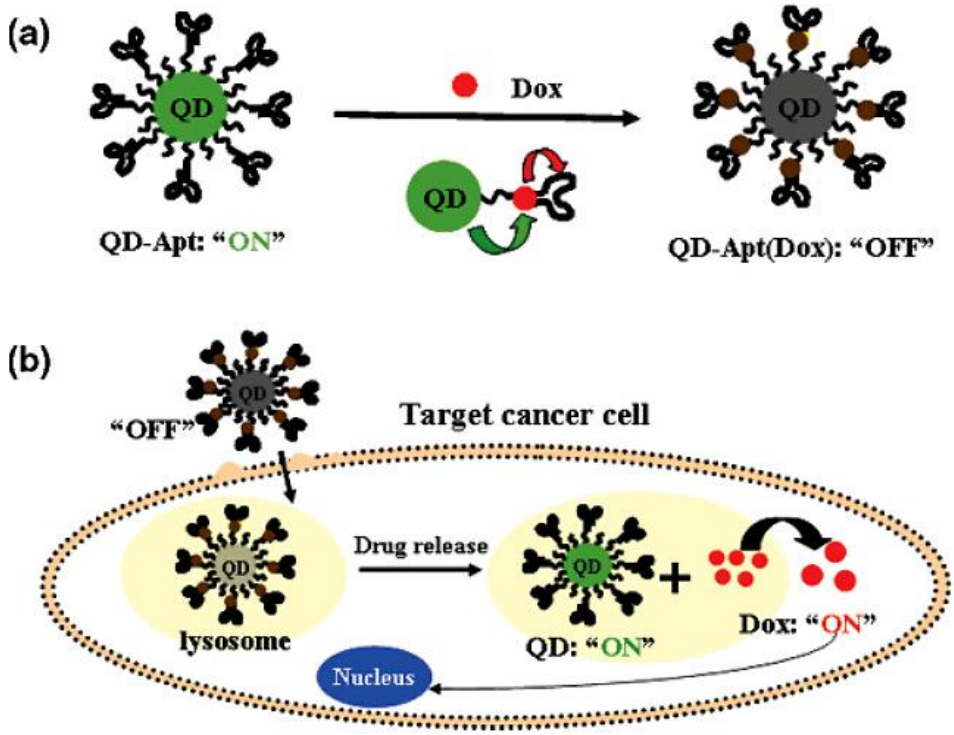

Fig. 1.4.4 Schematic mechanism of QD-Apt (Dox) Bi-FRET system in extracellular (a) and in intracellular (b) (Adapted from [151]).

1.4.2.4 GO as an acceptor in FRET biosensor for BoNT-LcA protease activity and MCF-7 breast cancer cells detection

As a promising candidate in biotechnology development, GO has been widely used as an acceptor in FRET biosensing studies due to its super quenching ability and long-range working distance. According to Swathi et al., the efficiency of resonance energy transfer between the fluorescent species and graphene with a $(distance)^{-4}$dependencewas higher than traditional FRET with $(distance)^{-6}$ dependent efficiency [88, 89].The effective working distance of GO quenching effect was calculated to be as long as 30 nm [88, 89], which was three times larger than that of conventional FRET. Similar super quenching ability of GO was also reported by Hung and Liu [152], they used varied DNA length to investigate distance dependent effect of GO in FRET, and the results was consistent to Swathi et al.'s calculation. Besides, Wang et al. claimed that GO could achieve nearly 100% fluorescence quenching from FAM-aptamer in five minutes [153].

Although the excellent electronic property of GO plays a significant role in super quenching effect, the contribution of 2D structure with high surface-to-volume ratio is not negligible due to the increasing contact area that functioned as FRET acceptors [154]. In another word, GO possess the capability of high loading amount of multiple fluorescent dyes, which is superior to traditional FRET pairs. Moreover, when using GO as an FRET acceptor, it can be free from the emission spectra of donor due to its wide absorbance spectrum [155]. However conventional FRET pairs require a restricted overlapping spectrum between donor emission and acceptor absorption. The super high fluorescence quenching efficiency of GO also conduces to the low background signals in

detection, which improves the sensitivities of conventional FRET biosensor at a large degree. Meanwhile, the low cost of GO as carbon materials gives promising opportunities to the development of GO based FRET biosensor.

Therefore, GO is a perfect quencher choice for peptide substrate and aptamer based long-range FRET system with high energy efficiency to detect BoNT/A protease activities and MCF-7 cancer cells sensitively. However, the usage of GO based FRET sensor for BoNT toxin enzymatic activity detection has not been explored.

1.5 Objectives of the study

Specific objectives of part I include:

- To establish a nanoparticle FRET biosensor based on GQDs and AuNPs for detection of mecA gene sequence of staphylococcus aureus;
- To explore the quenching effect caused by the formation of sandwich structure via co-hybridization between GQDs-oligo, AuNPs-oligo and target DNA;
- To find out the sensitivity, LOD and specificity for detection of mecA gene sequence of staphylococcus aureus using GQDs and AuNPs based FRET biosensor.

Specific objectives of part II include:

- To establish a GO-peptide FRET sensing platform for bacterial protein toxin BoNT-LcA protease activity detection;
- To compare different GO-peptide sensing platforms fabricated by varied methods, and explore the quenching efficiency of GO at various concentrations;

- To explore the real-time cleavage activity of BoNT-LcA on SNAP-25-GFP substrates in this GO based FRET biosensor and to investigate the real food sample applications;
- To find out the detection sensitivity, limit of detection (LOD) and specificity of BoNT-LcA protease activity using GO based FRET biosensor.

Specific objectives of part III include:

- To establish a aptamer/GO nanocomplex based FRET biosensor for MCF-7 cancer cells detection;
- To explore the quenching effect caused by GO at various concentrations and find optimal ratio of aptamer/GO nanocomplex;
- To find out the detection sensitivity, LOD and specificity for MCF-7 cancer cells in this FRET biosensor.

Chapter 2 Methodology

2.1 A FRET biosensor based on GQDs and AuNPs for the detection of mecA sequence of staphylococcus aureus

2.1.1 Materials and instrumentation

Gold (III) chloride trihydrate ($HAuCl_4 \cdot 3H_2O$) and sodium citrate solution were purchased from Sigma Aldrich (St. Louis, MO, US). Graphene quantum dot (GQD) was purchased from Nanjing XFNANO Materials Tech Co., Ltd. (Jiangsu, Nanjing, China).1-ethyl-3-(3-dimethyl-aminopropyl) carbodiimide (EDC) was purchased from Sigma Aldrich. Dithiothreitol (DTT) was purchased from Thermo Scientific Pierce. All of these chemicals were used as received without further purification. A 20-base gene sequence fragment of type II staphylococcal cassette chromosome mecA gene (N315, GenBank: D86934.2) was used as the target DNA. Both labeled and unlabeled DNA oligonucleotide were synthesized and purified by Integrated DNA Technologies (IDT) Inc. (Coralville, IA, US). All the DNA sequences are list as follows: Thiol-modified capture probe (a): 5'-TGATCCCAAT/3ThioMC3-D/-3'; Amine-modified reporter probe (b): 5'-/5AmMC6/AATGACGCTA-3'; 20-mer complementary target to probe (a'b'): 5'-ATTGGGATCATAGCGTCATT-3'; Single-base-mismatched target to probe (C2): 5'-ATTGGGAT**G**ATAGCGTCATT-3'; Double-base-mismatched target to probe (C3): 5'-ATTGGGAT**G**ATAGC**C**TCATT-3'. All oligonucleotide sequences were dissolved in distilled water to prepare stock solution. Gel columns (illustra MicroSpin G-25 Columns) were purchased from GE Healthcare (Piscataway, NJ, USA). The morphology and size of GQDs and AuNPs were observed by JEOL-2100F transmission

electron microscopy (TEM) equipped with an Oxford Instrument EDS system, with the operating voltage of 200 kV. UV absorbance was recorded by Ultrospec^{TM} 2100 pro UV-Visible spectrophotometer (GE Healthcare).

2.1.2 Preparation of gold nanoparticles

Gold nanoparticles (AuNPs) with average size of 15 nm were prepared by the citrate reduction method [156]. Briefly, as AuNPs preparation need an ultra-clean container, aqua regia (mixture of HCl and HNO_3 at a 3:1 ratio) followed by DI water was used to wash a beaker. Then $HAuCl_4$ (3 μL, 14.3 wt. %), DI water (10 ml) and sodium citrate solution (1 ml, 1 wt. %) were added into the baker and boiled with vigorous stirring at 100℃. When the color of boiling solution turned from yellow to wine red, another 15 min was employed for subsequent heating and stirring. Then the reacted solution was left to cool down to room temperature with continuous stirring. The final product, AuNPs solution, was suspended in DI water and stored in refrigerator at 4 ℃.

2.1.3 AuNPs-oligo conjugation

In order to enhance the efficiency of oligonucleotide immobilization on AuNPs, DTT (0.1 M, pH 8.2) was hired to cleave the disulfur linkage of thiol-modified probe oligonucleotide (A1: 5'-TGATCCCAA T/3ThioMC3-D/-3', 64μM) for 40 minutes at room temperature. Then gel-columns (illustra Microspin G-25 Columns, GE Healthcare, UK) were used to purify the activated oligonucleotide with centrifugation at 3,000 rpm for 2 minutes. After purification, the activated oligonucleotide was characterized by UV-

visible spectrophotometer (Ultrospec^{TM} 2100 pro). 500 µL AuNPs prepared before was then mixed with purified oligonucleotide and incubated at room temperature for 24 hours. After 16-hour standing with sodium chloride solution (0.1 M NaCl, 5mM $NaHPO_4$), the product was purified by centrifugation at 13,200 rpm for 30 minutes. The remaining red precipitate at the bottom was collected and rinsed 3 times with DI water to remove the unreacted reagents. The final AuNPs-oligo conjugates were dispersed in DI water and stored at 4 ℃. Fig. 2.1.1 shows the sketch of formation of Au-S linkage between AuNP and the thiol-labeled ssDNA to form AuNP-ssDNA conjugates.

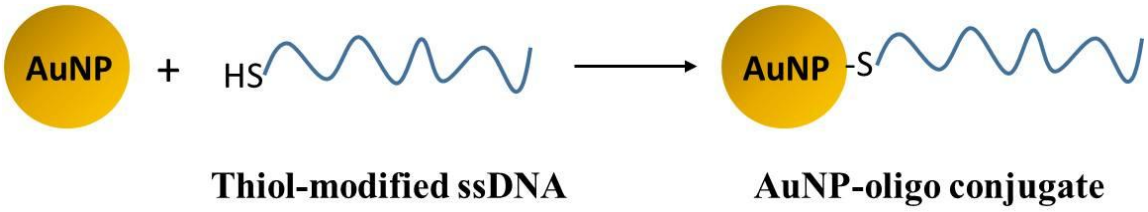

Fig. 2.1.1 Formation of AuNP-oligo conjugates.

2.1.4 GQDs-oligo conjugation

The graphene quantum dot solution (1 mg/mL) was initially sonicated for 10 min. In order to achieve active state of GQDs, EDC (27 mM) solution was added into GQDs suspensions. The mixture was shacked on a vortex mixer for 2 min and bath sonicated for another 15 min. After that, amine-modified capture probe DNA (G1: 5'-/5AmMC6/AATGACGCTA-3', 4.7 µM) was added into the mixture and incubated for 40 min at room temperature. The final product, GQDs-oligo conjugate, was characterized by spectrophotometer equipped with a 450 W steady-state xenon lamp (Edinburgh FLSP920), fluorescence microscope (Nikon, ECLIPSE 80i, Japan), and micro-plate reader (Tecan, Infinite F200, Switzerland). Fig. 2.1.2 shows the sketch of

formation of amide linkage between GQD and the amide-labeled ssDNA to form GQD-labeled ssDNA.

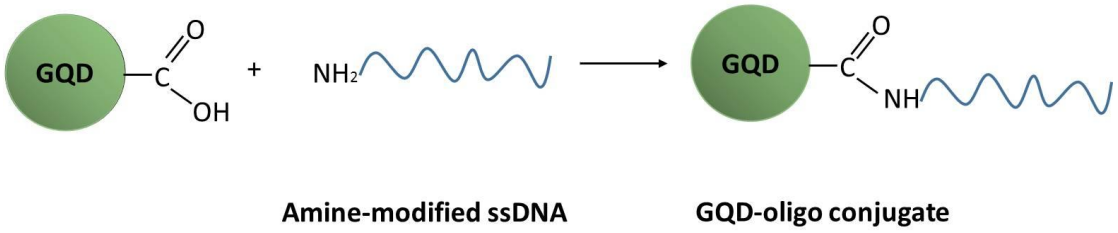

Fig. 2.1.2 Formation of GQD-oligo conjugates.

2.1.5 Quantum yield measurement of EDC modified GQDs

After incubating GQDs with EDC for 15 min, the quantum yield of the EDC modified-GQDs was measured by Edinburgh Instrument integrating sphere and Edinburgh FLSP920 spectrophotometer equipped with a 450 W steady-state xenon lamp (Edinburgh, UK). Firstly, the integrating sphere was installed in a sample chamber, and a quartz cuvette containing only solvent was then inserted into the central position of the integrating sphere. After that, an emission scan of excitation of solvent in the sphere was carried out, and excitation and emission scans of modified-GQDs were collected as well. All the excitation and emission scans were measured under the same condition. At last, the emission curves were integrated for further calculation of quantum yield.

2.1.6 FRET quenching

To investigate the effect of target DNA concentrations on fluorescence quenching efficiency, a fixed amount (1 mg/mL) of GQD-capture probe was incubated with different target probe concentrations (100 pM to 400 nM) for 2 hours to allow DNA

hybridization at room temperature. Then co-hybridized sandwich structure was formed by incubating the above mixture (50 μL) with reporter probe modified AuNP solution (50 μL) at room temperature for 2 hours. After incubation, the fluorescence intensity was measured using the micro-plate reader (Tecan, Infinite F200, Switzerland). All the fluorescence intensity was recorded under the same condition. The specificity of the system was also evaluated with both single mismatched target DNA and double-base mismatched DNA. Fig. 2.1.3 shows the sensing mechanism of the proposed GQDs–AuNPs FRET biosensor for *S. aureus* gene detection.

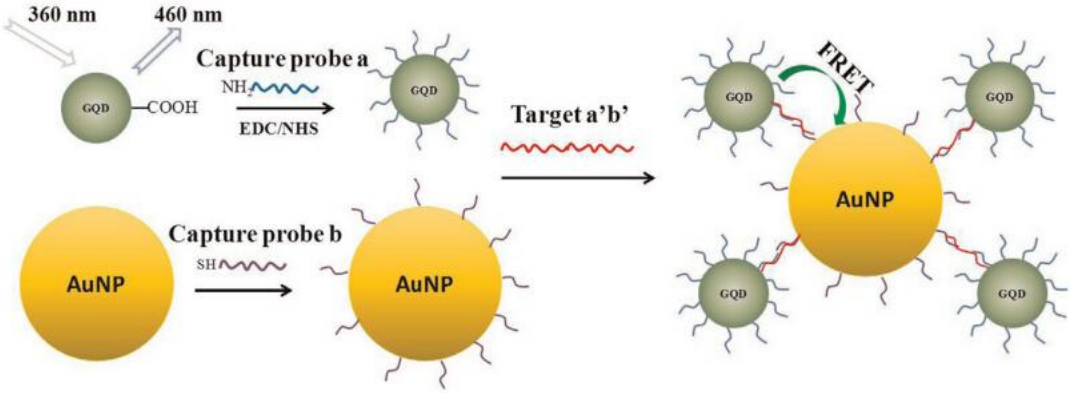

Fig. 2.1.3 The sensing mechanism of the proposed GQDs–AuNPs FRET biosensor for *S. aureus* gene detection.

2.1.7 Characterization of GQDs, AuNPs, GQDs-oligo and AuNPs-oligo

The morphology and size of GQDs and AuNPs were characterized using a JEOL-2100F transmission electron microscopy (TEM) equipped with an Oxford Instrument EDS system, operating at 200 kV. Samples for TEM were prepared on holey carbon coated 400 mesh copper grids. UV-visible spectrophotometer (Ultrospec^{TM} 2100 pro) was used for AuNPs and AuNPs-oligo adsorption spectra measurement. FLS920P

Edinburgh analytical instrument was used for GQDs and GQDs-oligo emission spectra measurement under excitation of 360 nm.

The ζ potential of nanoparticles were determined by a Zetasizer nano ZS from Malvern instruments Corporation at pH=7. Samples (GQDs, GQDs-oligo, AuNPs and AuNPs-oligo) were suspended in DI water and collected in disposable capillary cells respectively. Each sample was conducted thirty measurements of ζ potential in triplicates with 60s delay time at 25℃, and the average data were estimated by Henry approximation from the electrophoretic mobility.

FRET spectra of samples (GQDs, GQDs-oligo, AuNPs, and AuNPs-oligo) were obtained with a Bruker Vertex 70 model Fourier-transform-infrared (FTIR) spectrometer (Bruker, Germany). The conjugated sample of GQDs-oligo was firstly freeze-dried at -55℃ for 24 h. Then, the dried sample was mixed with pre-dried KBr (99+%, Acros Organics, Belgium) at ratio of 1:200. In order to obtain a fine power, the mixture was thoroughly grinded with a pestle in a mortar for 5 min. After further drying process applying at 60℃ for 5 min, the mixture was set up with pressing force between 100 and 120 kN to form a thin disk. Disks containing GQDs, AuNPs, and AuNPs-oligo were also made through the similar procedure. Background spectra were collected before each measurement. Spectra for each disk were accumulated with 32 scans at a resolution of 4 cm^{-1} in the 4000-400 cm^{-1} spectral range. All the spectra were baseline-adjusted and all the measurements were conducted with controlled ambient humidity of 45% RH at room temperature.

2.2 Graphene oxide based FRET biosensor for bacterial protein toxin detection

2.2.1 Materials and instrumentation

GO was prepared from raw graphite flakes using a modified Hummers method. [157] N-hydroxysulfosuccinimide (NHS) and 1-ethyl-3-(3-dimethyl aminopropyl) carbodiimide hydrochloride (EDC) were purchased from Sigma Aldrich (St. Louis, MO, USA). All of these chemicals were used as received without further purification. Skimmed milk and apple juice were purchased from local retailers.

Fluorescence signals for FRET quenching efficiency and BoNT-LcA enzymatic activity assay were recorded using an Edinburgh FLSP920 spectrophotometer equipped with a 450 W steady-state xenon lamp (Edinburgh, UK). Powder X-ray diffraction (XRD) pattern of the as-prepared GO was recorded using a Rigaku smart lab 9 kW (Rigaku, Japan) with Cu Kαradiation (λ= 1.5406 Å). Raman spectra of GO were measured by a Horiba Jobin-Yvon Raman system (Lab Ram HR800) equipped with a 488 nm laser excitation source. Fourier transform infrared spectrum (FT-IR) spectra of GO and GO-peptide conjugate ware collected with a PerkinElmer Spectrum 100 FT-IR spectrometer (PerkinElmer Inc., USA). Zeta potential of GO and GO-peptide conjugate was measured by a ZetaPlus Zeta Potential Analyzer (Brookhaven Instruments Corp., USA). Atomic Force Microscopy (AFM) was performed with a multifunctional Scanning Probe Microscopy (Digital Instruments Nanoscope IV) to observe the formation of GO-peptide complex.

2.2.2 Plasmid construction and protein expression

BoNT-LcA and SNAP-25 were prepared according to the previous research.[158] Briefly, In order to construct the light chain segments (LcA), several methods were applied in the preparation, including amplifying DNA encoding LcA (1-425) of *Clostridium botulinum* serotype A1 hall strain and subcloning into pET-15b. Plasmids for encoding LcA were transformed into *Escherichia coli* BL21 (DE3) RIL (Stratagene). Protein was expressed by *E. coli* cultured in the solution containing 0.75 mM isopropyl 1-thio-B-D-galactopyranoside at 16 ℃ overnight. Then, His-LCs were then extracted from the broken cells and purified by nitrilotriacetic acid-affinity chromatography, gel filtration, and DEAE chromatography. SNAP-25 was constructed by amplifying DNA that encoded the indicated region and subcloning into pGEX-2T. SNAP-25 was encoded by plasmids and transferred into *E. coli* TG1. *E. coli* was cultured with 0.75 mM isopropyl 1-thio-B-D-galactopyranoside at 30 ℃ for 2 h for protein expression. Glutathione-Sepharose 4B affinity chromatography, which was purchased from Amersham Biosciences, was used to purify SNAP-25. In this study, SNAP-25 with specific cleavage site of 197 to 198 was constructed and green fluorescent protein (GFP) was coupled to the C terminus of SNAP-25 to form SNAP-25-GFP substrates (38 kDa) (Fig. 2.2.1). For peptide labeling, The N terminus of SNAP-25-GFP was used to coupled to C terminus of GO by reaction of carboxyl group and amino group to form SNAP-25-GFP substrates.

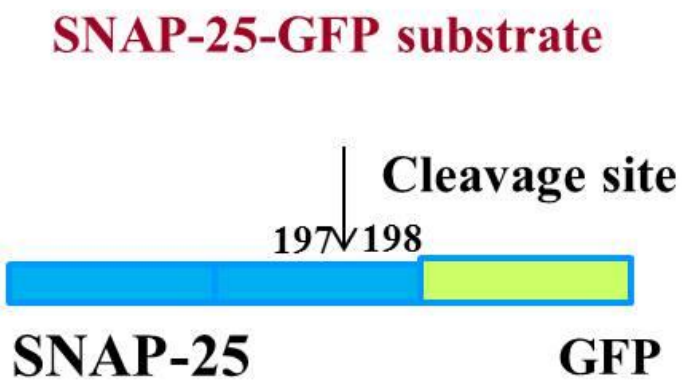

Fig. 2.2.1 Designed GFP conjugated SNAP-25 substrate for GO-FRET sensing.

2.2.3 Establishment of graphene oxide based biosensing platform for BoNT-LcA detection

2.2.3.1 Graphene oxide surface modification

In order to immobilize SNAP-25-GFP peptide substrate onto the GO surface, EDC/NHS chemical method was employed. In detail, initial GO solution with concentration of 5 mg/ml was sonicated for 30 min, and diluted into a series of concentrations ranging from 0 to 120 µg/mL by dissolving in DI water. 5 mM NHS and 1mM EDC were added into as-prepared GO suspensions at various concentrations (40 µL), respectively. After shaking on a vortex mixer for 2 min and a bath sonication for 15 min, the complex stood for 2 hours at room temperature for further use. Therefore, after EDC/NHS activation chemical modification, amine-reactive EDC/NHS esters can be created on any carboxyl-containing molecule on the GO surface.

2.2.3.2 Conjugation of graphene oxide and peptide (SNAP-25-GFP)

To form GO-SNAP-25-GFP conjugates, SNAP-25-GFP (0.12 µg/mL, 20 µL) was added into previously activated GO solution. In order to achieve optimal quenching efficiency, 40 µL GO solutions with increasing concentrations (from 0 to 120 µg/mL) were mixed with 20 µL SNAP-25-GFP at a fixed concentration of 0.12 mg/mL. The complex samples were sonicated in dark environment at room temperature for 1 h to make sure of completely immobilization of SNAP-25-GFP onto GO surface. After that, the products were purified by repeated centrifugation at 100,000 rpm for 30 min to remove the unreacted peptide and excessive EDC/NHS. The centrifugate were then rinsed by DI-water and resuspended in the solution of BSA (0.5 mg/mL) for 30 min at room temperature to passivate the unreacted GO surface. The product was centrifuged again at 100,000 rpm for 10 min and resuspended in the buffer to obtain GO-SNAP-25-GFP complex. Fig.2.2.2 demonstrates the schematic principle of GO and peptide conjugation.

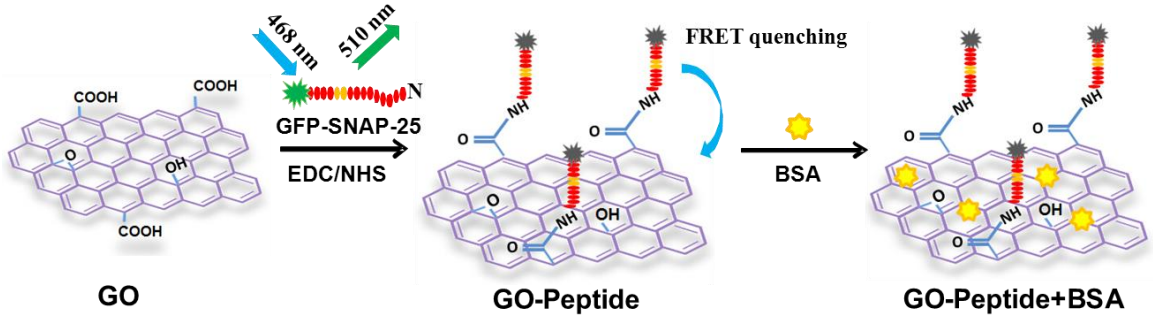

Fig. 2.2.2 Schematic diagram of GO and peptide conjugation.

2.2.4 Characterizations of GO, SNAP-25-GFP and GO- SNAP-25-GFP conjugate

2.2.4.1 XRD and Raman Effect of GO

Powder X-ray diffraction (XRD) pattern of the as-prepared GO was recorded using a Rigaku smart lab 9 kW (Rigaku, Japan) with Cu Kαradiation (λ = 1.5406 Å). Raman spectra of GO were measured by a Horiba Jobin-Yvon Raman system (LabRam HR800) equipped with a 488 nm laser excitation source.

2.2.4.2 FTIR characterization of GO and GO- SNAP-25-GFP conjugate

FTIR spectra were obtained with a PerkinElmer Spectrum 100 FT-IR spectrometer equipped with DTGS (deuterated triglycine sulphate) detector. After the conjugation process between GO and SNAP-25-GFP, the conjugated sample was freeze-dried at -55℃ for 24 h. Then, it was mixed with pre-dried KBr and grinded manually for 5 min till everything up to a fine powder. Further drying process was applied using an oven at 60℃ for 5 min. The thin disk of the mixture was set up with a pressing force between 100 and 120 kN. Disk of GO was made through similar procedure. Background spectra were collected before each measurement. Spectra of each disk were accumulated with 128 scans at a resolution of 1 cm^{-1} in the 4000-450 cm^{-1}spectral range. All the spectra were baseline-adjusted and all the measurements were carried out with controlled ambient humidity of 45% RH at room temperature.

2.2.4.3 Zeta-potential measurements of GO and GO- SNAP-25-GFP conjugate

Samples of GO or GO-SNAP-25-GFP conjugates were suspended in DI water for Zeta-potential measurements. The Zeta potential of all the samples was determined by a Zeta Potential Analyzer (ZetaPlus™) from Brookhaven Instruments Corporation. Sample measurements were recorded at 25 ℃ and pH=7 with a silver electrode using Phase Analysis Light Scattering mode. Ten measurements of ζ potential were collected in the ZetaPlus™.

2.2.4.4 AFM measurements of GO and GO- SNAP-25-GFP conjugate

Sample of single layer GO was prepared onto silicon wafer (size: less than 10*10 mm) by spin coating. Briefly, the Si wafer was cleaned by piranha solution (98% sulphuric acid and 30% hydrogen peroxide at a volume ratio of 4:1) at 200 ℃ for 1 h to remove any contaminants. The cleaned Si wafer was then washed with distilled water and baked at 200 ℃ for 1 h before use. For the formation of single layer sample, GO sample solution was then dropped onto the Si wafer and spin coated at a speed of 3000 rpm for 60 s. GO-SANP-25-GFP thin film was prepared in the same manner. After that, a tapping mode atomic force microscope (AFM) was used to collect thickness and roughness information of sample surface. Nanoscope IV software was further applied for analysis of AFM images.

2.2.5 GO-Peptide FRET Effect and BoNT-LcA Activity Detection

Fluorescence spectra for FRET quenching efficiency and BoNT-LcA enzymatic activity assay were recorded by an Edinburgh FLSP920 spectrophotometer equipped with a 450 W steady-state xenon lamp at room temperature. All the samples were collected in a 350 μL micro-scale quartz cuvette and measured with excitation wavelength of 468 nm and emission wavelength of 510 nm. For FRET quenching experiments, optimal GO concentration for excellent quenching efficiency was obtained by monitoring the fluorescence signal of GO-peptide conjugates with increasing GO concentrations. The change of fluorescence signal reflected the influence of quenching ability of GO distinctly. All the fluorescence spectra were collected under the same condition at room temperature. By observing the FRET effect between peptide and GO, optimal GO concentration of 60 μg/mL had been chosen to perform the BoNT-LcA toxin detection. For FRET restore experiments, the activity of BoNT-LcA protease was monitored by the recovered fluorescence intensity. Specifically, GO-peptide conjugates was mixed and incubated with BoNT-LcA toxin at various concentrations (1 fg/mL, 10 fg/mL, 100 fg/mL, 1 pg/mL, and 10 pg/mL), and the subsequently recovered PL intensity represented the cleavage ability of LcA toxin at different amounts. Time dependent SNAP-25-GFP release effect was further explored by measuring the fluorescence recovery using a micro-plate reader (Tecan, Infinite F200, Switzerland) at room temperature. All the fluorescence spectra and intensity were collected under the same conditions. The whole BoNT-LcA enzymatic activity sensing principle by the FRET biosensor based on energy transfer from GFP to GO was displayed in Fig. 2.2.3.

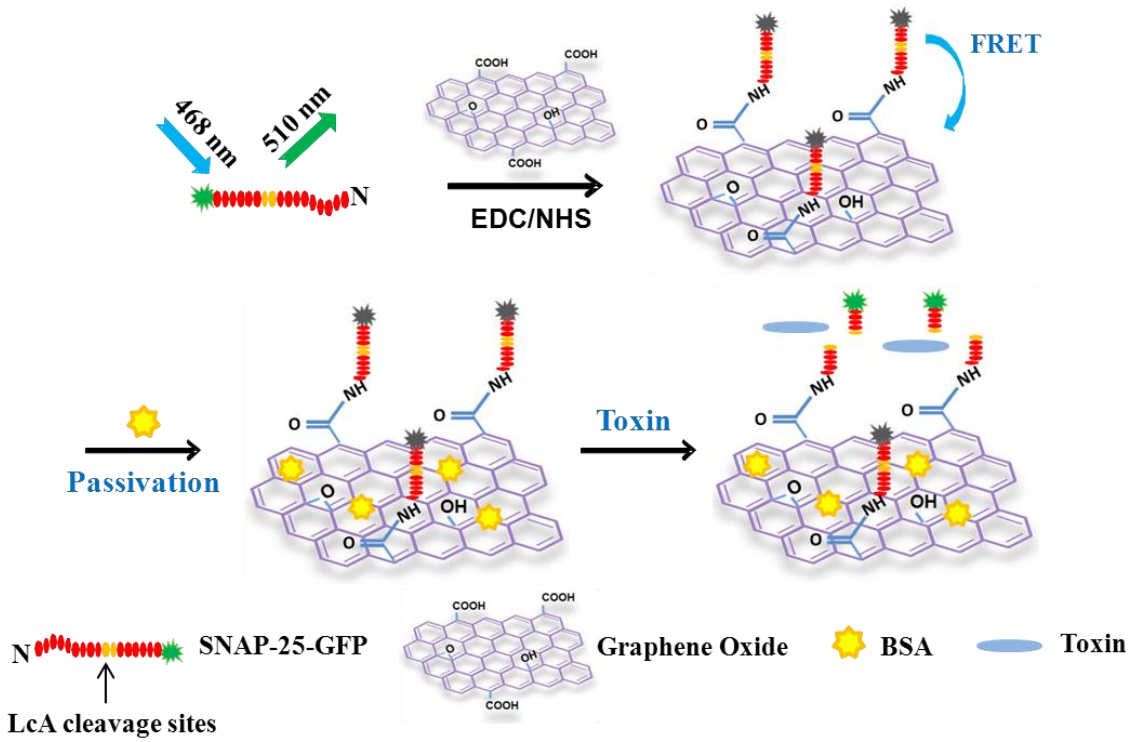

Fig. 2.2.3 Schematic diagram of BoNT-LcA enzymatic activity detection by the FRET biosensor based on energy transfer from GFP to GO.

2.2.6 Fully passivation of GO-peptide conjugate

In passivation experiments, tris buffer and bovine serum albumin (BSA) was used as small and large blocking agents to decrease non-specific binding of peptide to GO surface, respectively. Initially, original GO solution (5 mg/ml) was diluted to 60 μg/mL by tris buffer (PH=7.4), and then BSA (5.2 mg/ml, 2.5 μL) was introduced. After fully passivating the GO surface, SNAP-25-GFP (0.12 μg/mL, 40 μL) were added into the suspension of GO sheets (60 μg/ml, 80 μL) with or without NHS (0.1 M, 6.25 μL)/EDC (0.1 M, 1.25 μL) to achieve covalent GO-peptide conjugates according to previously described conjugation procedures (Section 2.2.3) or simply self-assembly absorption, respectively. In contrast, covalent GO-peptide conjugates with BSA

passivation after modification process was measured as a control group (Fig. 2.2.4). Fluorescence intensity change as a function of time was recorded by a micro-plate reader (Tecan, Infinite F200, Switzerland). All experiments were repeated in triplicate.

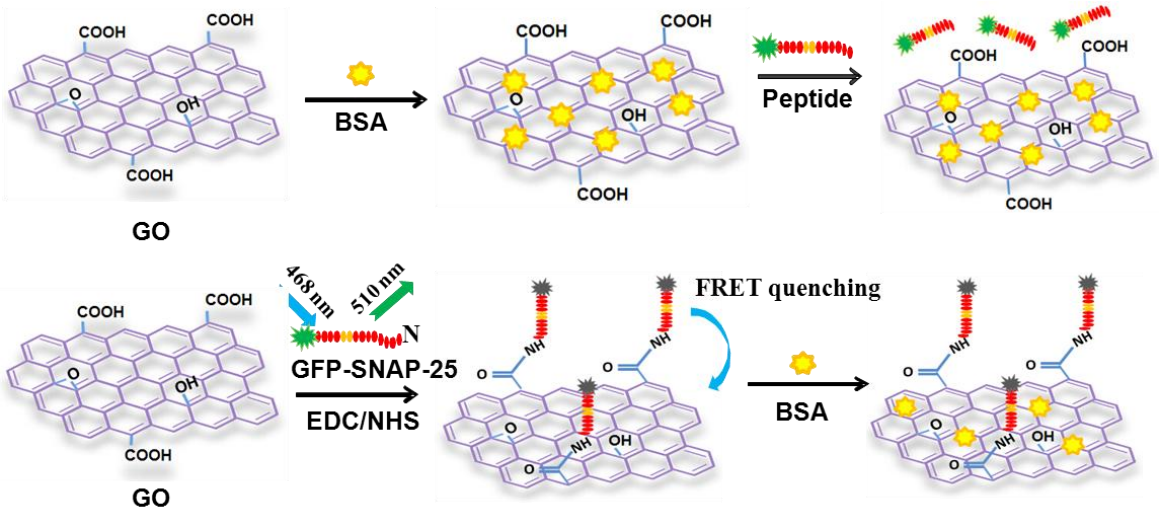

Fig. 2.2.4 GO and peptide conjugation after (Top) and before (Bottom) BSA passivation.

2.2.7 Comparison of the stability of GO-peptide conjugate and peptide-absorbed GO composites

A series of assays were designed to investigate covalent and non-covalent bonding between GO and peptide. Initially, original GO solution (5 mg/ml) was diluted into a concentration of 60 µg/ml by DI water, and GO suspension was sonicated for 30 min before use. To achieve covalent GO-peptide conjugates, NHS (0.1 M, 6.25 µL), EDC (0.1 M, 1.25 µL) and peptide (SNAP-25-GFP, 0.12 µg/mL, 40 µL,) were added into the solution of GO sheets (60 µg/ml, 80 µL) according to previous conjugation procedures (Section 2.2.3). The complex samples were sonicated in dark environment at room temperature for 1 h. To prepare non-covalent complex of peptide absorbed GO, a

self-assembly procedure involving incubation of peptide with GO was applied. GO was mixed with peptide as same weight and volume ratios as before, then, the complex was incubated at room temperature for 1 h. After incubations, additional BSA at final concentration of 0.1mg/ml was added into GO-peptide conjugates and peptide-absorbed GO composites respectively (BSA: 5.2 mg/ml, 2.5 µL). Time dependent fluorescence intensity was recorded by the Tecan Infinite 200 micro-plate reader. All experiments were repeated in triplicate (Fig. 2.2.5).

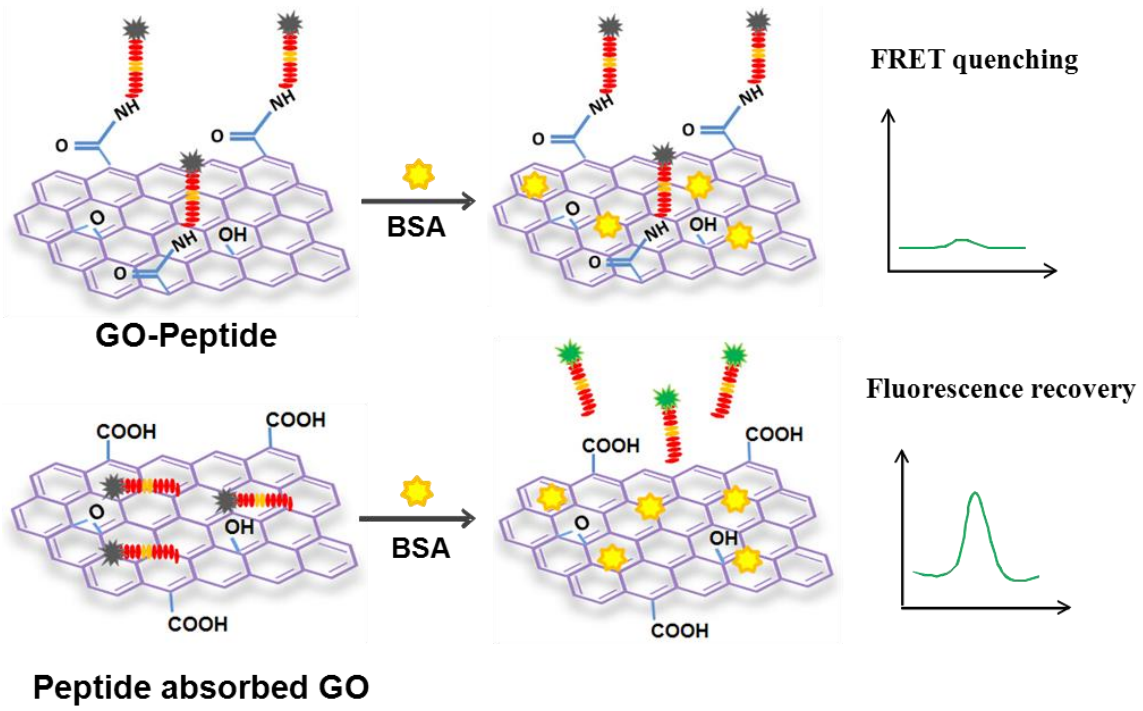

Fig. 2.2.5 (Top) GO-peptide conjugation with BSA passivation. (Bottom); Peptide adsorbed GO with BSA passivation.

2.2.8 Real food sample test

Skimmed milk and apple juice purchased from retailers were employed as real sample matrices to assess bacterial protein toxin (BoNT-LcA) activity. Both skimmed milk and apple juice were used as purchased without further purification. Skimmed milk was diluted to 4% of the original concentration for achieving the transparent solution. The pH value of Apple juice was adjusted to 7.4 by using 10 mM NaOH. Then, the as-prepared GO-peptide sensing platforms were applied to actual food samples, respectively. After 1 h incubation, BoNT-LcA toxin with final concentration of 0.1 mg/ml was spiked into skimmed milk and apple juice, respectively. The fluorescence intensity was measured by the Tecan Infinite 200 micro-plate reader. All experiments were repeated in triplicate.

2.3 Graphene oxide based FRET biosensor for MCF-7 cancer cells detection

2.3.1 Materials and instrumentation

GO was prepared from raw graphite flakes using a modified Hummers method [177]. MCF-7 cell lines were purchased from American Type Culture Collection (ATCC, USA). FAM labeled EpCAM aptamer (5′ FAM-AGC GTC GAA TAC CAC TAC AGT TTG GCT CTG GGG GAT GTG GAG GGG GGT ATG GGT GGG AGT CTA ATG GAG CTC GTG GTC AG-3′) was purchased from Integrated DNA Technology (IDT) Inc. (Coralville, IA, US). Dulbecco's Modified Eagle Medium (DMEM) with 4,500mg/L D-Glucose, Fetal Bovine Serum (FBS, Invitrogen), Penicillin Streptomycin, 0.25% Trypsin/EDTA and Phosphate Buffered Solutions (PBS) were

purchased from Sigma Aldrich (St. Louis, MO, USA). All of these chemicals were used as received without further purification. Fluorescence intensity was measured using the Tecan Infinite F200 micro-plate reader (Tecan, Infinite F200, Switzerland). Fluorescence images were captured by the fluorescence microscope (Nikon, ECLIPSE 80i, Japan).

2.3.2 Cell culture

MCF-7 breast cancer cells were employed in this project. The cells were cultured in a 25 cm^2 cell culture flask with filter cap (SPL Life science co. Ltd, Korea) and incubated at 37 ^oC with 5% CO_2 and 95% air. The routine cell culture medium supplement was consisted of Dulbecco's Modified Eagle Medium (DMEM) with 4,500mg/L D-Glucose, 5% Fetal Bovine Serum (FBS) and penicillin streptomycin (1:1). In accordance to the routine culture, the medium was changed every 2~3 days. When the cells need to be subcultured or harvested, the cell culture flask was firstly wash by sterile phosphate buffered saline (PBS) for three times. Then, trypsin, a proteolytic enzyme, was used to detach adherent cells from the surface of a cell culture flask, this procedure is called trypsinization. The concentration of trypsin/EDTA was 0.25%. The removed cells were subcultured to a new flask for subsequent cell culture.

2.3.3 FAM- EpCAM aptamer/GO nanocomplex based FRET biosensor and MCF-7 cancer cells Detection

Initially, GO solution with 5 mg/ml was sonicated for 30 min, and diluted into a series of concentrations from 0 to 200 µg/mL by dissolving in PBS buffer. The

concentration of FAM-EpCAM aptamer was fixed at 1 μM. Then, in order to obtain optimal quenching effect, 1 μM 50 μL FAM-aptamer was added into 50 μL GO solution with increased concentrations (from 0 to 200 μg/mL) to achieve simply self-assembly absorption of FAM-EpCAM aptamer/GO nanocomplex, respectively. After incubating the nanocomplex samples in dark environment at room temperature for 30min, the fluorescence signals was measured by Tecan Infinite F200 micro-plate reader with excitation wavelength of 465 nm and emission wavelength of 520 nm. All the fluorescence intensities were collected under the same conditions. The fluorescence images of FAM-EpCAM aptamer and FAM-EpCAM aptamer/GO nanocomplex were captured under blue light excitation with exposure time of 1 s by a fluorescence microscope (Nikon, ECLIPSE 80i, Japan), respectively. By observing the FRET effect between FAM-EpCAM aptamer and GO at different ratios, optimal concentration of GO had been chosen to prepare the noncomplex sensing platform for further detection of MCF-7 cancer cells. For FRET restore experiments, The FAM-EpCAM aptamer/GO noncomplex was incubated with additional MCF-7 cancer cells ($2*10^5$ cells/mL, 5μL) at 37 ℃ for 2 h. After incubation, the fluorescence images and florescence intensity were measured under the same conditions as before. The specific affinity interaction between FAM labeled EpCAM aptamer and EpCAM protein overexpressed on the surface of MCF-7 cancer cells were observed corresponding to the change of fluorescence intensity and fluorescence image. The whole MCF-7 cancer cells sensing principle by FAM-EpCAM aptamer/GO nanocomplex based FRET biosensor was displayed in Fig. 2.3.1.

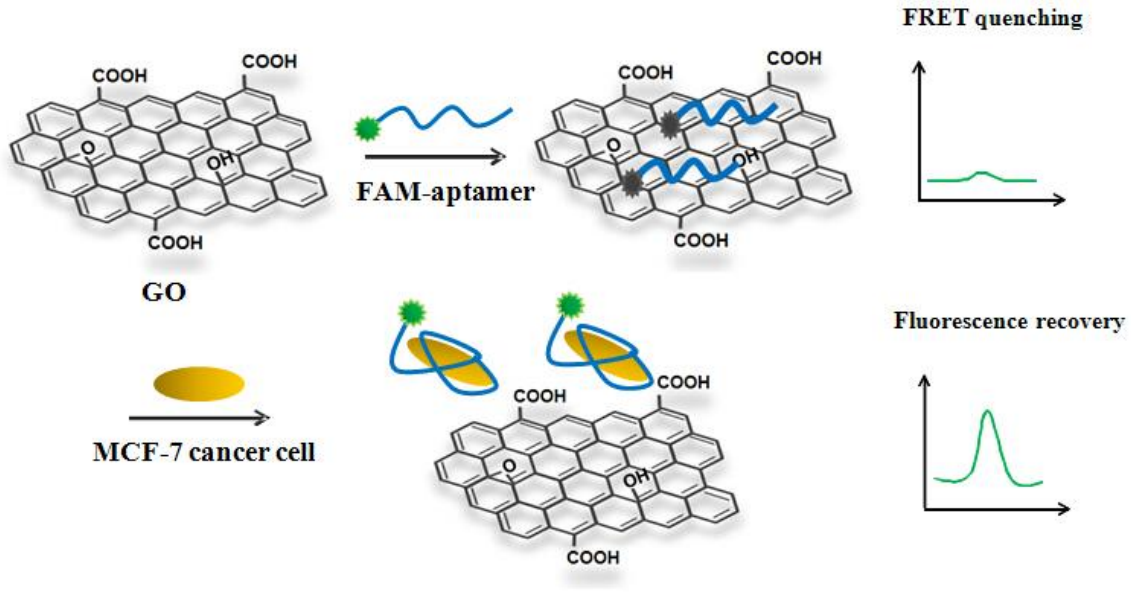

Fig. 2.3.1 Principle of FAM-aptamer/GO nanocomplex based FRET biosensor for MCF-7 cancer cells detection.

Chapter 3 Results

3.1 A FRET biosensor based on GQDs and AuNPs for the detection of mecA sequence of staphylococcus aureus

3.1.1 Mechanism of FRET biosensor

Fig. 2.1.3 shows the sensing mechanism of the GQDs-AuNPs based FRET biosensor for staphylococcus aureus DNA detection. In this part, GQDs and AuNPs were chosen to be the donor-acceptor FRET pair. Initially, GQD was conjugated with amine modified capture probes (a), while the reporter probe (b) was immobilized onto AuNPs surface. The target staphylococcus aureus oligos (a' b') can complementary co-hybridize with capture probes (a) and reporter probe (b), leading to the shortened distance between GQDs and AuNPs for FRET occurrence. The blue emission of GQDs can be absorbed by AuNPs significantly using UV excitation at 360 nm. Base on the change of fluorescence intensity, rapid and sensitive detection of staphylococcus aureus target probes can be achieved.

3.1.2 Characterization of GQDs and AuNPs

The morphology and size of citrate reduction method synthesized AuNPs was characterized by TEM. As shown in Fig. 3.1.1, the synthesized AuNPs exhibit round shape with uniform size at average diameter of 15 nm. GQDs were well dispersed in DI water with average size of 3±1 nm (Fig. 3.1.2). Fig. 3.1.3 shows the TEM image of AuNPs-GQDs system. It exhibits a satellite structure because large AuNPs were surrounded by many small GQDs through oligonucleotide hybridization.

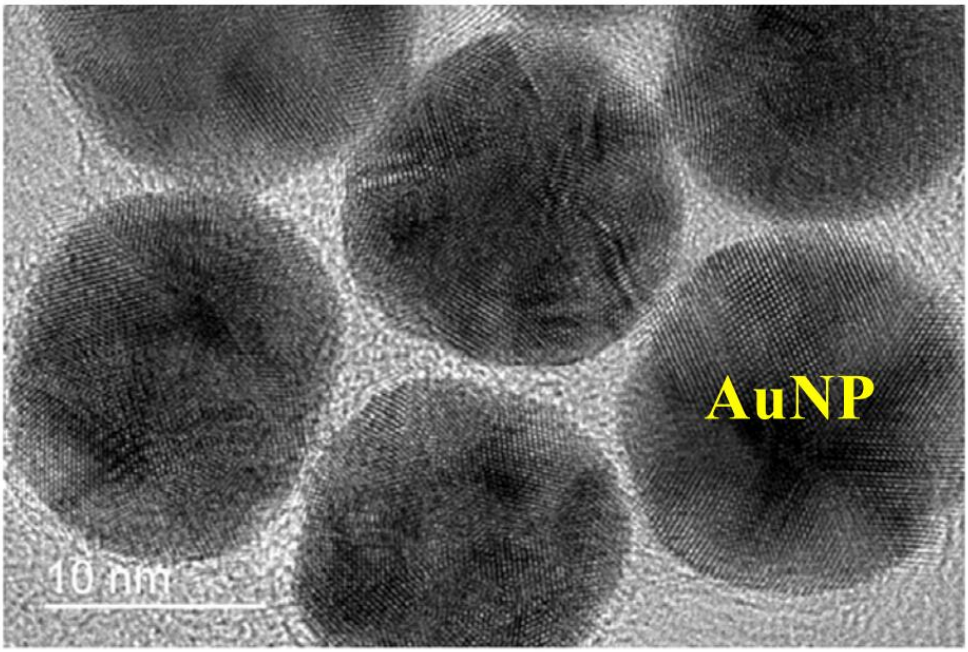

Fig. 3.1.1 TEM image of synthesized AuNPs with average size of 15 nm.

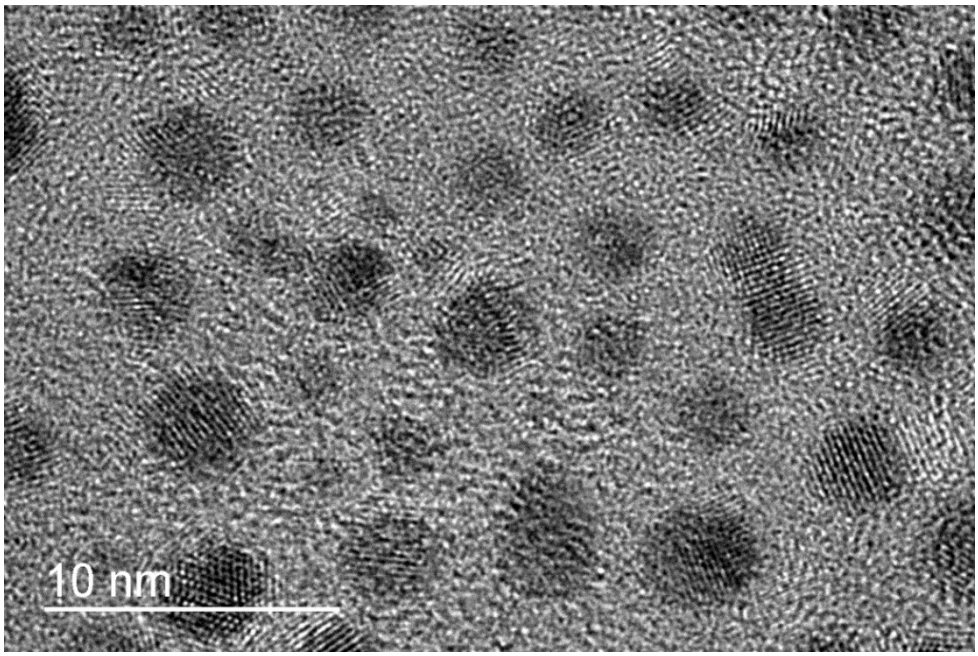

Fig. 3.1.2 TEM image of GQDs with average size of 3 nm.

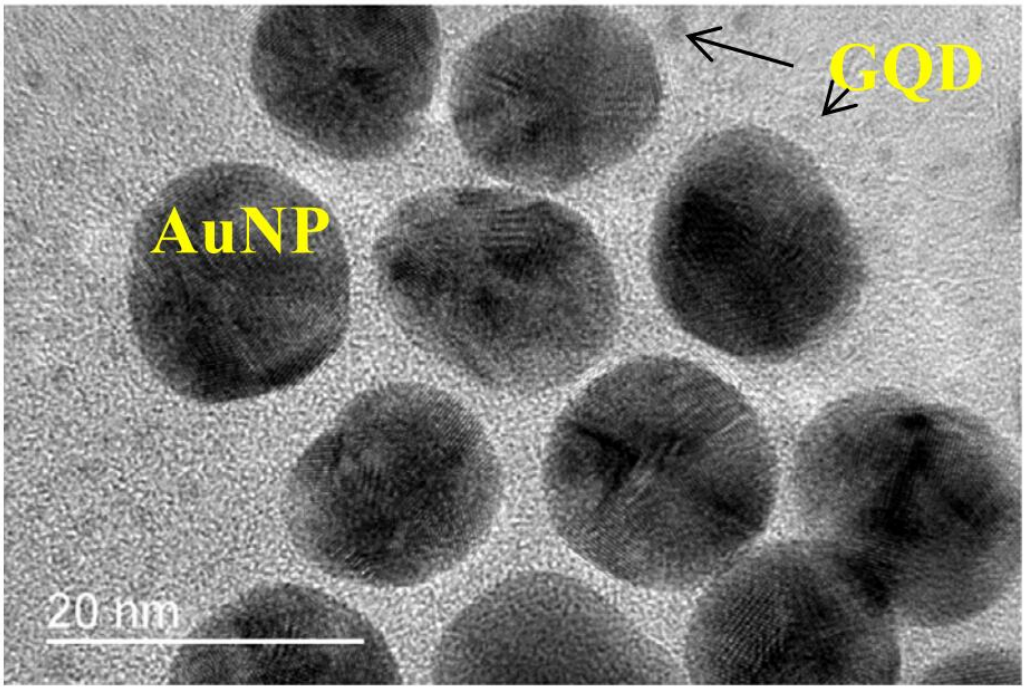

Fig. 3.1.3 TEM image of AuNPs conjugated with GQDs.

3.1.3 Characterization of GQDs-oligo and AuNPs-oligo

3.1.3.1 Zeta potential

The characterization of GQDs-oligo and AuNPs-oligo conjugates can be performed by Zeta potential measurement, which provides the information about the surface electrical charge of particles. As different particles have various isoelectric points, it is possible to confirm the effective conjugation between oligonucleotide and GQDs/AuNPs by measuring the change of surface electrical charge under the same condition. As shown in Fig. 3.1.4, the initial zeta potential values of AuNPs, GQDs and oligos at pH = 7 are -39.5 mV, - 15.2 mV and - 26.6 mV, respectively. After conjugation, oligo probes cover the whole surface of AuNPs and GQDs and the zeta potential of AuNPs–oligo and GQDs–oligo become- 26.5 mV and- 25.5 mV at pH = 7 respectively,

which are close to the zeta potential of pure oligos. The zeta potential measurement results demonstrated the successful conjugation of oligos to AuNPs and GQDs.

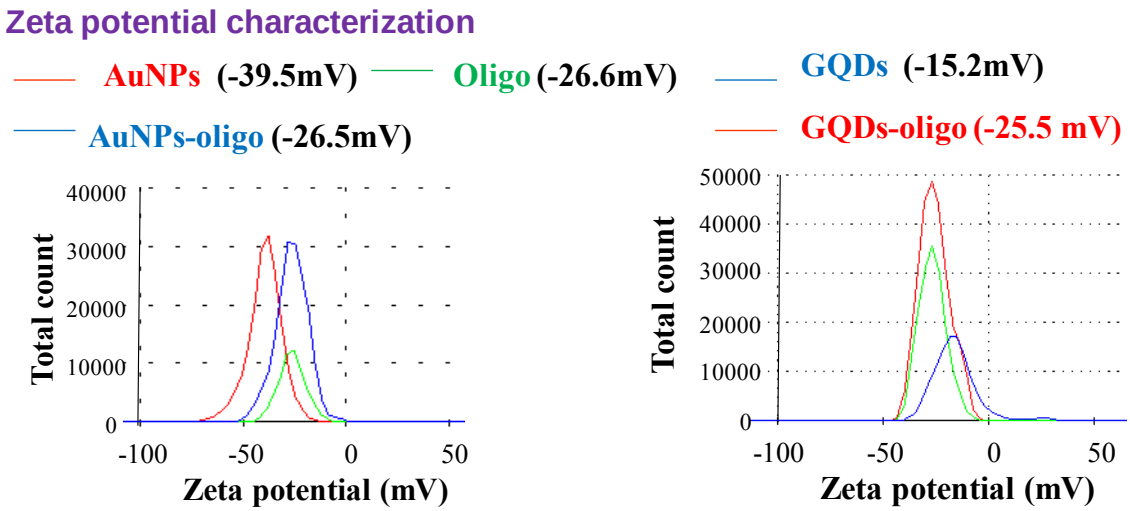

Fig. 3.1.4 Zeta potential measurements of AuNPs, oligo, GQDs, AuNPs-oligo and GQDs-oligo.

3.1.3.2 FTIR spectra

FTIR spectra were also used for conjugation characterization. Fig. 3.1.5 shows the FTIR spectra of GQDs and GQDs–oligo. The most feature characteristic absorptions of GQDs include a broad peak at 3400 cm^{-1} indicating the stretching of –OH groups and a strong band at 1600 cm^{-1} representing the carboxyl groups (-COOH). Moreover, absorption bands at 1400 cm^{-1}, 1087 cm^{-1} s reveal the stretching vibration of C-H and C-O, respectively. After conjugation between oligonucleotide and GQDs, Small peaks appearing around 2900 cm^{-1} stands for -CH_2-streching. The characteristic absorption peaks appear at 1655 cm^{-1} and 1585 cm^{-1} indicating the presence of amide vibration, which confirms the successfully formation of the amide bond between GQDs and amine modified oligonucleotide via EDC/NHS method. The feature band of oligonucleotide

appearing at 1116 cm^{-1} stands for the vibration of symmetric phosphate (PO^{2-}). Additionally, absorption peak at 1060 cm^{-1} is typically assigned to the C-O stretch of DNA backbone and absorption band at 965 cm^{-1} is as an indication of P–O stretching.

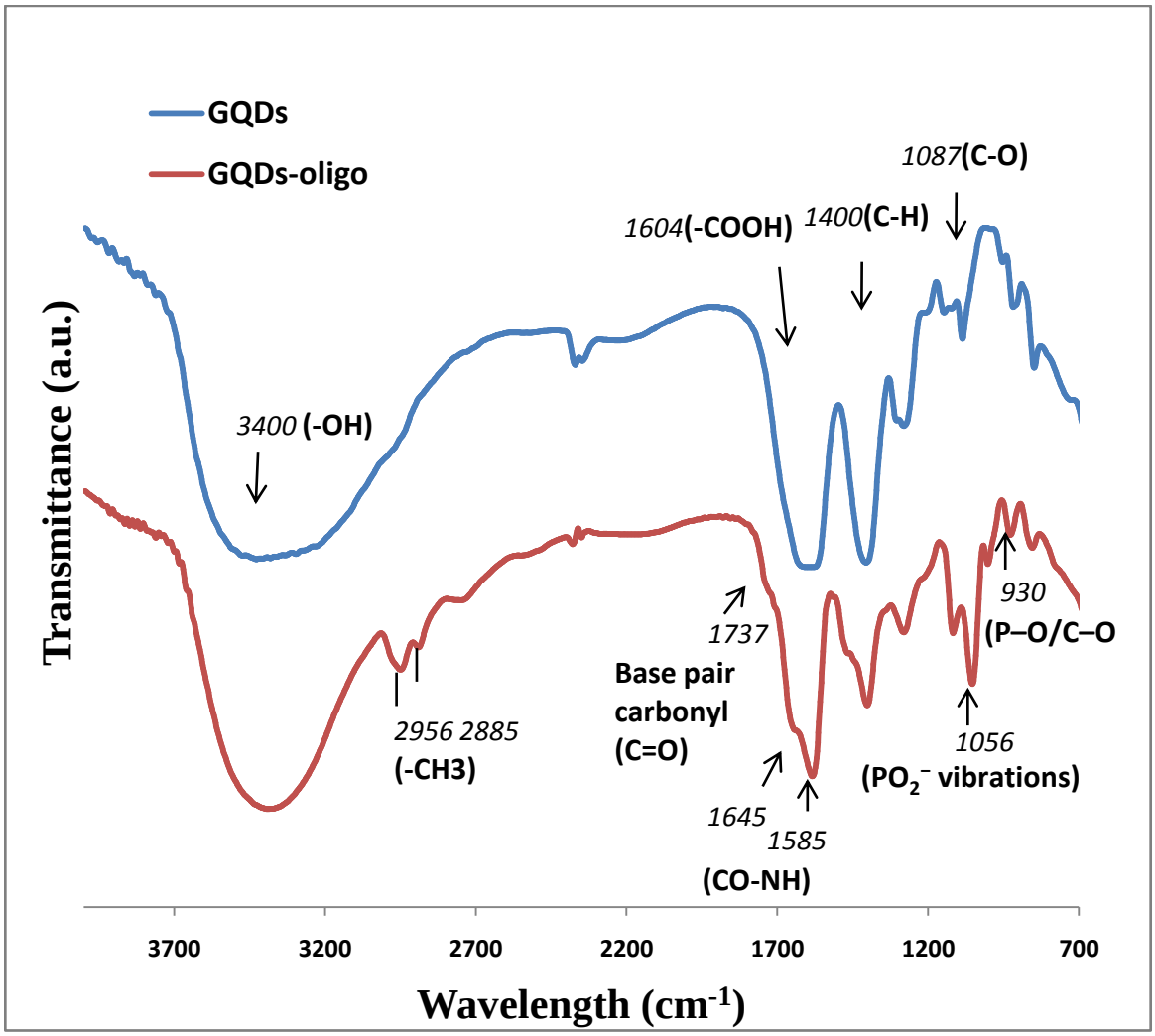

Fig. 3.1.5 FTIR spectra of GQDs and GQDs-oligo.

Fig. 3.1.6 shows the FTIR spectra of AuNPs and AuNPs–oligo. AuNPs show the presence of both carboxyl groups (–COOH, 1600 cm^{-1}) and hydroxyl functional groups (-OH, 3400 cm^{-1}). After oligo conjugation, AuNPs–oligo shows characteristic vibration bands from 1250 cm^{-1} to 850 cm^{-1} assigned to the phosphate groups of oligos and small

peaks around 2900 cm^{-1} indicating the $-CH_2-$ stretching, which confirm the conjugation of oligos onto AuNPs.

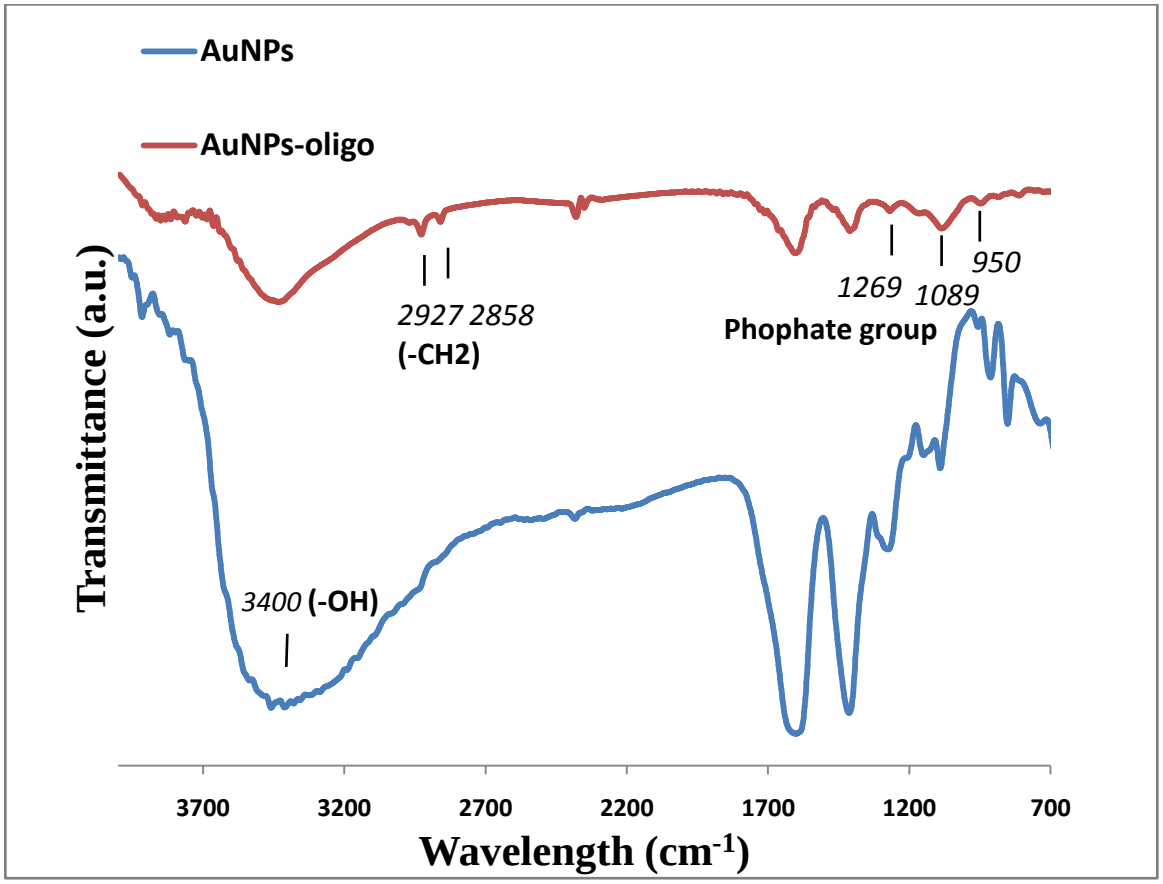

Fig. 3.1.6 FTIR spectra of AuNPs and AuNPs–oligo.

3.1.4 Emission spectrum of GQDs-oligo and absorption spectrum of AuNPs-oligo

The photoluminescence of GQDs relied on the density of sp^2 cluster, which can be tuned by the energy gap of GQDs [38, 159]. GQDs were observed to emit blue luminescence around 460 nm when got excited at 365 nm laser. As the PL of GQDs was a complicated phenomenon, it was influenced by complex mixtures as well, leading to false results or poor precision. This is not suitable for real applications, thus it is crucial

to take potential interferences caused by matrix effects in to account. In this GQDs based FRET biosensor, pH value and H^+ ion strength in the solution were the main matrix effect. Particularly, GQDs possess a pH-dependent PL property. PL intensity decrease dramatically in acidic solution due to the interaction between free zigzag sites of the GQDs and H^+ ions, which impedes the PL emissive state in GQDs [52]. According to Zhu et al., they also observed decreasing PL intensities of GQDs accompanied with blue shift of emission wavelength in alkaline solution [160]. Therefore, neutral pH value ranging from 6 to 8 should be the best working pH value to preserve strong blue fluorescence emission of GQDs. In this experiment, we used neutral buffer solution with pH=7.4 to achieve the strong blue fluorescence emission.

As shown in Fig. 3.1.7 GQDs emit strong blue luminescence at 450 nm, while the emission peak of GQD-ssDNA slightly shifted to the right (460 nm). The adsorption spectra of AuNPs also slightly shifted to the right after conjugation with oligonucleotide with the main adsorption region in the range of 450 nm to 550 nm (Fig. 3.1.8). The spectra overlap between emission spectra of GQDs and absorption spectra of AuNPs ensured the feasibility of this FRET biosensor (Fig. 3.1.9).

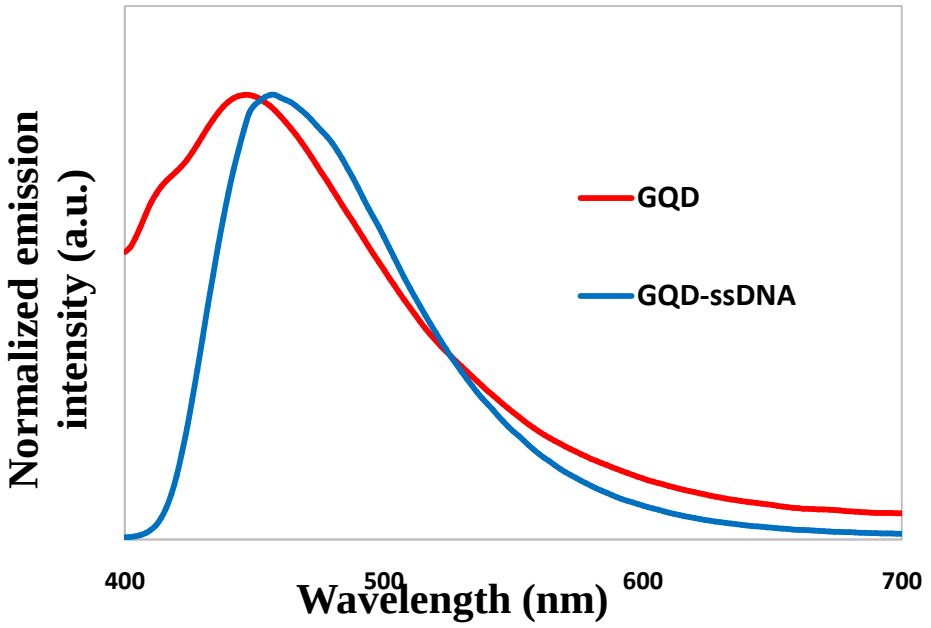

Fig. 3.1.7 Normalized emission spectra of GQDs before and after conjugation with oligos.

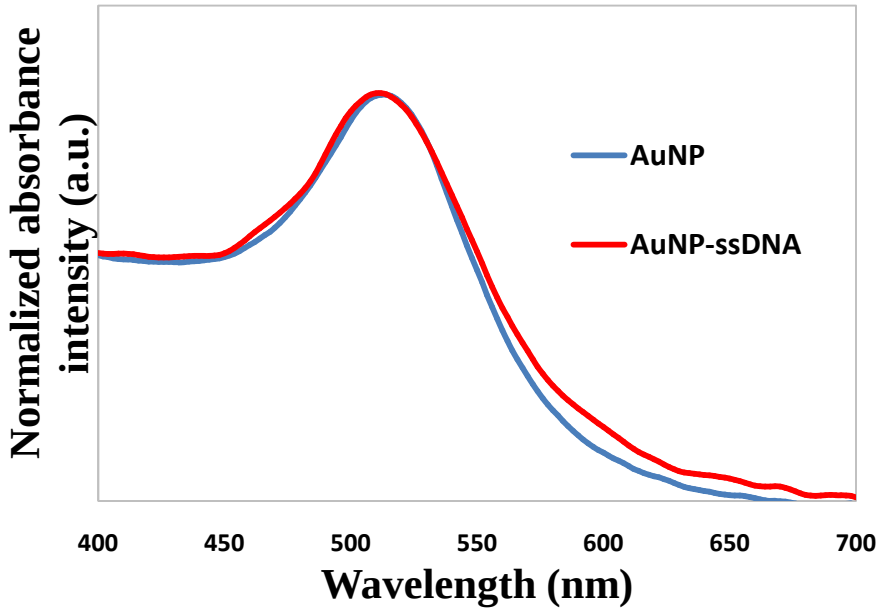

Fig. 3.1.8 Normalized absorption spectra of AuNPs before and after conjugation with oligos.

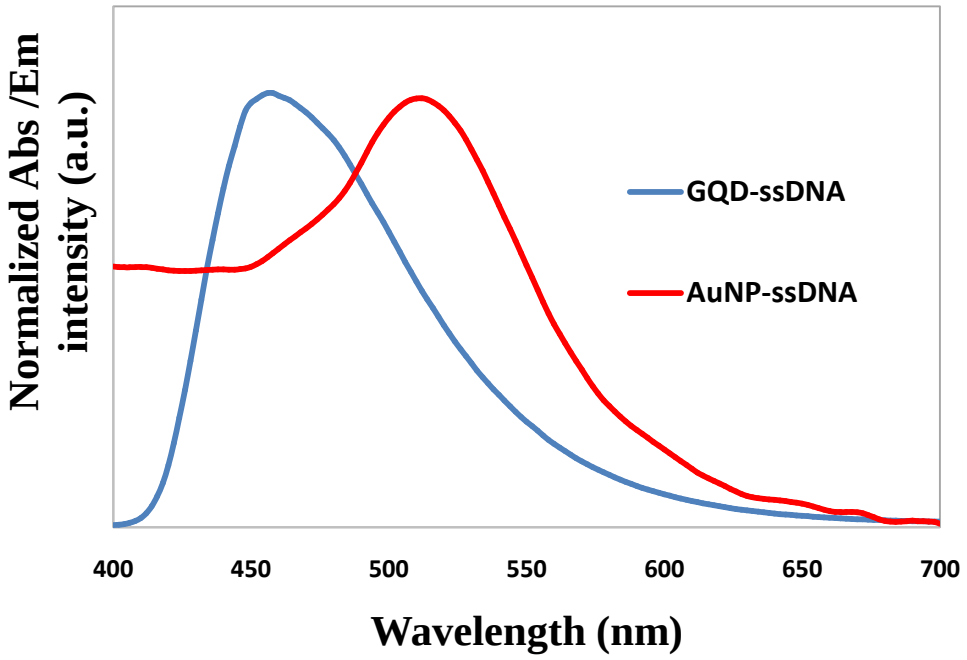

Fig. 3.1.9 Normalized spectral overlap between emission spectra of GQDs and absorption spectra of AuNPs.

3.1.5 Enhanced blue photoluminescence of EDC modified-GQDs

GQDs are dispersed well in water solution due to the abundant oxygen-containing functional groups on the surface, which is demonstrated by the uniform blue color distribution in GQD solution. As shown in Fig. 3.1.10 (left), GQDs exhibit stable blue photoluminescence under UV excitation at 360 nm and exposure time of 1s. In contrast, after mixing with EDC, the modified GQD displayed considerably higher brightness under the same excitation condition and exposure time (Fig. 3.1.10 (right)). The enhanced blue photoluminescence of GQDs was caused by EDC activation, which can graft o-acylisourea active intermediate on the edge of GQDs via interaction with carboxyl groups. Since quantum yield was presented by the ratio of photons emitted and

photons absorbed, the quantum yield of EDC modified-GQD can be calculated by the following equation:

$$\eta = \frac{\varepsilon}{\alpha} = \frac{\int \mathbf{L}(modified - GQD)}{\int \mathbf{E}\,(solvent) - \int \mathbf{E}(modified - GQD)}$$

where η is the quantum yield; ε is the photons emitted by the modified-GQD; $L_{modified-GQD}$shows the luminescence emission spectrum of modified-GQD; $E_{modified-GQD}$ is the spectrum of the light used to excite the modified-GQD, and represents the photons not absorbed by modified-GQD; $E_{solvent}$ is the spectrum of the light used for excitation with only the solvent, and stands for the photons going into the sample. Therefore the difference between the areas of $E_{solvent}$ and $E_{modified-GQD}$ will give the photons absorbed. The area under $L_{(modified-GQD)}$ gives the photons emitted by the modified-GQD. According to Fig. 3.1.11, the quantum yield of EDC modified-GQD was calculated to be 19.01%, which was much higher than that of bare GQDs (QY less than 10%) [161]. This enhanced photoluminescence and quantum yield may be attributed to the chemical nature of modified GQDs, which contained less carboxylic and epoxide groups acting as the non-radiative electron-hole recombination centers, thus the intrinsic state emission was enhanced, and their fluorescent quantum yields could be subsequently increased.

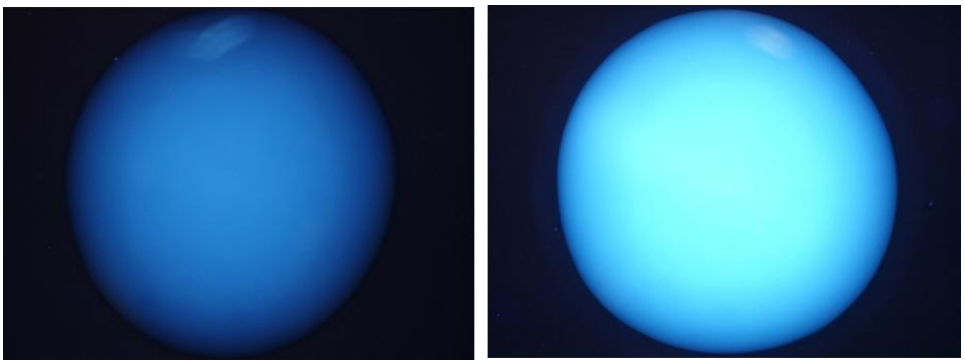

Fig. 3.1.10 Fluorescence image of GQDs (left) and modified-GQDs (right) under excitation of 360 nm and exposure time of 1 s.

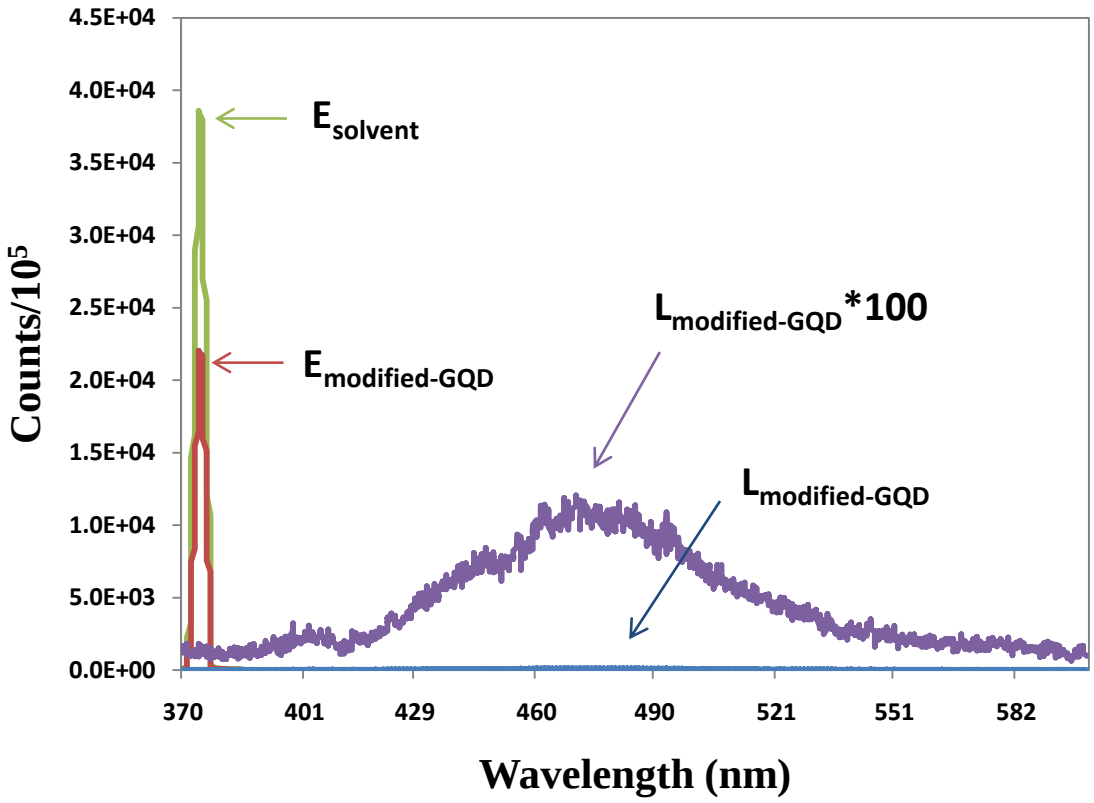

Fig. 3.1.11 The green and red curves are excitation spectrum of solvent ($E_{solvent}$) and modified-GQD ($E_{modified\text{-}GQD}$), respectively; The blue curve is the luminescence emission spectrum of modified-GQD ($L_{modified\text{-}GQD}$); The purple curve is the 100 times magnified version of the luminescence emission spectrum of modified-GQD ($L_{modified\text{-}GQD}$*100).

3.1.6 Construction of FRET biosensor for target probes detection

The quenching efficiency of this FRET biosensor was explored using a series of concentrations of target probes. The concentrations of target DNA increased from 100 pM to 400 nM gradually. A fixed amount of GQDs conjugated with capture probe at 1 mg/mL was used as fluorescence probe. A certain amount of AuNPs conjugated with reporter probe at concentration of 7 nM was acted as fluorescence quencher. As a result of DNA co-hybridization, the formation of sandwich structure of GQDs-oligo-AuNPs

brought GQDs close to AuNPs, leading to fluorescence quenching. The quenching efficiency is expressed by $Q=1-F_q/F_0$, where F_q is the fluorescence intensity of GQDs after quenching, and F_0 is the original fluorescence intensity of GQDs. With the increasing of concentrations of target probes, the quenching efficiency was enhanced gradually. When the target probes was increased to 100 nM, the quenching efficiency reached a maximum of 87% and almost unchanged with further increasing amount of target probes (Fig. 3.1.12). Fig. 3.1.13 shows the fluorescence signal quenching (F_0-F_q) versus a series of target probes concentrations. Then fluorescence signal decreased with the decreasing concentration of target DNA. The limit of detection (LOD) is determined by the control signal plus three times of noise signal (standard derivation), which was around 1 nM. In this work, our GQDs-AuNPs based FRET biosensor was much more sensitive than that of fluorescence microarray (LOD from tens of nM to mM) [110]. The sandwich structure assay also enhanced the specificity and made it more applicable for real situations.

For GQD and AuNP based FRET biosensor based FRET biosensor, the response time is related to the co-hybridization of target DNA with GQD conjugated reporter probe and AuNP modified capture probe and the response time for target bacterial DNA detection was around 2 hours. Moreover, due to the good stability and negligible photobleaching effect of GQD, this FRET biosensor can be stored for several weeks.

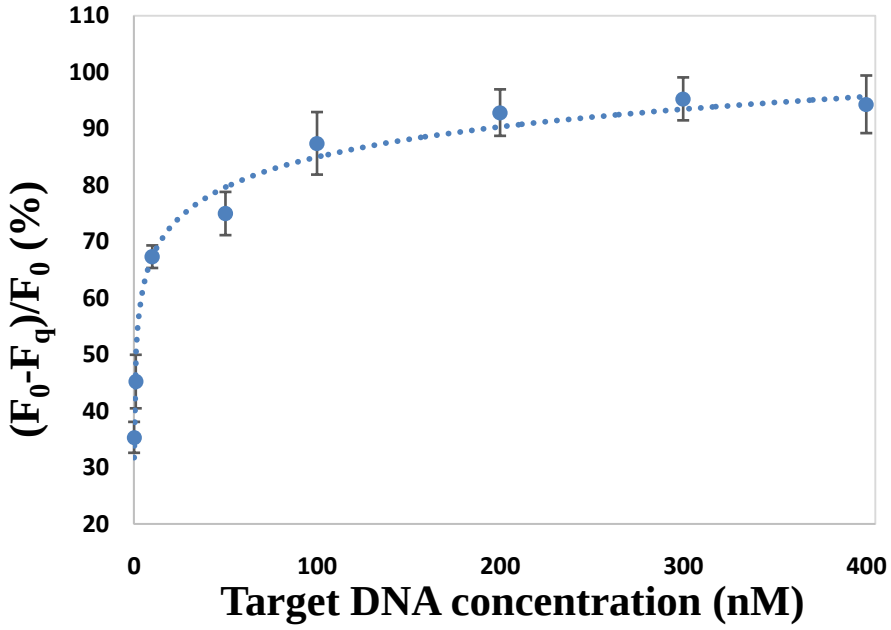

Fig. 3.1.12 The quenching efficiency $Q = 1-F_q/F_0$ versus with a series of target oligo concentrations.

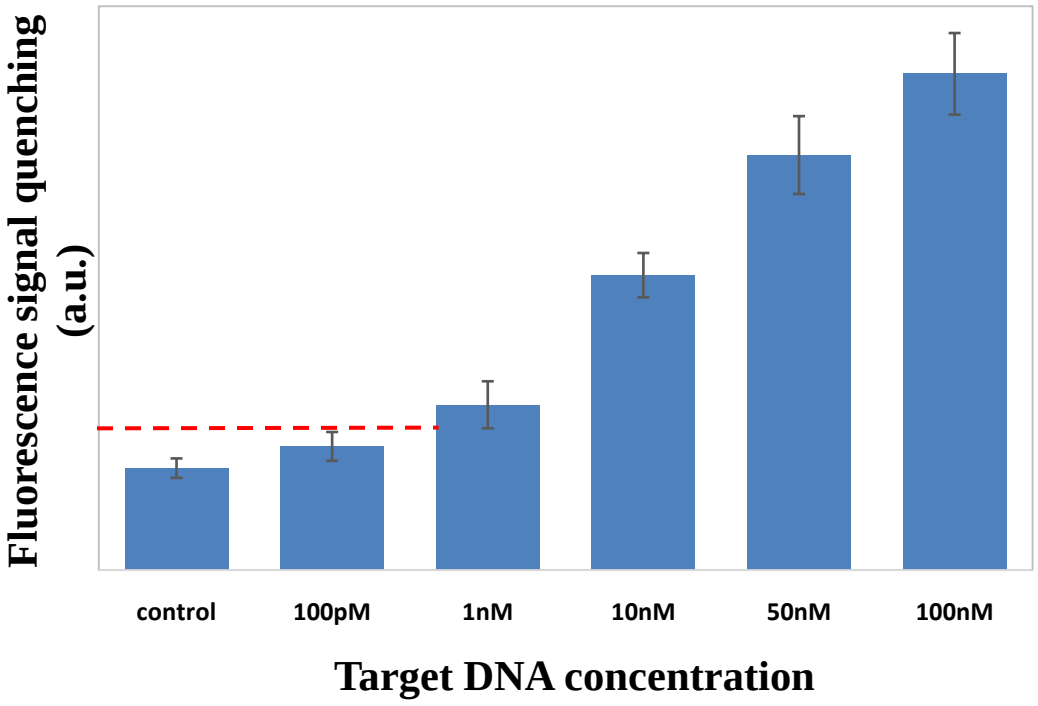

Fig. 3.1.13 The fluorescence signal quenching (F_0- F_q) versus a series of target oligo concentrations from 100 pM to 100 nM.

3.1.7 Specificity of FRET biosensor

The specificity of this GQDs-AuNPs FRET biosensor was explored using both single-base mismatched target DNA and double-base mismatched target DNA as compared to the complementary target DNA. All the experiments used the same concentration of 200 nM for comparison. As shown in Fig. 3.1.14, the quenching efficiency decreased significantly with the increasing number of mismatches. The quenching efficiency for complementary target DNA was around 93%, while that of single-base mismatch DNA and double-base mismatch DNA dropped to 37% and 22% respectively. Generally, an increasing number of mismatches of target probes would lead to decreasing duplex stability, which decreased the chances to form GQDs-probes-AuNPs sandwich complex and GQDs emission would not decrease much. Similar results have also been reported [162-163]. The results indicated that this FRET DNA biosensor exhibits high selectivity.

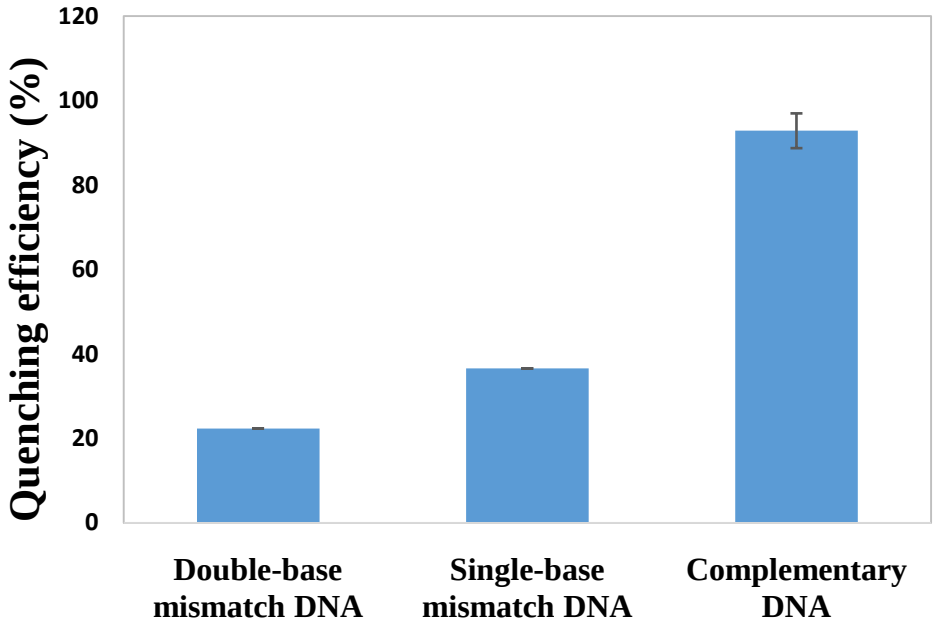

Fig. 3.1.14 Quenching efficiency comparison among single-base mismatched oligos, double-base mismatched oligos, and complimentary target oligo with concentration of 200 nM.

3.2 Graphene oxide based FRET biosensor for bacterial protein toxin detection

3.2.1 Mechanism of GO-peptide FRET biosensor

The sensing principle of GO-peptide based FRET biosensor for detection of enzymatic activity of bacterial protein toxin (BoNT-LcA) is shown in Fig. 2.2.3. The SNAP-25-GFP residues designed from 141 to 206 with specific cleavage site at 197/198 were serving as the FRET donor in this work. GO was regarded as the FRET acceptor due to its super quenching ability. For constructing the GO-peptide based FRET biosensing platform, the C terminus of GO was covalently conjugated with the N terminus of protease substrate peptide (SNAP-25-GFP) via EDC/NHS chemical

activation, which brought GFP and GO into close proximity and resulted in fluorescence quenching effect. The emission of GFP was largely absorbed by GO under excitation of 468 nm due to the ultra-high quenching efficiency of GO. In addition, the unreacted surface area of GO was blocked by bovine serum albumin (BSA) to prevent the non-specific peptide adsorption. The SNAP-25-GFP substrate can be cleaved into two fragments with addition of target BoNT-LcA protease. As a result, the GFP labeled partial fragment was released from GO surface and the fluorescence signal was recovered. By measuring the recovered fluorescence signal, BoNT-LcA enzymatic activity can be monitored.

3.2.2 Characterization of synthesized GO and SNAP-25-GFP

To realize the design, GO sheets were synthesized according to the previous research and the GO dispersion with particle size under 100 nm was obtained in water [157]. XRD spectrum was used to characterize the GO products. As shown in Fig. 3.2.1, the characteristic peak of GO centered at $2\Theta=10.58^{0}$. The GO products was also characterized by Raman spectrum, which displayed the well-grounded strong peak at 1580 cm^{-1} (G band) and a weak peak at 1350 cm^{-1} (D band) (Fig. 3.2.2). The UV-vis absorption spectrum of GO collected by an UV-visible spectrophotometer was displayed in Fig. 3.2.3, which demonstrated that GO had an extremely wide absorption region started from 200 nm and extended to 800 nm.

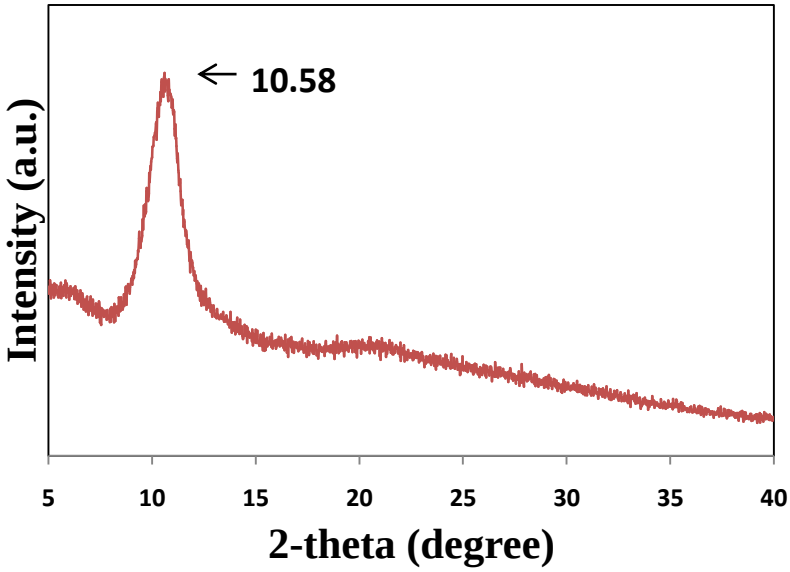

Fig. 3.2.1 XRD spectrum of GO giving typical diffraction peak at 10.58°.

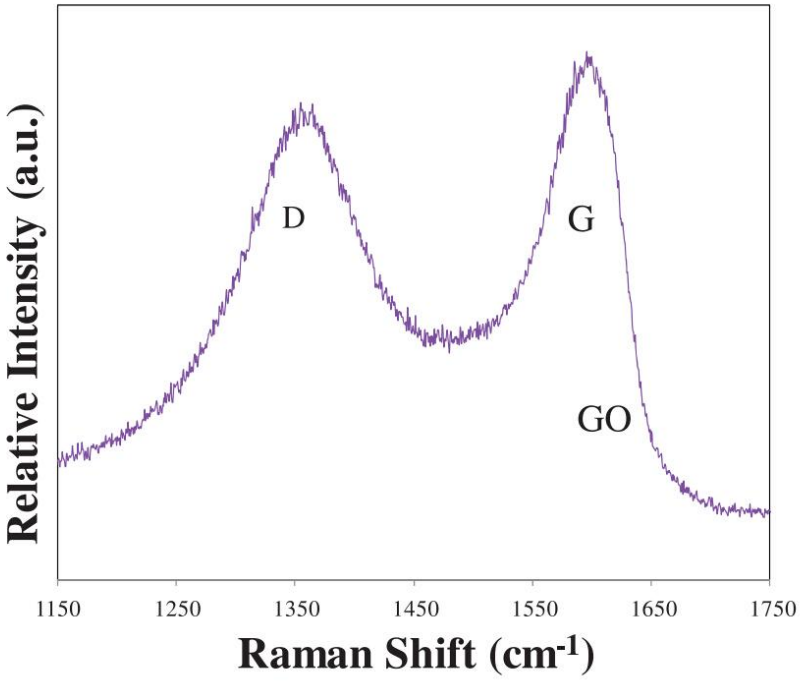

Fig. 3.2.2 Raman spectrum of GO.

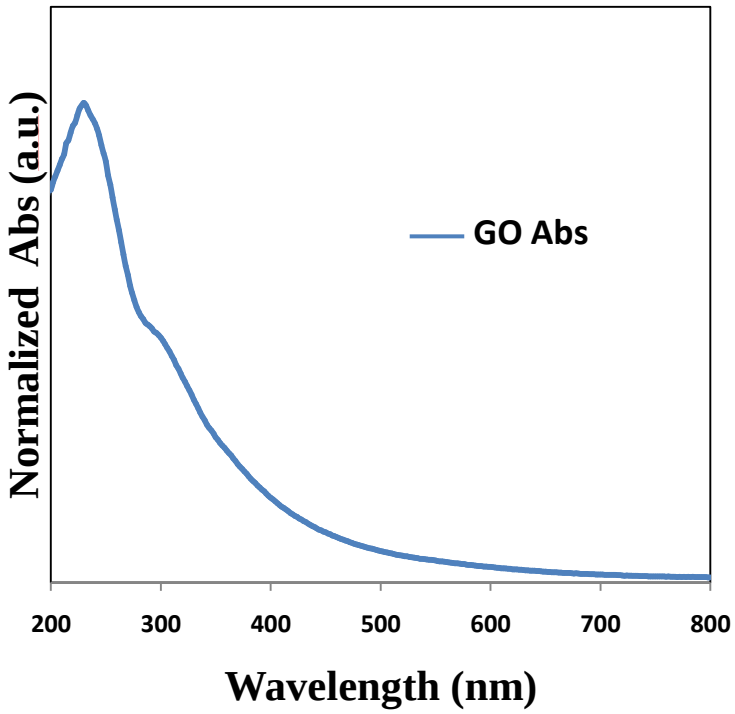

Fig. 3.2.3 Absorption spectrum of GO.

SNAP-25-GFP substrate was synthesized by coupling fusion protein SNAP-25 with GFP. Fig. 3.2.4 shows intense fluorescence image of 1 mg/mL SNAP-25-GFP solution during illumination of 468 nm laser. The fluorescence spectrum of SNAP-25-GFP was recorded using an Edinburgh FLSP920 spectrophotometer equipped with a 450 W steady-state xenon lamp at room temperature. The typical emission spectra of GFP were centered at 510 mm when excited at 468 nm (Fig. 3.2.5).

The broad absorption spectra of GO has spectral overlap with GFP emission band at 510 nm, which meets the necessary condition of FRET effect. Therefore, the energy transfer from GFP to GO was explored by measuring the change of fluorescence intensity after the conjugation process between GO and peptide.

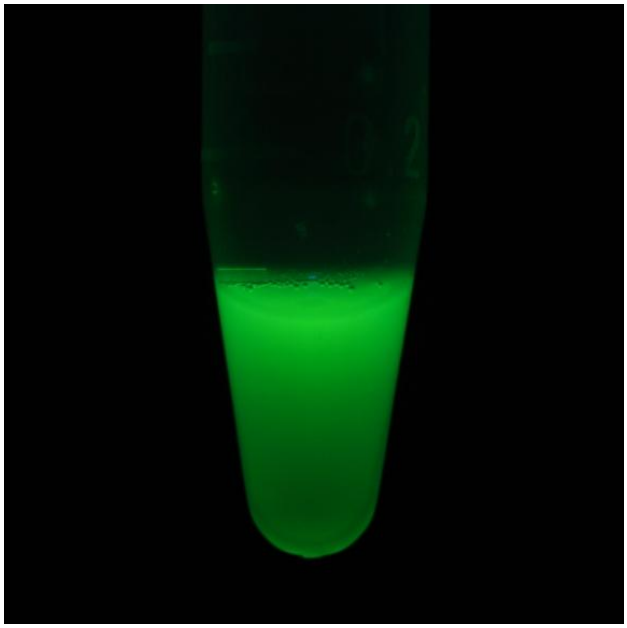

Fig. 3.2.4 Fluorescence image of green fluorescence protein modified SNAP-25.

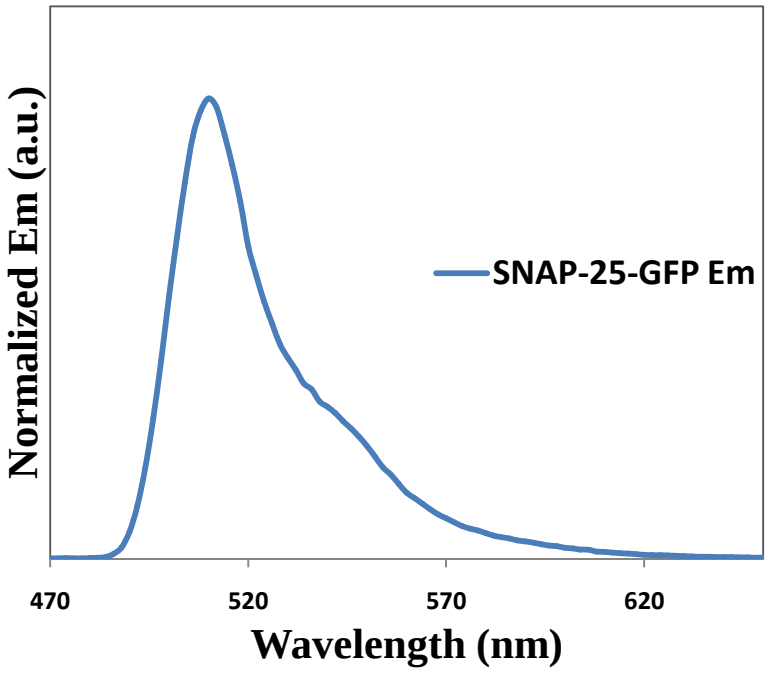

Fig. 3.2.5 Emission spectrum of SNAP-25-GFP.

3.2.3 Conjugation of GO and peptide

SNAP-25-GFP substrates were covalently linked to GO surface via amide bonding, which was formed in the presence of EDC/NHS. FRET effect took place after the formation of GO-SNAP-25-GFP conjugates, which brought GO and GFP into a close distance. The conjugation of GO-peptide complex was verified by AFM measurements. The AFM image and corresponding height profile of bare GO were displayed in Fig. 3.2.6 (a), which showed that the thickness of the synthesized GO sheets was around 1 nm. However, after conjugating GO with SNAP-25-GFP, the heights of the conjugates were approximately around 8 to 10 nm, which indicated that SNAP-25-GFP was successfully conjugated with GO surface (Fig. 3.2.6 b).

a

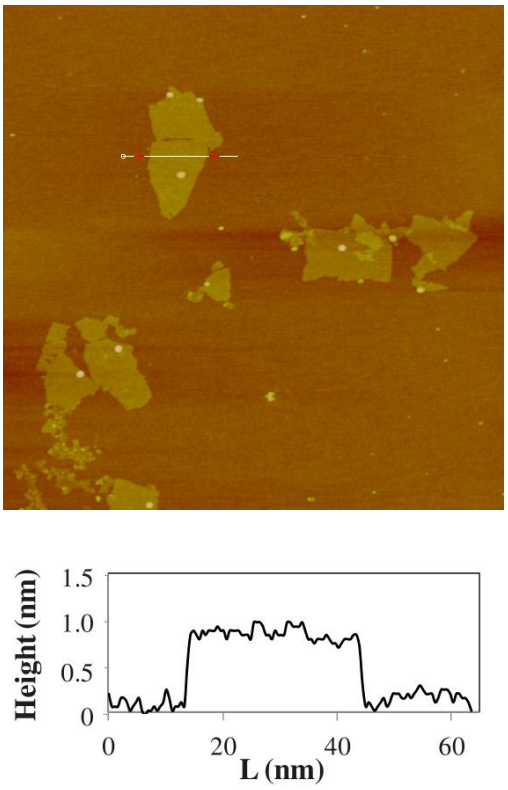

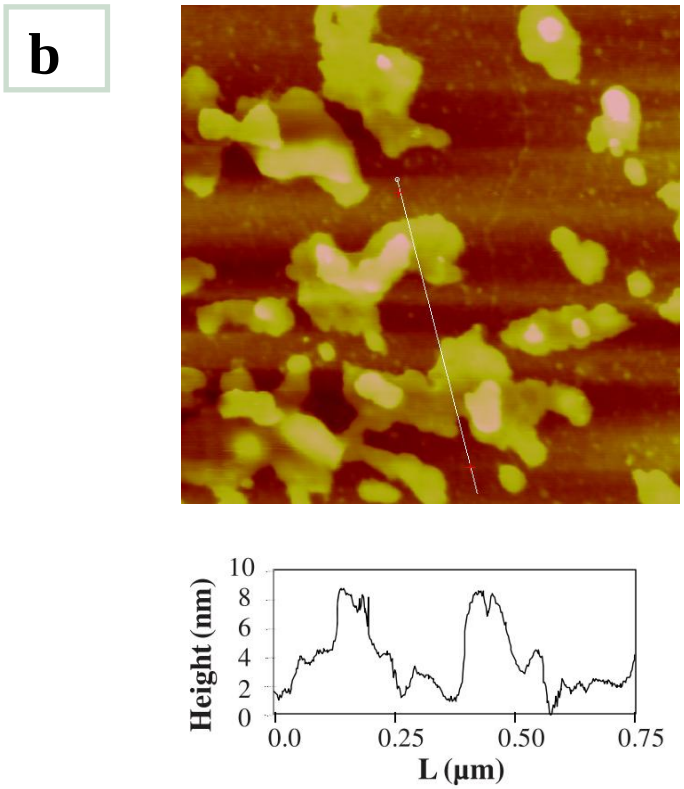

Fig. 3.2.6 AFM images and height profiles of (a) GO and (b) GO-SNAP-25-GFP complex.

The chemical structures of GO and GO-peptide conjugates were characterized by means of FTIR spectra. As shown in Fig. 3.2.7, GO has various characteristic absorptions. A broad peak at 3401 cm^{-1} indicates the stretching of –OH group. The most feature characteristic absorption bands at 1735 cm^{-1}, 1628cm^{-1}, 1384 cm^{-1}, 1095 cm^{-1} represent the stretching vibration of C=O, C=C, C-OH and C-O, respectively, revealing the presence of -COOH, -OH and O-C-O functional groups in GO. For the GO-peptide complex, conjugation of SNAP-25-GFP peptide onto GO surface was confirmed by the appearance of characteristic absorption peaks corresponding to the $-CH_2-$ stretching vibration (2935 cm^{-1} and 2877 cm^{-1}), and amide group vibration (1647 cm^{-1} and 1553 cm^{-1}). They both confirmed the successful conjugation of SNAP25-GFP onto GO.

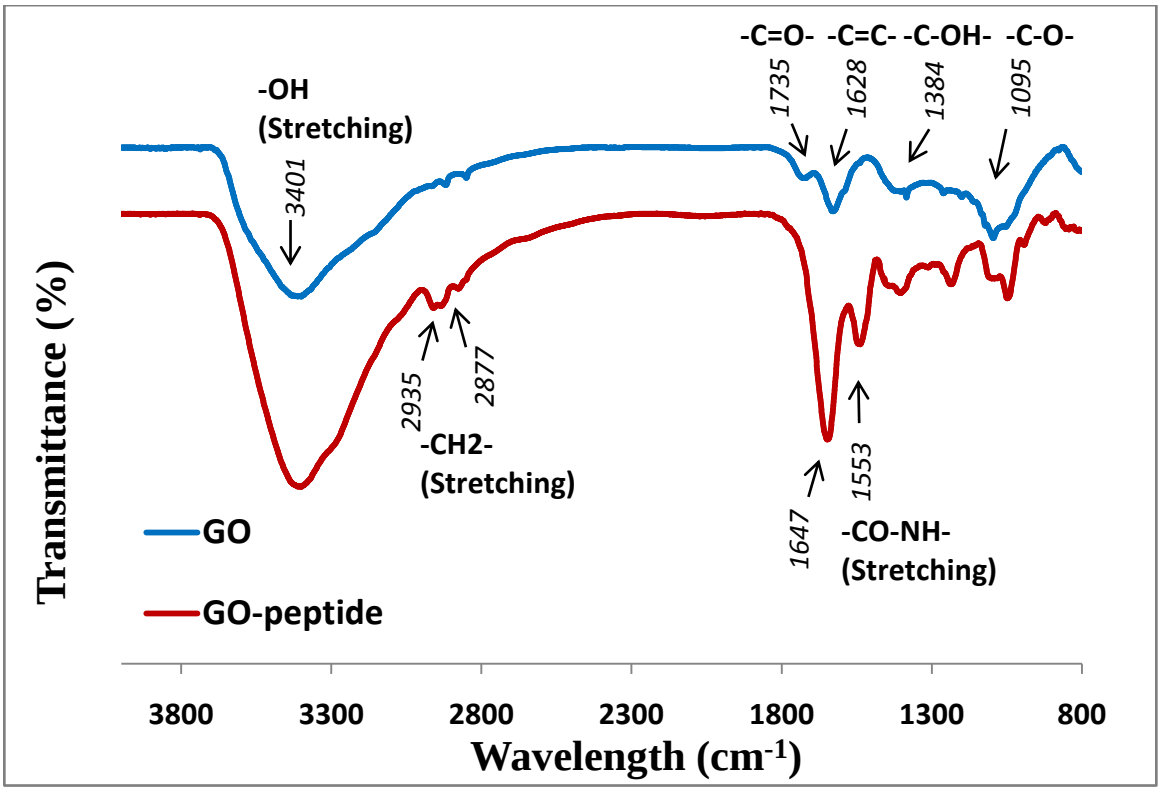

Fig. 3.2.7 FT-IR spectra of GO and GO-peptide conjugate.

Zeta potential measurements showed that GO-peptide conjugates were less negative charged as compared to bare GO solution (Fig. 3.2.8). The average zeta potential for bare GO was -40.7 mV at pH=7 due to plenty of negative charged oxygen functional groups on GO surface, such as hydroxyl (-OH), carboxyl (-COOH), epoxy (C-O-C), and carboxylate (COO-), which were similar to the previous reports [164]. The average zeta potential shifted to -16.68 mV at pH=7 for GO-peptide complex after conjugating with SNAP-25-GFP. The increase of zeta potential was caused by the immobilization of less negative charged SNAP-25-GFP peptide onto GO surface.

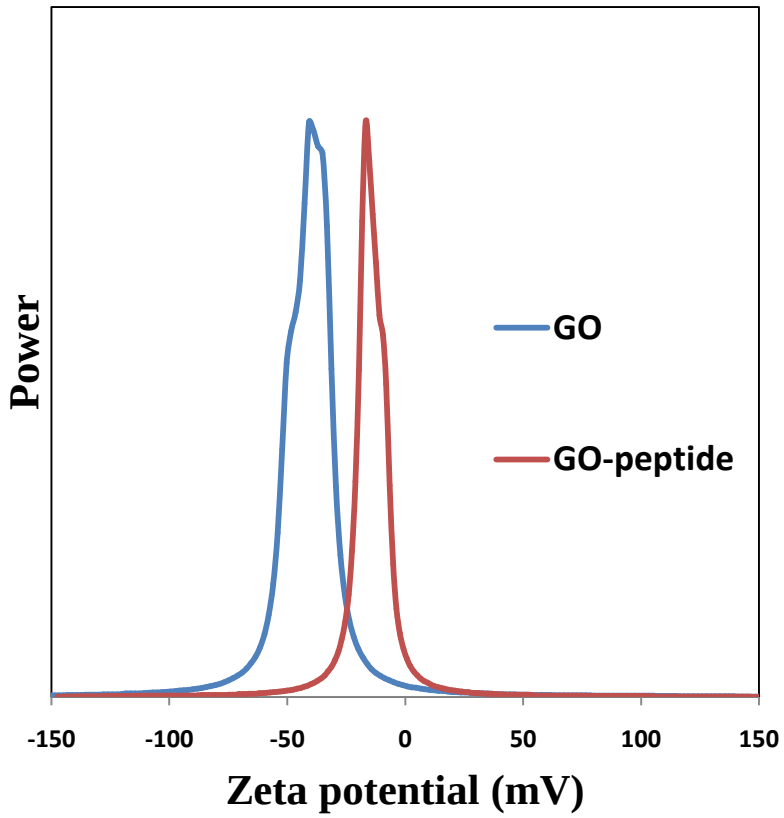

Fig. 3.2.8 Zeta potential of GO and GO-SNAP-25-GFP.

3.2.4 Passivation effect

To demonstrate the passivation effect of BSA on GO surface, adsorption experiments of SNAP-25-GFP peptide (0.12 μg/mL) onto GO surface (60 μg/mL) with EDC/NHS treatment before and after BSA passivation were explored. Meanwhile, adsorption between passivated GO surface and SNAP-25-GFP peptide without EDC/NHS was also investigated. As shown in Fig. 3.2.9, GO without passivation caused a significant fluorescence intensity reduction due to the covalent binding of SNAP-25-GFP onto GO surface (purple curve). This covalent linkage brought SNAP-25-GFP and GO into close proximity, triggering FRET quenching effect with a high quenching ratio

of 92.6% at 510 nm. In contrast, negligible quenching effect was observed for passivated GO with or without EDC/NHS modification at a low quenching ratio of 3.2% and 4.8% respectively (red and green curves).This phenomenon indicated that peptide can neither chemically bind nor physically adsorb onto BSA passivated GO surface. When comparing the red and purple curves, the results demonstrated that the successful covalent linkage between GO and peptide is the driving force for fluorescence quenching effect, and BSA passivation should be executed after EDC/NHS chemical interaction. As a result, passivation on GO surface could significantly decrease non-specific peptide adsorption on GO. Using EDC/NHS chemical method followed with BSA passivation, most SNAP-25-GFP peptides were attached to GO surface by covalent bonds rather than non-specific adsorption.

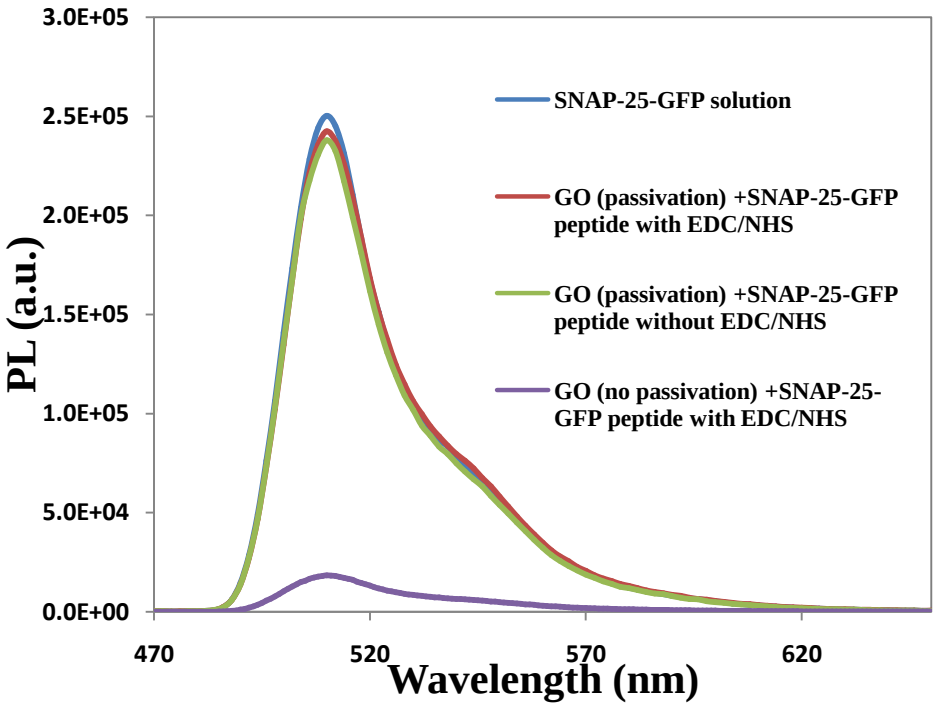

Fig. 3.2.9 Fluorescence spectra of GO and peptide (SNAP-25-GFP) conjugation after and before BSA passivation.

3.2.5 Stability of peptide-conjugated GO complex

To compare the stability of peptide-conjugated GO complex and non-covalent peptide-adsorbed GO composite in complex matrix such as protein abundant solution, the fluorescence signal change was measured for both SNAP-25-GFP peptide adsorbed GO composite and SNAP-25-GFP peptide conjugated GO complex in BSA solution with the same concentration of 0.1 mg/mL. As shown in Fig. 3.2.10, substantial enhancement of fluorescence signal was observed for peptide-adsorbed GO composite in BSA solution, which suggested the displacement of SNAP-25-GFP peptide from GO surface by BSA. In contrast, covalent conjugated GO-peptide complex only showed very slightly increased fluorescence signals, indicating the stability of covalent conjugated GO-peptide complex. The stable covalent bonding between GO and peptide plays a significant role in maintaining fluorescence quenching effect by keeping the FRET distance within 30 nm. This experiment demonstrated the weak affinity of peptide adsorbed on GO in the protein abundant solution. The results also showed that peptide-adsorbed GO complex based FRET biosensor had low specificity in protein abundant solution, whose fluorescence signal recovery could be from non-specific protein replacement. Therefore, peptide-conjugated GO complex plus passivation is a better FRET-based peptide assay platform compared with peptide-adsorbed GO composite.

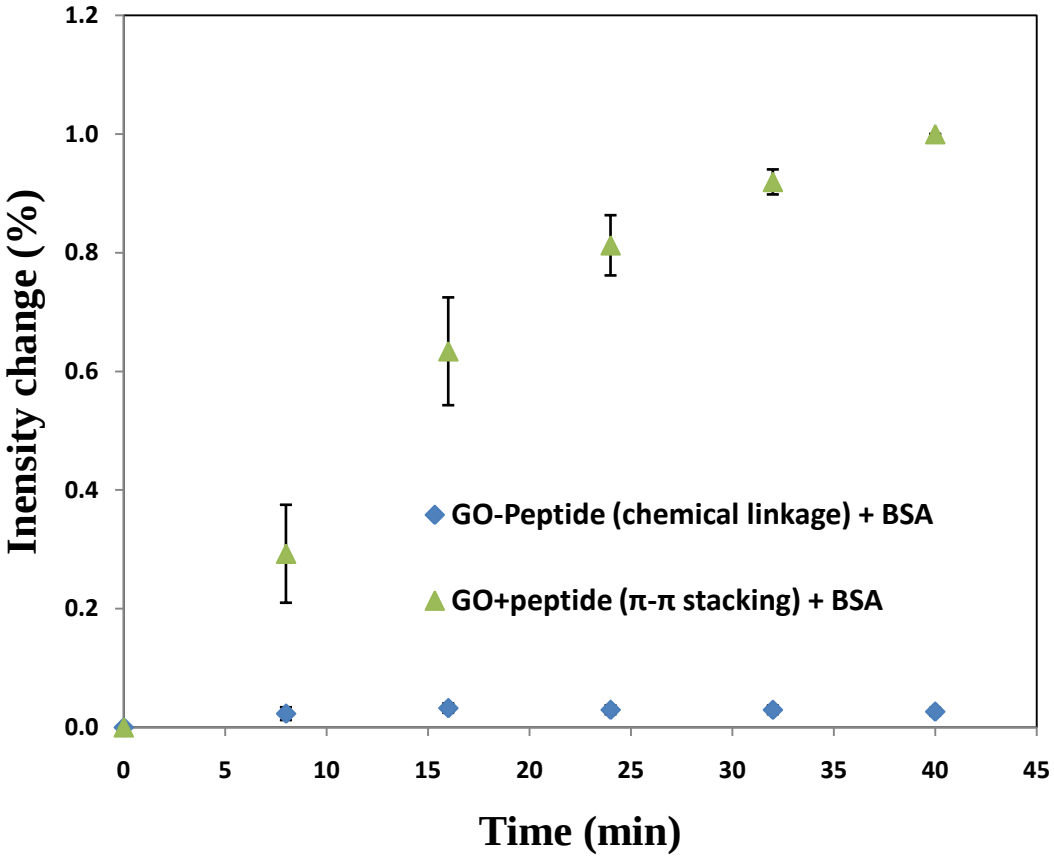

Fig. 3.2.10 Fluorescence signal change for peptide adsorbed GO composite and peptide conjugated GO complex in BSA solution with the same concentration of 0.1 mg/mL.

3.2.6 Construction of GO-peptide FRET biosensor

SNAP-25-GFP substrate can emit intense green light centered at 510 nm when using 468 nm blue light illumination. Base on the measurement of fluorescence quenching intensity, the energy transfer from GFP to GO was explored quantitatively. Herein, SNAP-25-GFP with fixed volume and concentration (20 µL, 0.12 µg/mL) was used as the FRET donor. 40 µL GO solution with increasing concentrations (from 0 µg/mL to 120 µg/mL) was acted as the FRET quencher. After incubating SNAP-25-GFP peptide substrate with GO solution, the fluorescence signals were then measured. The

same volume of DI water was added to the SNAP-25-GFP solution and the related fluorescence signals were measured as control. Fig. 3.2.11 shows the fluorescence spectra of GO-SNAP-25-GFPconjugates with increasing concentrations of GO. Particularly, the fluorescence signal decreased gradually with increasing concentrations of GO from 0 µg/mL to 120 µg/mL. This fluorescence quenching was realized as a result of conjugation between GO and SNAP-25-GFP, which shortened the distance between donor-acceptor pair. The quenching efficiency is expressed by $Q=1-Fq/F0$, where F_q is the fluorescence intensity of SNAP-25-GFP after quenching, and F_0 is the original fluorescence intensity of SNAP-25-GFP. As shown in Fig. 3.2.12, the fluorescence quenching efficiency reached a maximum of 98% and the normalized fluorescence intensity (F_q/F_0) reached 1.6% when GO concentration increased to 60 µg/mL. The quenching efficiency kept almost unchanged when GO concentration further increased. This high quenching efficiency of 98% was due to the excellent quenching capability of GO.

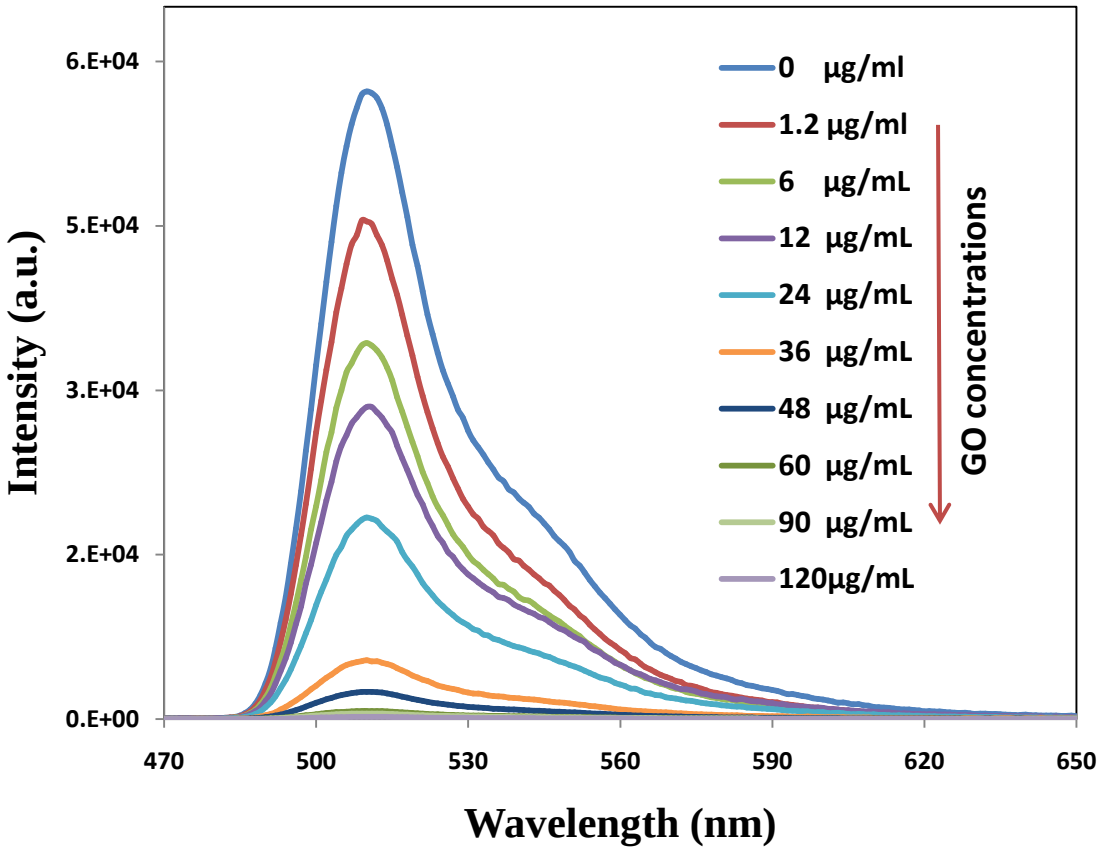

Fig. 3.2.11 Fluorescence emission spectra of GO-SNAP-25-GFP complex in the presence of increasing concentrations of GO.

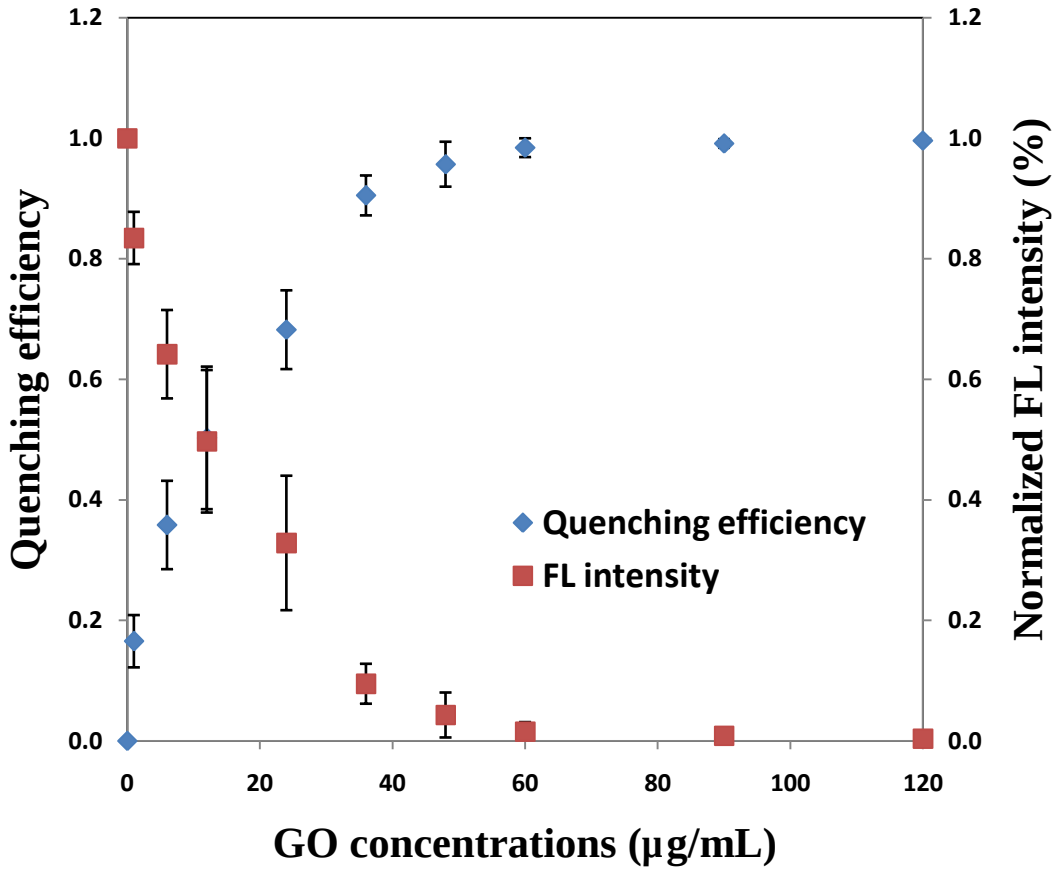

Fig. 3.2.12 Quenching efficiency and normalized fluorescence intensity with increasing concentrations of GO.

3.2.7 Fluorescence signal recovery for LcA protease activity detection

After investigating the quenching efficiency of GO on SNAP-25-GFP, we explored the use of GO-SNAP-25-GFP complex as the sensing platform for BoNT-LcA protease activity detection. GO at a concentration of 60 µg/mL together with 0.12 µg/mL SNAP-25-GFP were hired to prepare the GO-SNAP-25-GFP complex for BoNT-LcA protease activity detection in accordance to the criteria of efficient FRET. 60 µg/mL GO was regards as the optimal ratio for maximum quenching efficiency of 98% against fluorescence peptide substrate, and the background signal is significantly

reduced by GO. After exposing the GO-peptide FRET platform to a series of concentrations of BoNT-LcA for 30 minutes, fluorescence emission spectra were measured to quantify the fluorescence recovery signals. Fig. 3.2.13 shows the fluorescence emission spectra of GO-SNAP-25-GFP complex with addition of increasing concentrations of BoNT-LcA from 1 fg/mL to 10 pg/mL. On mixing GO-SNAP-25-GFP complex with increasing concentrations of BoNT-LcA, the fluorescence signal was gradually recovered, as a result of the increasing cleavage action of BoNT-LcA to release the cleaved fragment with GFP from GO surface to the solution. Fig. 3.2.14shows the relative fluorescence signal recovery rate $(F_r\text{-}F_q)\ /F_q$, where F_r is the recovered fluorescence intensity of SNAP-25-GFP after addition of BoNT-LcA, and F_q is the fluorescence intensity of SNAP-25-GFP after quenching. As shown in Fig. 3.2.11, this FRET biosensor shows a quantifiable detection ranging from 1 fg/mL to 10 pg/mL and a linear detection ranging from 1 fg/mL to 1 pg/mL (inset of Fig. 3.2.14). The limit of detection (LOD) for BoNT-LcA protease activity detection was around 1 fg/mL based on the background signal plus 3 times of standard derivation. These results were superior to the current detection methods including mouse bioassay [116], immunoassays [117, 119], organic fluorophore based FRET biosensors and the commercial available FRET kits [130-133, 165], whose BoNT LODs are in the range from 1 pg/mL to 1 ng/mL.

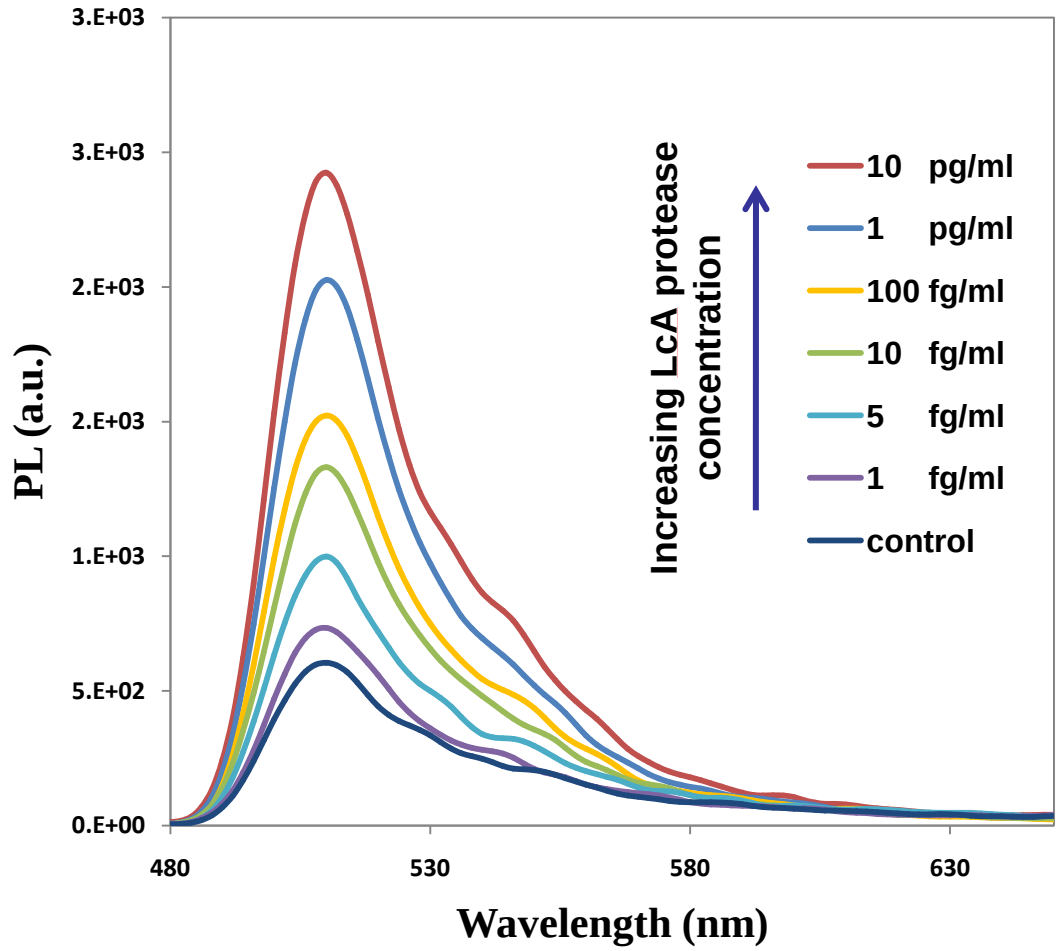

Fig. 3.2.13 Fluorescence emission spectra of GO-SNAP-25-GFP complex with addition of BoNT-LcA with various concentrations from 1 fg/mL to 10 pg/mL.

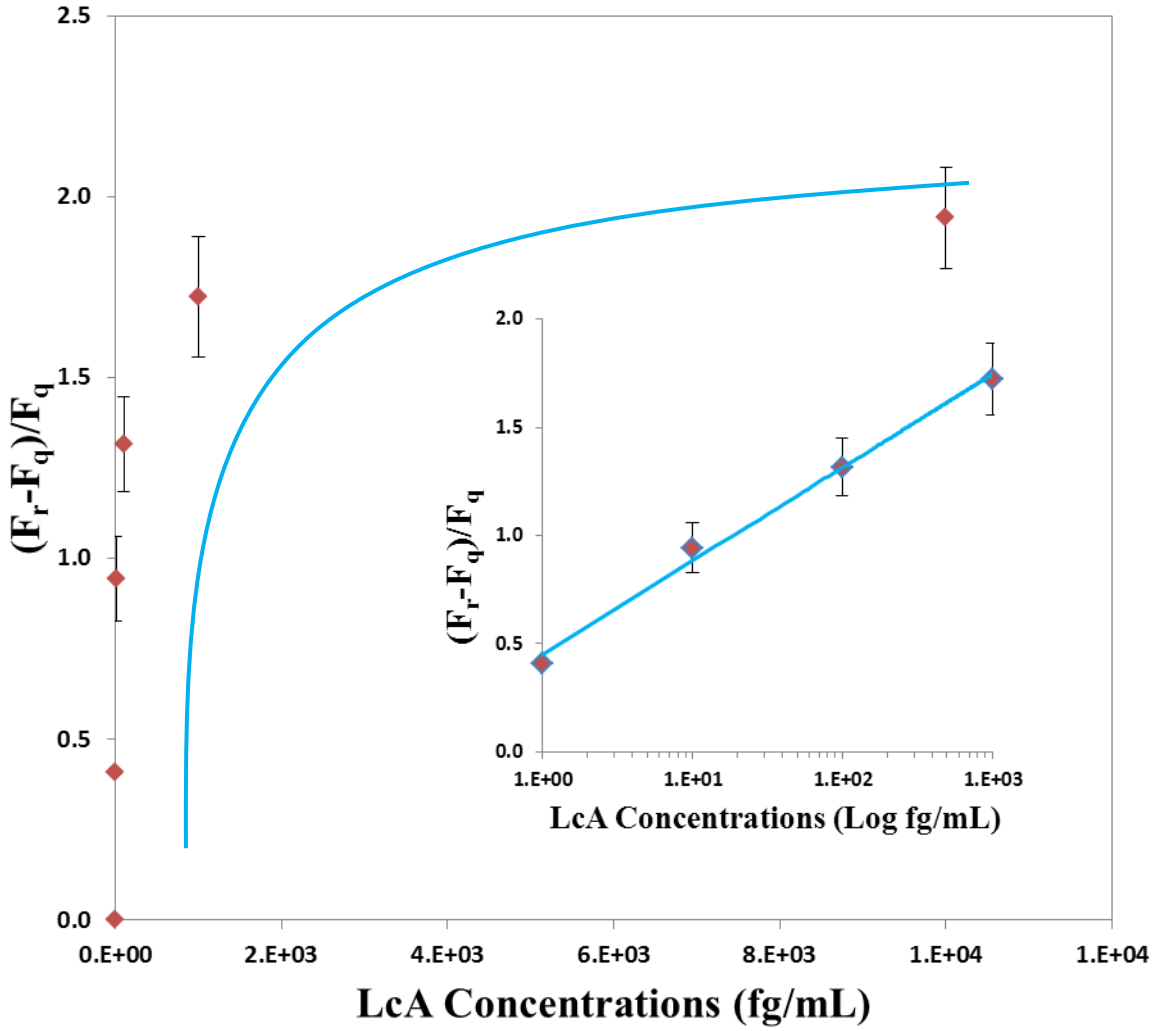

Fig. 3.2.14 Relative fluorescence intensity recovery $(F_r\text{-}F_q)/F_q$ for various LcA concentrations from 1 fg/mL to 10 pg/mL. Inset: linear detection range from 1 fg/mL to 1 pg/mL.

3.2.8 Time response curve for fluorescence signal recovery

Time dependent SNAP-25-GFP release effect was explored by measuring the fluorescence intensity recovery at various time points after addition of BoNT-LcA. The fluorescence recovery signals were monitored by a Tecan Infinite F200 micro-plate reader at room temperature. The fluorescence intensity time plot upon

addition of BoNT-LcA to GO-SNAP-25-GFP complex solution shows the response time of this biosensor is around 30 minutes (Fig. 3.2.15), highlighting the great potential in developing a simple and sensitive diagnostic assay for BoNT enzymatic activity detection in real time.

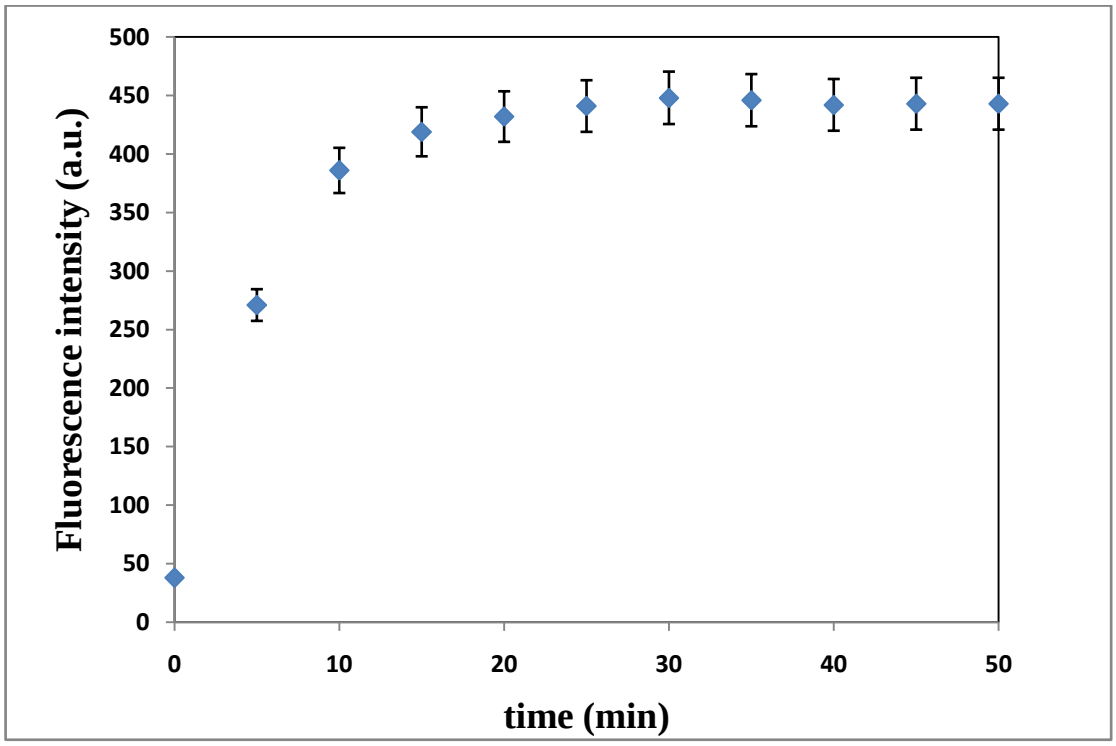

Fig. 3.2.15 Fluorescence signal recovery change with time after addition of BoNT-LcA.

3.2.9 Performance evaluation of FRET biosensor

BoNT serotype B light chain (BoNT-LcB) was employed as control groups to explore the specificity of this FRET biosensor for BoNT-LcA toxin detection. BoNT-LcB is another kind of botulinum toxins which cannot cleave SNAP-25 substrate. But BoNT-LcB is able to specifically identify neuronal vesicle-associated membrane protein (VAMP) [166]. Experiments based on BoNT-LcB were conducted via procedures that were identical with BoNT-LcA detection. With the same concentration of target (0.7

mg/mL), BoNT-LcB did not cause an obvious recovery of donor fluorescence signals, while BoNT-LcA could lead to a large increase of fluorescence signals. It demonstrated that this FRET biosensor was specific for BoNT-LcA and insensitive to BoNT-LcB (Fig. 3.2.16).

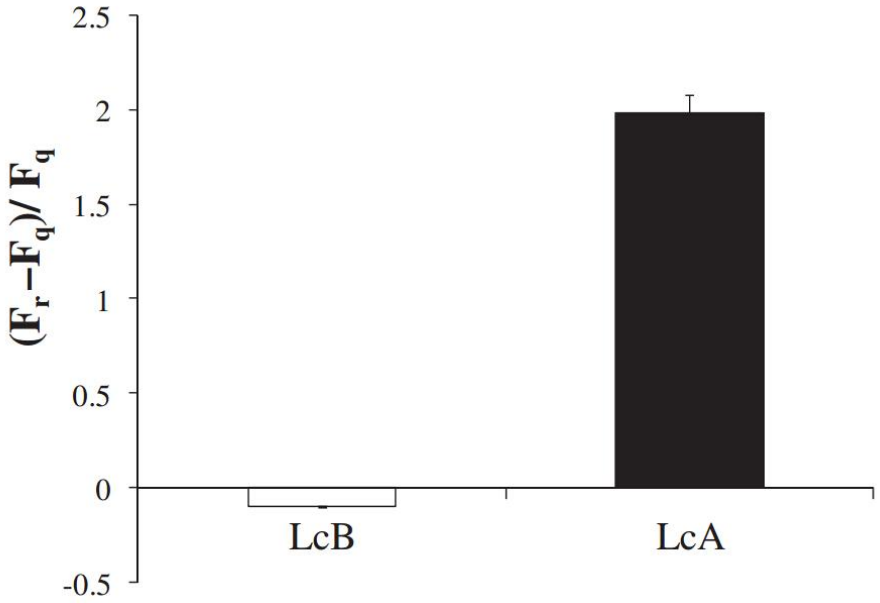

Fig. 3.2.16 Comparison of fluorescence signal recovery between target BoNT-LcA and non-target BoNT-LcB.

The repeatability of the proposed GO-peptide FRET biosensor was investigated by evaluating the variation of experimental results for 10 proposed GO-peptide FRET biosensor. The standard deviation was 7.9% at 0.1 pg/mL LcA concentration in tris buffer solution. The results indicated that the proposed GO-peptide FRET biosensor was robust for LcA detection with acceptable repeatability. However, this GO-peptide based FRET biosensor can be stored for only a few days due to the instability of fluorescence peptide, which is biodegradable.

To evaluate the ability of this FRET biosensor for practical applications, LcA protease activity detection was explored in skimmed milk and apple juice. The GO-peptide based FRET platform was applied in skimmed milk and apple juice with 0.1 pg/mL spiked BoNT-LcA toxins, respectively. Fluorescence recovery signal measured in tris buffer solution was used as the reference for comparison. All the experiments were conducted in the same condition according to previous work. As shown in Fig. 3.2.17, there was no observable fluorescence recovery rate difference between toxin-spiked buffer and toxin-spiked apple juice, indicating apple juice has no significant effect on performance of this FRET biosensor for LcA toxin detection. In toxin-spiked skimmed milk, the fluorescence recovery rate was decreased to around 52% of that in buffer, but still obviously larger than that of non-spiked sample. The decrease of fluorescence recovery signal could be explained by the interference from abundant amount of protein in skimmed milk. The above results demonstrated the potential applicability of this FRET biosensor for real food sample detection.

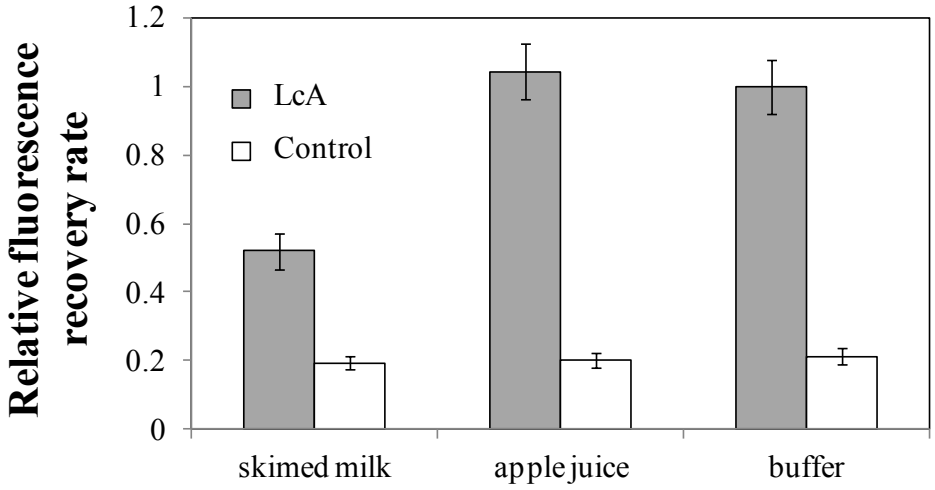

Fig. 3.2.17 Relative fluorescence recovery rate in skimmed milk, apple juice and buffer with and without spiked LcA.

3.3 Graphene oxide based FRET biosensor for MCF-7 cancer cells detection

3.3.1 Mechanism of FRET biosensor

In this FAM-EpCAM aptamer/GO nanocomplex based FRET sensing platform, FAM was selected as a FRET donor with emission of 520 nm when excited at 465 nm (Fig. 3.3.1), and GO was used as a universal fluorescence nano-quencher with super quenching efficiency. The broad absorption spectrum of GO (Fig. 3.3.2) ranging from 200 to 800 nm has a spectral overlap with FAM emission band at 520 nm, which meets the necessary condition of FRET effect.

The sensing principle of FAM-EpCAM aptamer/GO nanocomplex based FRET sensing platform was similar to that of GO-peptide based FRET biosensor (Section 3.2.1). They all had the 'signal on' sensing mechanism. As shown in Fig. 2.3.1, the FAM labeled EpCAM aptamer can physically absorbed on GO surface via π-π stacking, which brought FAM and GO into close proximity and triggered FRET. In the presence of MCF-7 cancer cells, the FAM labeled EpCAM aptamer can specifically bind to EpCAM protein overexpressed on the surface of MCF-7 cells and then detach from GO surface, leading to the recovery of fluorescence signal. By measuring the change of fluorescence signal, MCF-7 cancer cells can be monitored.

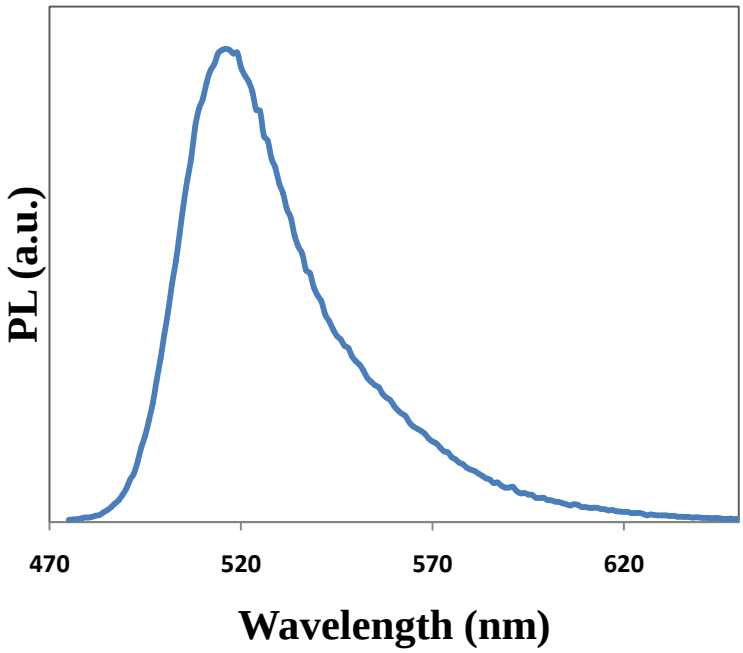

Fig. 3.3.1 Emission spectrum of FAM-EpCAM aptamer.

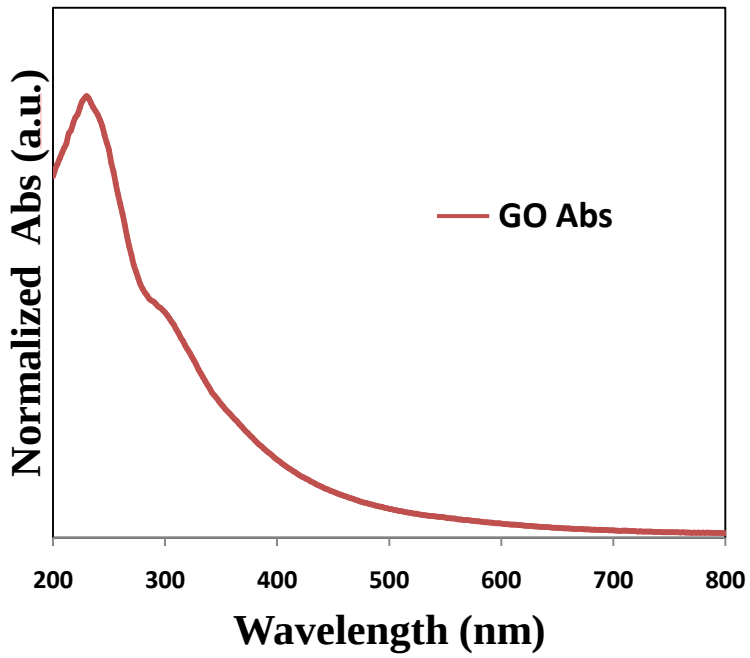

Fig. 3.3.2 Absorption spectrum of GO.

3.3.2 Construction of FAM-EpCAM aptamer/GO nanocomplex based FRET biosensor

The quenching effect was investigated in the nanocomplex of FAM-EpCAM aptamer/GO. Herein, FAM-EpCAM aptamer at fixed volume and concentration (50 µL, 1 µM) was mixed with 50 µL GO solution at a series of increasing concentrations, respectively. After incubating for 30 min, the fluorescence signals of FAM-aptamer were measured. 50 µL PBS buffer was added to the FAM-EpCAM aptamer solution and the related fluorescence signals were measured as control. Fig. 3.3.3 shows the relative fluorescence unit of FAM-aptamer with increasing GO concentrations. Generally, the fluorescence signals of FAM-aptamer decreased gradually with increasing concentrations of GO from 0 to 200 µg/mL. The reason for this phenomenon was because the π-π stacking interaction between GO and FAM-aptamer shortened the interval distance, resulting in the fluorescence quenching of FAM-aptamer by GO, signifying the 'off' state of the FRET system. The quenching efficiency is expressed by $Q=1-F_q/F_0$, where F_q is the fluorescence intensity of FAM-EpCAM aptamer after quenching, and F_0 is the original fluorescence intensity of FAM-EpCAM aptamer. As shown in Fig. 3.3.4, the fluorescence quenching efficiency reaches a maximum platform of 96% when the concentration of GO increases to 100 µg/mL and remains almost unchanged with further GO concentrations. This excellent quenching efficiency close to 100% was resulted from the super quenching capability of GO. Fig. 3.3.5 shows the fluorescence images of FAM-aptamer (1 µM) in the absence (Image 1) of and with the presence (Image 2) of GO solution (100 µg/mL). The fluorescence images turned from bright green (FI: 90.468 RFU, Image 1) to dark (FI: 5 RFU, Image 2), indicating the effective quenching phenomenon caused by GO. However, it was

worth noticing that the photobleaching effect of FAM was not negligible. As shown in Fig. 3.3.4, 1.03% fluorescence intensity of FAM was bleached after 30 min incubation in the dark environment in the absence of GO solution. This phenomenon indicated that FAM as an organic fluorescence dye suffered from the unsatisfied photostability.

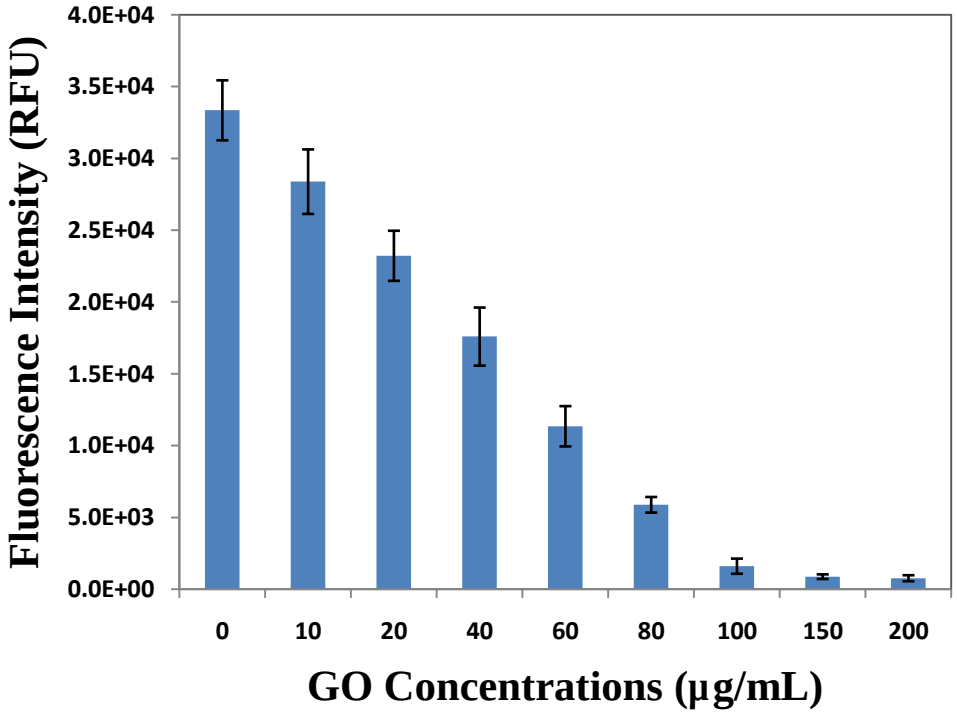

Fig. 3.3.3 Relative fluorescence unit of FAM-aptamer with increasing concentrations of GO.

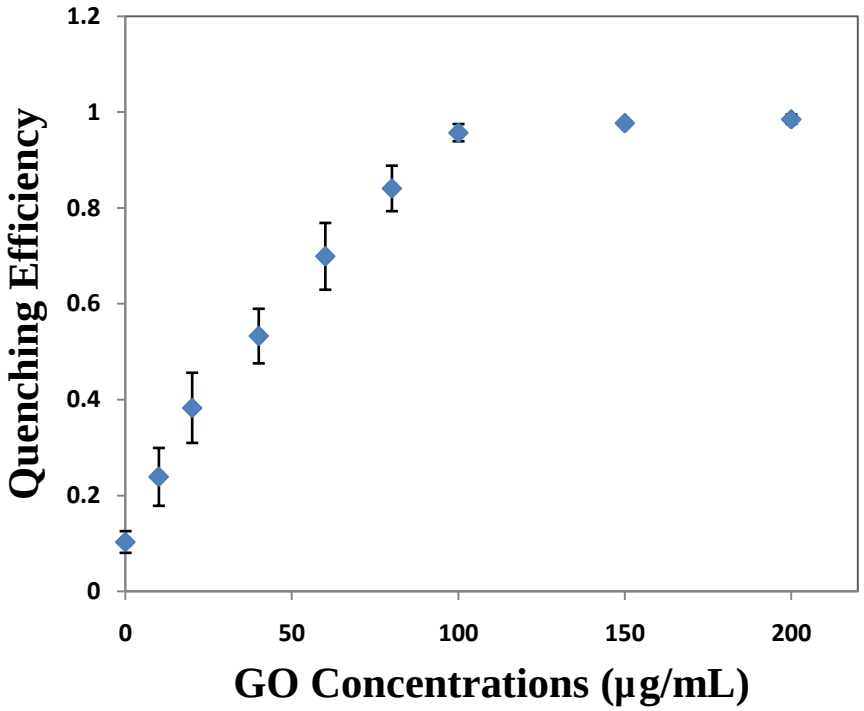

Fig. 3.3.4 Fluorescence quenching efficiency of FAM-aptamer/GO nanocomplex with increasing amount of GO.

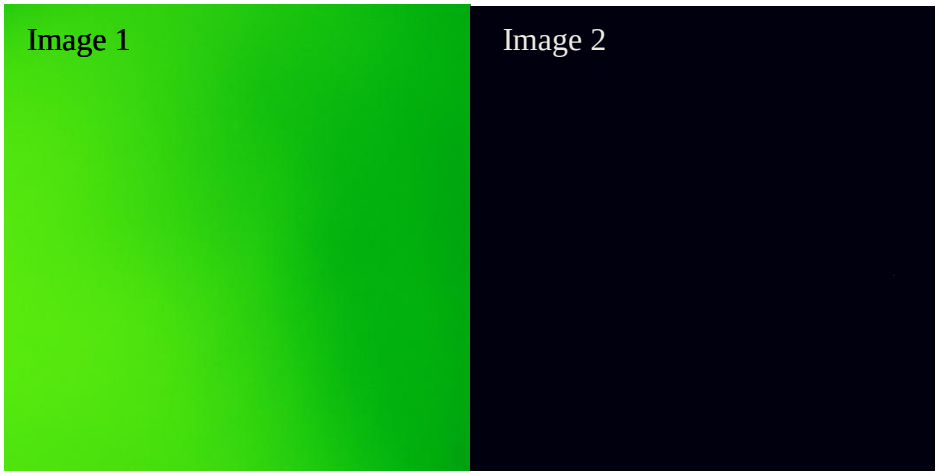

	Area	Mean FI	Min FI	Max FI
Image 1	4016016	90.468	62	119
Image 2	4016016	5	4	19

Fig. 3.3.5 Fluorescence image of FAM-aptamer at concentration of 1 µM (Image 1) and FAM-aptamer absorbed GO (100 µg/mL) nanocomplex (Image 2).

3.3.3 Fluorescence signal recovery for MCF-7 cancer cells detection

After demonstrating the quenching efficiency of GO on FAM-aptamer, we used FAM-EpCAM aptamer/GO nanocomplex as a sensing platform to detect MCF-7 cancer cells. In accordance to previous studies, GO at concentration of 100 µg/mL was chosen to prepare the nanocomplex due to its maximum quenching efficiency of 96%. Fig. 3.3.6 (a) shows the fluorescent image of FAM-aptamer/GO nanocomplex under the excitation of 465 nm, and the dark image represents completely fluorescence quenching of FAM caused by GO. Fig. 3.3.6 (b) shows the optical image of MCF-7 breast cancer cells. After incubating the quenched FAM-aptamer/GO nanocomplex with MCF-7 cells ($2*10^5$ cells/mL, 5µL) at 37℃ for 2h, the green fluorescence emission recovered substantially (Fig. 3.3.6 (c)). The fluorescence recovery was caused by the release of FAM-aptamer from GO surface as a result of specific binding between FAM-EpCAM aptamer and EpCAM protein expressed on the surface of MCF-7 cells, signifying the 'on' state of the FRET system. By measuring the aptamer-cell recognition induced signal change, MCF-7 breast cancer cells can be detected sensitively. Fig. 3.3.7 shows the relative fluorescence signal recovery rate $(F_r-F_q)/F_q$ of FAM-EpCAM aptamer/GO complex with addition of MCF-7 cells ($2*10^5$ cells/mL, 5µL) in the course of time, where F_r is the recovered fluorescence intensity of FAM-EpCAM aptamer after addition of MCF-7 cells, and F_q is the fluorescence intensity of FAM-EpCAM aptamer after GO quenching. The gradually increased relative fluorescence signal recovery rate reached a maximum of 2.85 after 72 min incubation (response time: within 80 min). As an organic fluorophore, FAM has high photobleaching rate, which is not suitable for long time storage. However, aptamer is quite stable as compared to antibody. So the FAM-aptamer/GO nanocomplex based FRET biosensor can be stored for a week. As the

results, this FAM-EpCAM aptamer/GO nanocomplex based FRET biosensing platform has big potential for application of rapid recognition of MCF-7 cancer cells.

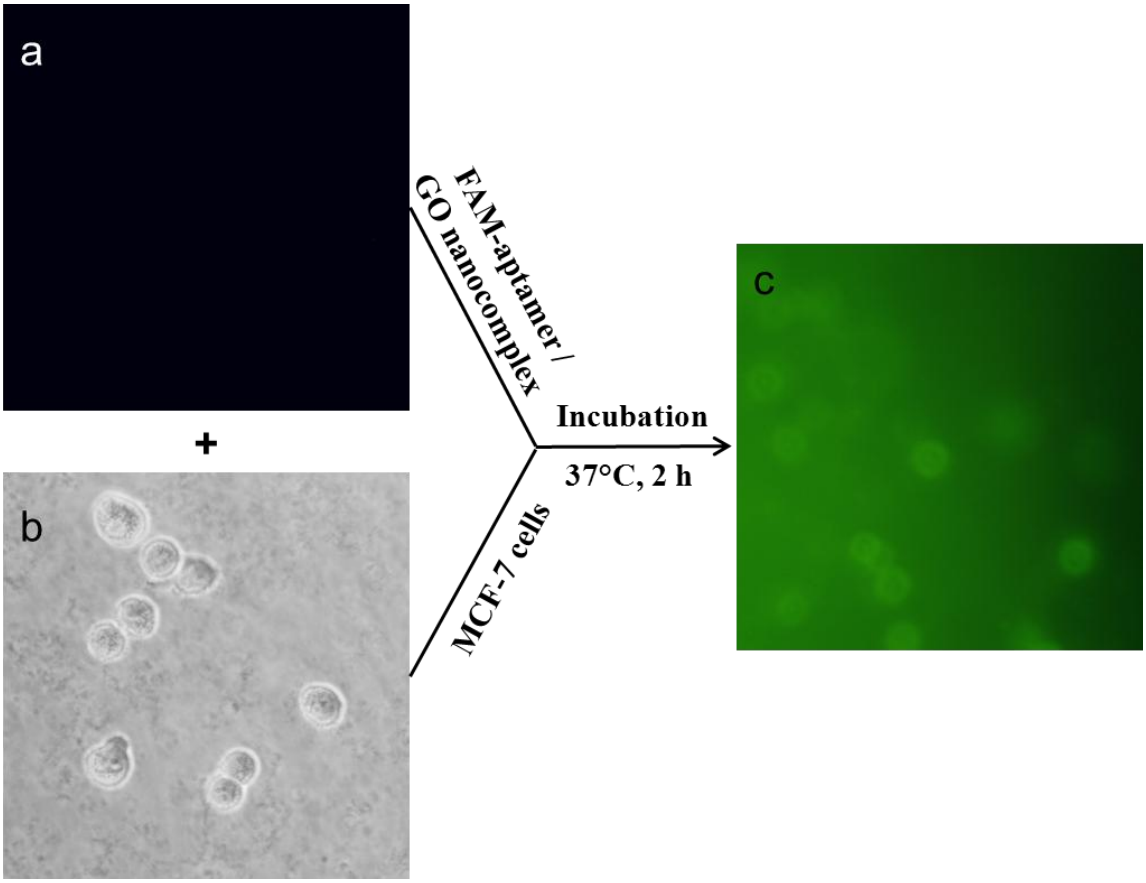

Fig. 3.3.6 Fluorescence image of FAM-aptamer/GO nanocomplex at optimal ratio (a); Optical image of MCF-7 cancer cells (b); Fluorescence image of MCF-7 cells after incubation with FAM-aptamer/GO nanocomplex for 2 h at 37 ℃ (c).

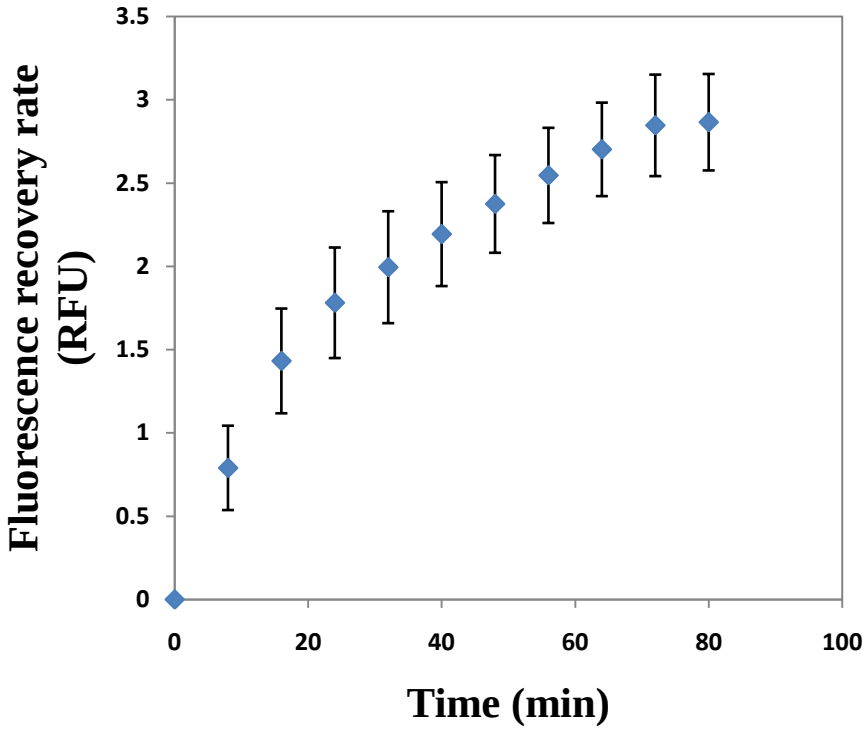

Fig. 3.3. 7 Relative fluorescence signal recovery rate of FAM-aptamer/GO nanocomplex with addition of MCF-7 cells in the course of time.

Chapter 4 Discussion

4.1 A FRET biosensor based on GQDs and AuNPs for the detection of mecA sequence of staphylococcus aureus

4.1.1 Design of sandwich structure assay

GQDs and AuNPs were used for establishing FRET assay for DNA hybridization detection. Nowadays there are two kinds of DNA hybridization detection strategy, including two complimentary DNA hybridization assay and sandwich structure hybridization assay. However, according to previous study, two complimentary DNA hybridization assay usually requires a modification process on target DNA to chemically immobilize target DNA with AuNPs before usage. Besides, the amount of target DNA extracted from samples is always limited, which requires DNA amplification step before the AuNPs-oligo conjugation process. There is no doubt that these complicated procedures are inconvenient in real applications [167, 168]. For our sandwich structure assay, target DNA does not need any modification. Reporter DNA is conjugated on AuNPs and capture DNA is immobilized on GQDs. The co-hybridization process of target DNA with GQDs-oligo (capture probe) and AuNPs-oligo (reporter probe) makes the whole assay independent from the excessive GQDs-oligo or AuNPs-oligo. Because GQD labeled probe DNA can be specifically captured by certain amount of target DNA at the first step, which determined the number of reacted GQDs-oligo and AuNPs-oligo due to the complimentary hybridization process. Thus, GQDs-oligo and AuNPs–oligo will not conjugate with each other unless target oligos are added. The number of added target oligos mainly determined the number of formation of GQD-oligo-target-oligo-

AuNPs complex, leading to subsequently fluorescence quenching effect. The quenching efficiency is dominated by the concentration of additional target DNA. Therefore, this sandwich structure assay makes label-free target DNAs to be a key factor for FRET sensing, which is much more suitable for various areas of real applications.

4.1.2 Choice of the FRET pair (GQDs and AuNPs)

Traditional FRET pairs usually include organic fluorophore, fluorescence protein and quantum dots, such as FAM, Texas red, GFP, YFP, CdSe and CdSe-Zns, and they have been extensively reported [8-11]. However, the disadvantages of high cost and photobleaching effect of organic dyes hamper their development in reliable and long term detection. The high toxicity of conventional quantum dots is not suitable for wide applications in biological field. Concerning these problems, the discovery of GQDs has arisen great attention in biological field owing to its outstanding merits, including strong and stable photoluminescence, low cytotoxicity and biocompatibility [30, 35, 36, 47]. The quantum yield of GQDs was ranged from 2% to 22% via various fabrication methods, and it can be tunable by further surface functionalization [30, 44]. Thus, in our study, GQD was chosen as the fluorescence donor, which can emit strong and stable blue photoluminescence at 460 nm with long fluorescence lifetime under continuous UV excitation. In addition, we observed that the conjugation of GQDs and oligonucleotide can exhibit stronger luminescence with enhanced quantum yield at similar emission peak when comparing with that of bare GQDs (Fig.3.1.7). These features allow GQD to be a perfect candidate for FRET biosensing system.

AuNPs are considered to be highly efficient fluorescence quenchers over longer distances [169, 170]. Unlike other dye molecules, the spherical AuNPs have no defined dipole moment, leading to possibility of energy transfer to AuNPs in any orientation of the donor relative to the surface of the AuNPs [171]. AuNPs have large absorption section, especially near the Plasmon resonance frequency range, which enhances their performance as energy acceptors [171]. Therefore, AuNP is used as fluorescence quencher in our study. Also, the absorption spectra of AuNP and AuNP-ssDNA were almost equal, both of them have absorption peak at 512 nm (Fig. 3.1.8).

Beside, the emission spectra of GQD-ssDNA and absorption spectrum of AuNP-ssDNA overlapped to a great extent (Fig. 3.1.9), and thus efficient FRET between GQD-ssDNA and AuNP-ssDNA was feasible and effective when complimentary oligonucleotide hybridization occurred.

4.1.3 Enhanced photoluminescence by EDC coating on GQDs

According to previous studies, the optical properties of GQDs are influenced by several factors, including size, shape, and surface functionality of GQDs [30, 40, 41, 43, 45]. In our study, the EDC modified GQDs exhibit the same blue emission at 460 nm as GQDs, but possess higher brightness and quantum yield. The quantum yield of EDC modified-GQD was measured to be ~19.01% (Fig. 3.1.11), which was almost two times higher than that of GQDs (quantum yield less than 10%). Because the size and shape of GQDs almost remained the same, thus the enhanced photoluminescence mainly originated from the difference in the quantity of functionalized groups on GQDs surface.

As EDC can active the COOH groups on the edge of GQDs, the COOH groups can be turned into o-acylisourea intermediate with amino on the edge. Although this intermediate is not stable, it can greatly remove the existence of oxygen-containing groups and facilitate the conjugation with amino modified oligonucleotide via amide bonding. Since the oxygen groups play a significant role in radiative recombination of localized electron-hole pairs and surface emissive traps, the decreasing oxidation degree caused by surface modification can alter the fraction of sp^2 clusters and the surface defects in GQDs, thus improving the quantum yield. Furthermore, the oxidation degree of GQDs can tailor the color of photoluminescence as well. If the oxidation degree of GQDs rich oxygen groups is high enough, the GQDs will emit green or yellow light. Then the reduction or modification of highly oxidized GQDs can tailor the luminescence into blue or green, respectively [172].

This enhanced PL of GQDs benefits the fluorescence stability and life time, which not only improve the signal to noise ratio but also produce reliable detection. These improvements contribute a lot to the sensitivity of FRET biosensor.

4.1.4 Fluorescence measurement

The accuracy of fluorescence measurement by Tecan Infinite F200 micro-plate reader (Tecan, Infinite F200, Switzerland) are affected by variation of different samples, total volume and gain values. In order to obtain accurate and comparable data, we did fluorescence measurements of buffer solution as background signal under same condition. All the collected fluorescence intensity with subtracted background signal

was used as accurate data for further calculation. For all the measurements, the total volume of samples was fixed at 100 µL with same concentration of components. Since the gain value of micro-plate reader is related to the working voltage of the detector, the establishment of optimal gain value can be crucial for better signal to background ratio. The higher gain value is set, the stronger relative fluorescence unit will be obtained. Generally, the manual gain is from 60 to 255, however, we fixed the value at 45 for all the fluorescence measurements due to the extremely high luminescence of GQDs-oligo conjugate. If the gain increases to 60, the fluorescence units will be overflow.

4.2 Graphene oxide based FRET biosensor for bacterial protein toxin (BoNT-LcA) detection

4.2.1 Design of GO-peptide FRET biosensor

Generally, we studied four FRET biosensing platforms associated with GO and peptide. As shown in Fig. 4.1.1, A/B shows the interaction between BSA passivated GO surface and peptide with and without EDC/NHS treatment, respectively. The fluorescence intensity of A/B biosensing platforms was supposed to be similar to that of bare peptide because of the absent quenching ability of surface passivated GO. Fig. 4.1.1 C displays the self-assembly absorption of GO and peptide without EDC/NHS treatment followed by BSA passivation. We hypothesized that the fluorescence intensity of C biosensing platform was initially quenched by bare GO, but subsequently restored after addition of BSA. Fig. 4.1.1 D indicates the chemical modification procedure of GO and peptide via EDC/NHS treatment followed by BSA passivation. After successfully forming the GO-peptide conjugate, the fluorescence intensity of D biosensing platform

was expected to decrease dramatically and stay at the lowest point during the following BSA passivation process. Thus, in order to construct an optimal and reliable FRET biosensing platform with high signal to noise ratio, we investigated these four fabrication strategies. Specifically, when comparing A with B biosensing platforms, we designed an experiment to testify the effectiveness of BSA passivation with and without chemical modification (Section 4.2.2). When comparing A with D biosensing platforms, we investigated the influence of BSA passivation before or after EDC/NHS modification (Section 4.2.2). When comparing C with D biosensing platform, we designed an experiment to study the stability of GO-peptide conjugates and peptide absorbed GO complex (Section 4.2.3).

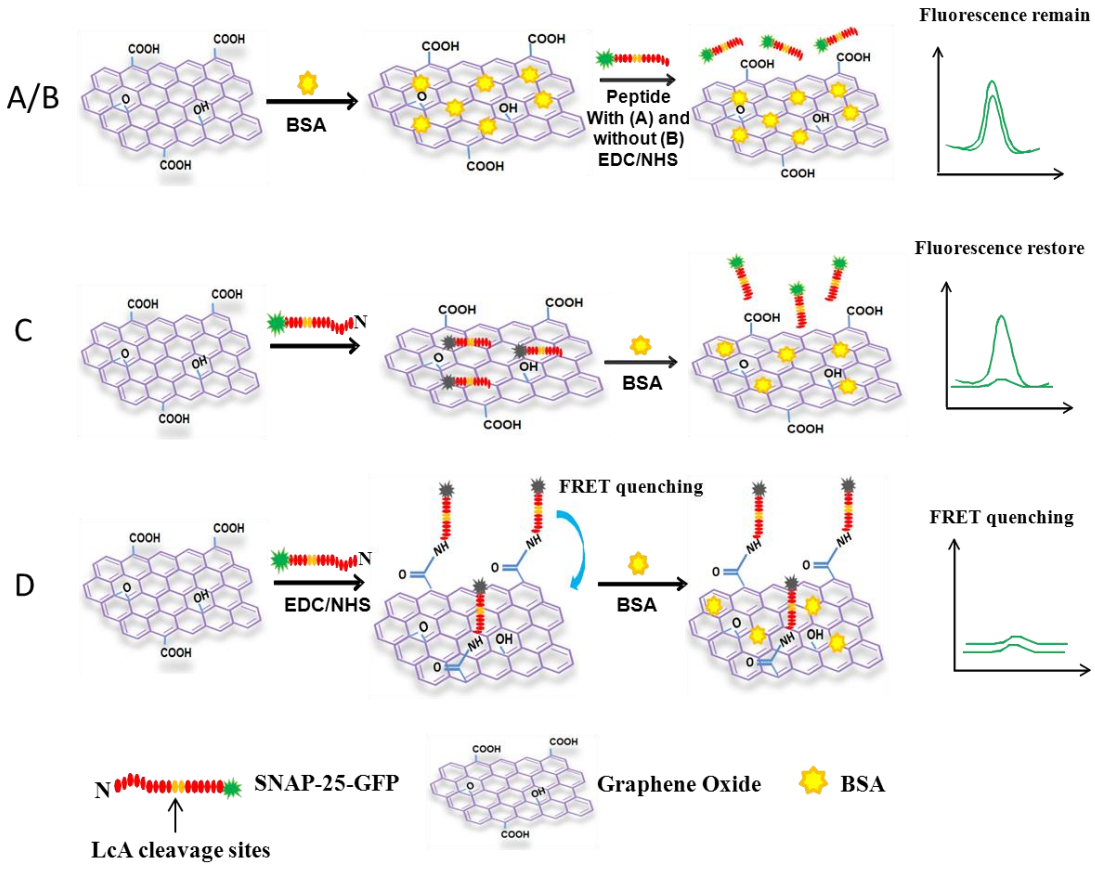

Fig. 4.1.1 Schematic design of four FRET biosensing platforms associated with GO and peptide.

4.2.2 Passivation of GO surface

Since GO is a 2D flat sheet that consists of a single layer of carbon atoms and oxygen groups bonded in both sp^2 and sp^3 hybridization, it can absorb DNA, aptamer, peptide, protein directly by π-π stacking and hydrophobic interactions [173-175]. Based on our design, if the GFP labeled SNAP-25 peptide is physically absorbed onto GO surface, the fluorescence intensity will be quenched efficiently. However, it is not desirable to use the non-specific peptide absorbed GO complex to construct an optimal FRET biosensor due to it slow stability, which can lead to not only false-positive signal but also high background noise. After BoNT-LcA cleavage, the re-absorption of released GFP-partial peptide onto GO surface may also trigger the fluorescence quenching effect. This re-absorption was considered as the key reason for false-negative signal, which hindered the sensitivity of biosensor remarkably. The high background noise was caused by the incompletely fluorescence quenching of SNAP-25-GFP by GO in protein interfered environment. Therefore, in order to construct interference-free assay with high sensitivity, we need to obtain reliable positive signal and high signal to noise ratio by preventing the non-specific binding of peptide onto GO surface.

Generally, the passivation of GO surface is essential for eliminating peptide non-specific binding. We chose two passivation elements, BSA and tris buffer, acting as large and small blocking agents. After incubating BSA and tris buffer with GO, the fully passivated GO surface can neither physically absorb nor covalently link SNAP-25-GFP so that the large intermolecular distance between GFP and GO would hinder the occurrence of FRET and remain the fluorescence signal (Section 3.2.4). The results demonstrated that both BSA and tris buffer were effective passivation agents for

minimizing the non-specific binding onto GO surface. Meanwhile the maintained fluorescence signal indicated the order of surface passivation and modification. To obtain desirable GO-peptide FRET biosensor, we should use BSA to block GO surface after chemical modification with peptide.

4.2.3 Stability of GO-peptide sensing platform

The strong covalent linkage between GO and peptide (SNAP-25-GFP) is essential for the formation of a stable sensing platform to identify the unique cleavage properties of BoNT-LcA protease. Considering the properties of GO, we have two ways to realize the GO-peptide based sensing platform, including physical absorption and chemical linkage (Fig 4.1.1 C, D). Physical absorption of peptide onto GO surface via hydrophobic and π-π stacking interactions is an intriguing synthetic method, because it is the simplest self-assembly fabrication method avoiding the complex chemical immobilization procedures [173-174]. The hydrophobic interactions are caused by hydrophobic backbones in protease and hydrophobic basal plane in GO [175]. The π-π stacking interactions mainly depend on π-interactions between aromatic rings of GO and aromatic amino acid of peptide [176].

However, we found that hydrophobic and π-π stacking interactions between peptide and GO were not stable in protein abundant medium, such as BSA solution. The absorbed peptide can be easily displayed by BSA in the course of time. This protein replacement can be explained by several reasons. Firstly, a possible reason could be the weak hydrophobic interaction between GO and peptide due to the unfavorable functional

groups on GO surface. Zhang et al. [173] demonstrated that the hydrophobic interaction of non-covalent GO-enzyme conjugate was less stable than that of reduced GO-enzyme conjugate. The stability of rGO-enzyme complex was significantly improved with the increase of GO reduction rate, which was related to the recovery of the hydrophobic aromatic rings in GO [173].Secondly, by using molecular dynamics simulation method, Zuo et al. found that π-π stacking played a key role in GO and protein integration, which could be affected by the geometry of protein and the softness of carbon based materials [177]. Protein with more aromatic residues can cause stronger π-π stacking interaction with GO backbone due to the large contacting region. As GO applied in our study is very soft and flexible, it can fit well to the structure of protein as compared to single-wall carbon nanotube (SWCNT) and fullerene (C60) [177]. Furthermore, according to Alwarappan et al. the layer number of GO had no significant effect on enzymatic π-π stacking conjugation and its stability [178]. Thus, in our study, the replacement of SNAP-25-GFP by BSA was mainly caused by different absorption affinity of proteins, which can be influenced by their size and shape. The molecular weight of BSA was 66.5 kDa, which was nearly twice larger than that of SNAP-25-GFP (38 kDa).BSA is a globular protein with three domains in line [179], while SNAP-25-GFP is a fibrous protein with α-helixsecondary structure. So, BSA equipped higher surface affinity when comparing to SNAP-25-GFP. According to Vroman effect, initially absorbed small proteins with low surface affinity will be displaced by large proteins with high surface affinity in the course of time. Thus, in this absorption competition, BSA will be the dominant banding agents over time, releasing the initially absorbed SNAP-25-GFP into solution. Noticeably, when comparing scheme B and C in Fig 4.1.1, it can be found that the displacement procedure of absorbed peptide on GO by BSA is not reversible.

Consistent results were demonstrated in Fig. 3.2.9 and Fig. 3.2.10, which strongly verified the Vroman effect. In this case, to realize stable immobilization, we chose chemical bonding strategy to covalently link peptide and GO via EDC/NHS chemical method. The immobilization of peptide onto GO surface was stable against the disturbance of rich protein in the medium.

4.2.4 Quenching efficiency of GO

GFP and GO were used as energy donor-acceptor pair in the FRET biosensor. Generally GFP exhibits bright green photoluminescence at 510 nm, which overlaps the wide absorption spectrum of GO at a large degree. This overlapping spectrum meets the necessary requirement of FRET. The covalently linkage between SNAP-25-GFP and GO made the intermolecular distance small enough to trigger fluorescence quenching effect, leading to the fluorescence ‘off’ state in the FRET system for further detection. Therefore, the quenching efficiency of GO would be crucial to determine the background signal, which affects the sensitivity of this GO-peptide based FRET biosensor significantly.

When using GO as a quencher, the 2D flat structure of GO with increasing the contact area was regarded as multiple acceptors that can interact with multiple donors simultaneously. This multiple-donor to multiple-acceptor configuration was much different from the traditional organic dye based FRET biosensor with single donor to single acceptor configuration. This would enhance the quenching efficiency to a large extent. Moreover, both Fig. 3.2.11 and Fig. 3.3.3 demonstrated that the intensity of

fluorescence emission decreased dramatically with addition of GO, and the corresponding quenching efficiency of GO at optimal concentration could reach almost 100%. Due to the high luminescence emission of GFP and good quenching efficiency of GO, a low detection limit of 1 fg was obtained for bacterial protein toxin detection.

4.3 Graphene oxide based FRET biosensor for MCF-7 cancer cells detection

4.3.1 Photobleaching effect of FAM

As FAM is an organic fluorophore, the photobleaching effect cannot be ignored. We observed significantly fluorescence bleaching phenomenon of FAM-aptamer under periodical excitation at 465 nm every five minutes (Fig. 3.3.4). It turned out that nearly 1.03% fluorescence intensity of FAM was lost in 30 min due to the low photo stability of organic fluorophores, which was not suitable for long-duration fluorescence measurement. In the same manner, the brightness of fluorescence image dimmed with continuous laser excitation during the imaging capture section, which made it more difficult to capture satisfied images. Besides, it was also hard to detect restored fluorescent signal with weak intensity by fluorescence microscope due to its low sensitivity.

4.3.2 Avoidance of false-positive signal

FAM-aptamer/GO nanocomplex was generated by a simple self-assembly procedure via π-π stacking interaction, which was unstable. And we have demonstrated

the instability of peptide absorbed GO system in the second part of this study. In this case, it can be inferred that the reason for the detachment of FAM-aptamer from GO surface includes EpCAM aptamer and EpCAM protein affinity interaction and unstable π-π stacking between aptamer and GO at the same time. Obviously, this unstable π-π stacking induced free FAM-aptamer in solution may cause false-positive signal for cancer cells detection, which hampers the reliability and sensitivity of FRET sensing strategy. In order to solve this problem and obtain reliable signal, MCF-7 cancer cells was centrifuged at 1000 rpm for 5 min after incubating with FAM-aptamer/GO nanocomplex to remove the unbound FAM-aptamer. Thus, the recovered fluorescence intensity of aptamer-cell residues was mainly depends on the specific binding of EpCAM aptamer and EpCAM protein.

Chapter 5 Conclusion

The novel graphene nanomaterial based FRET sensing platforms were developed for rapid and sensitive gene sequence hybridization, bacterial protein toxin detection and cancer cells sensing and imaging. This study includes three parts.

In the first part, a novel FRET biosensor based on GQDs and AuNPs pairs was developed for *S. aureus* specific gene detection. The sandwich structure formation caused by co-hybridization of target oligos with capture probes and reporter probes brought GQDs and AuNPs into close proximity to trigger FRET phenomena. The quenching efficiency was measured with a series of target gene oligos concentrations and the results demonstrated the feasibility of this FRET biosensor for bacteria gene detection with LOD of 1 nM. The experiments with single-base mismatched oligos and double-base mismatched oligos demonstrated the good sequence selectivity of this FRET biosensor. In this study, a short gene sequence of the whole genome of *S. aureus* was used as target oligos. In real applications, the targets should be the whole genome of bacteria extracted from raw samples. This GQDs–AuNPs FRET biosensor will be adapted for the whole genome of *S. aureus* detection in the future, which has the potential to be used as a simple, sensitive and portable platform for in-field foodborne pathogen detection in food safety and environmental screening.

In the second part, we have constructed a novel GO-peptide FRET based proteolytic biosensor for bacteria protein toxin BoNT-LcA detection. The ability of long-range energy transfer and high quenching efficiency of GO allows the assembly of lengthy peptide substrate sequence on GO surface for the access of LcA toxin. Moreover,

the large planar surface area of GO provides the simultaneous quenching capability which is unavailable to conventional FRET based BoNT enzymatic activity assay with a single-donor versus single-acceptor dye configuration. This peptide-conjugated GO complex based FRET system with BSA passivation could decrease non-specific adsorption and keep high stability in protein abundant solution compared with peptide-adsorbed GO composite. The LOD of 1 fg/mL for BoNT-LcA using this GO-peptide FRET biosensor is much lower than current dominating methods including mouse bioassay, immunoassays and the commercial available FRET kits, whose LOD is around 1 pg/mL to 1 ng/mL. This GO-peptide FRET biosensor can be easily adapted to the detection of other BoNT serotypes with alternative peptide substrates, which provides an ultrasensitive platform as BoNT enzymatic activity assay. Therefore, peptide-conjugated GO complex plus passivation is a better FRET-based peptide assay platform compared with peptide-adsorbed GO composite.

In the last part, FAM-aptamer/GO nanocomplex based FRET biosensing was fabricated for sensing and imaging circulating tumor cells (CTCs) in breast cancer. By making a use of specific affinity interaction between EpCAM aptamer and EpCAM protein expressed on the surface of cancer cells, sensitive and specific sensing and imaging of MCF-7 breast cancer cells was realized. The recovered fluorescence image and signal strongly demonstrated the feasibility of this FRET application in cancer imaging and sensing field. However, the sensitivity and limit of detection (LOD) of this FAM-aptamer/GO nanocomplex based FRET biosensing will be investigated in the future.

In this study, we have discovered the excellent photoluminescence properties of GQDs as a FRET donor, which possess higher brightness, better photo-stability and lower toxicity contrasting to organic dyes and quantum dots. We have demonstrated the super quenching ability of GO as a FRET acceptor, which offers this FRET biosensor with higher signal to noise ratio and stability comparing to traditional one. In the future work, it is possible for us to construct a FRET biosensor using GQD and GO as a FRET pairs, and make a good use of the merits of both GQDs and GO to further increase the sensitivity and the detection limit of FRET biosensors in various biological applications, such as bioimaging, biolabeling and biosensing. As GQDs and GO are both carbon based nanoparticles, they are relatively low cost and low cytotoxicity. Furthermore, the upconversion luminescence opens a door for near-IR light diagnostic using multi-photon excitation, which is less harmful to living biosystems. These properties make it possible to generate a GQD and GO based FRET biosensor with high potential of extracellular or intracellular applications.

In this study, we demonstrated the feasibility to use GQD FRET biosensor for MCF-7 cancer cell detection. The sensitivity of this GQD FRET assay need to be improved to single cell level and the specificity for cancer cell detection need to be tested with normal breast cells (MCF-10A). In the future study, it is also possible to integrate this FAM-aptamer/GO nanocomplex based FRET biosensor with microfluidic devices for field detection.

Reference

[1] Ha T, Enderle T, Ogletree D F, Chemla D S, Selvin P R, and Weiss S. Probing the interaction between two single molecules: fluorescence resonance energy transfer between a single donor and a single acceptor. Proceedings of the National Academy of Sciences, 1996, 93(13): 6264-6268.

[2] Marras S A, Kramer F R, and Tyagi S. Efficiencies of fluorescence resonance energy transfer and contact-mediated quenching in oligonucleotide probes. Nucleic Acids Research, 2002, 30(21): e122-e122.

[3] Clegg R M. Fluorescence resonance energy transfer. Current Opinion in Biotechnology, 1995, 6(1): 103-110.

[4] Szöllosi J, Damjanovich S, and Mátyus L. Application of fluorescence resonance energy transfer in the clinical laboratory: routine and research. Cytometry, 1998, 34(4): 159-179.

[5] Sapsford K E, Berti L, and Medintz I L. Materials for fluorescence resonance energy transfer analysis: beyond traditional donor–acceptor combinations. Angewandte Chemie International Edition, 2006, 45(28): 4562-4589.

[6] Kim J, Cote L J, Kim F, and Huang J. Visualizing graphene based sheets by fluorescence quenching microscopy. Journal of the American Chemical Society, 2009, 132(1): 260-267.

[7] Zimmermann T, and Terjung S. FRET Basics and Applications. EAMNET Teaching Module.

[8] Greenfield R S, and Ranzurmal S. Methods for measuring ADAMTS13 activity and protein on platelets and in plasma. U.S. Patent 7,270,976, issued September 18, 2007.

[9] Mahajan N P, Linder K, Berry G, Gordon G W, Heim R, and Herman B. Bcl-2 and Bax interactions in mitochondria probed with green fluorescent protein and fluorescence resonance energy transfer. Nature Biotechnology, 1998, 16(6): 547-552.

[10] Dong H, Gao W, Yan F, Ji H, and Ju H. Fluorescence resonance energy transfer between quantum dots and graphene oxide for sensing biomolecules. Analytical Chemistry, 2010, 82(13): 5511-5517.

[11] Liu C, Wang Z, Jia H, and Li Z. Efficient fluorescence resonance energy transfer between upconversion nanophosphors and graphene oxide: a highly sensitive biosensing platform. Chemical Communications, 2011, 47(16): 4661-4663.

[12] Ziegler C, and Göpel W. Biosensor development. Current Opinion in Chemical Biology, 1998, 2(5): 585-591.

[13] Velusamy V, Arshak K, Korostynska O, Oliwa K, and Adley C. An overview of foodborne pathogen detection: in the perspective of biosensors. Biotechnology Advances, 2010, 28(2): 232-254.

[14] Arora P, Sindhu A, Dilbaghi N, and Chaudhury A. Biosensors as innovative tools for the detection of food borne pathogens. Biosensors and Bioelectronics, 2011, 28(1): 1-12.

[15] Ko S, and Grant S A. A novel FRET-based optical fiber biosensor for rapid detection of Salmonella typhimurium. Biosensors and Bioelectronics, 2006, 21(7): 1283-1290.

[16] Wei F, and Ho C M. Aptamer-based electrochemical biosensor for Botulinum neurotoxin. Analytical and Bioanalytical Chemistry, 2009, 398(8): 1943-1948.

[17] Ferracci G, Marconi S, Mazuet C, Jover E, Blanchard M P, Seagar M, Popoff M, and Lévêque C. A label-free biosensor assay for botulinum neurotoxin B in food and human serum. Analytical Biochemistry, 2011, 410(2): 281-288.

[18] Han S M, Cho J H, Cho I H, Paek E H, Oh H B, Kim B S, Ryu C, Lee K, Kim Y K, and Paek S H. Plastic enzyme-linked immunosorbent assays (ELISA)-on-a-chip biosensor for botulinum neurotoxin A. Analytica Chimica Acta, 2007, 587(1): 1-8.

[19] Chan L L, Gosangari S L, Watkin K L, and Cunningham B T. A label-free photonic crystal biosensor imaging method for detection of cancer cell cytotoxicity and proliferation. Apoptosis, 2007, 12(6): 1061-1068.

[20] Maesawa C, Inaba T, Sato H, Iijima S, Ishida K, Terashima M, Sato R, Suzuki M, Yashima A, Ogasawara S, Oikawa H, Sato N, Saito K, and Masuda T. A rapid biosensor chip assay for measuring of telomerase activity using surface plasmon resonance. Nucleic Acids Research, 2003, 31(2): e4-e4.

[21] Schmilovitch Z, Mizrach A, Alchanatis V, Kritzman G, Korotic R, Irudayaraj J, and Debroy C. Detection of bacteria with low-resolution Raman spectroscopy. Transactions of the ASAE, 2005, 48(5): 1843-1850.

[22] Su Y L, Li J R, Jiang L, and Cao J. Biosensor signal amplification of vesicles functionalized with glycolipid for colorimetric detection of Escherichia coli. Journal of Colloid and Interface Science, 2005, 284(1): 114-119.

[23] Vaughan R D, O'sullivan C K, and Guilbault G G. Development of a quartz crystal microbalance (QCM) immunosensor for the detection of Listeria monocytogenes. Enzyme and Microbial Technology, 2001, 29(10): 635-638.

[24] Micheli L, Grecco R, Badea M, Moscone D, and Palleschi G. An electrochemical immunosensor for aflatoxin M1 determination in milk using screen-printed electrodes. Biosensors and Bioelectronics, 2005, 21(4): 588-596.

[25] Yang L, Li Y, Griffis C L, and Johnson M G. Interdigitated microelectrode (IME) impedance sensor for the detection of viable Salmonella typhimurium. Biosensors and Bioelectronics, 2004, 19(10): 1139-1147.

[26] Oh E, Hong M Y, Lee D, Nam S H, Yoon H C, and Kim H S. Inhibition assay of biomolecules based on fluorescence resonance energy transfer (FRET) between quantum dots and gold nanoparticles. Journal of the American Chemical Society, 2005, 127(10): 3270-3271.

[27] Gill R, Willner I, Shweky I, and Banin U. Fluorescence resonance energy transfer in CdSe/ZnS-DNA conjugates: probing hybridization and DNA cleavage. Journal of Physical Chemistry B, 2005, 109(49): 23715-23719.

[28] Sekar R B, and Periasamy A. Fluorescence resonance energy transfer (FRET) microscopy imaging of live cell protein localizations. Journal of Cell Biology, 2003, 160(5): 629-633.

[29] Sourjik V, and Berg H C. Binding of the Escherichia coli response regulator CheY to its target measured in vivo by fluorescence resonance energy transfer. Proceedings of the National Academy of Sciences, 2002, 99(20): 12669-12674.

[30] Zhu S, Zhang J, Tang S, Qiao C, Wang L, Wang H, Liu X, Li B, Li Y, Yu W, Wang X, Sun H, and Yang B. Surface chemistry routes to modulate the photoluminescence of graphene quantum dots: from fluorescence mechanism to up-conversion bioimaging Applications. Advanced Functional Materials, 2012, 22(22): 4732-4740.

[31] Wu W, Shen J, Banerjee P, and Zhou S. Core–shell hybrid nanogels for integration of optical temperature-sensing, targeted tumor cell imaging, and combined chemo-photothermal treatment. Biomaterials, 2010, 31(29): 7555-7566.

[32] Gao J, Chen K, Miao Z, Ren G, Chen X, Gambhir S S, and Cheng Z. Affibody-based nanoprobes for HER2-expressing cell and tumor imaging. Biomaterials, 2011, 32(8): 2141-2148.

[33] Li J M, Zhao M X, Su H, Wang Y Y, Tan C P, Ji L N, and Mao Z W. Multifunctional quantum-dot-based siRNA delivery for HPV18 E6 gene silence and intracellular imaging. Biomaterials, 2011, 32(31): 7978-7987.

[34] Ruan J, Song H, Qian Q, Li C, Wang K, Bao C, and Cui D. HER2 monoclonal antibody conjugated RNase-A-associated CdTe quantum dots for targeted imaging and therapy of gastric cancer. Biomaterials, 2012, 33(29): 7093-7102.

[35] Shen J, Zhu Y, Chen C, Yang X, and Li C. Facile preparation and upconversion luminescence of graphene quantum dots. Chemical Communications, 2011, 47(9): 2580-2582.

[36] Pan D, Zhang J, Li Z, Wu C, Yan X, and Wu M. Observation of pH-, solvent-, spin-, and excitation-dependent blue photoluminescence from carbon nanoparticles. Chemical Communications, 2010, 46(21): 3681-3683.

[37] Li D, Müller M B, Gilje S, Kaner R B, and Wallace G G. Processable aqueous dispersions of graphene nanosheets. Nature Nanotechnology, 2008, 3(2): 101-105.

[38] Eda G, Lin Y Y, Mattevi C, Yamaguchi H, Chen H A, Chen I, Chen C W, and Chhowalla M. Blue photoluminescence from chemically derived graphene oxide. Advanced Materials, 2010, 22(4): 505-509.

[39] Kim S, Hwang S W, Kim M K, Shin D Y, Shin D H, Kim C O, and Yang S B, Park J H, Hwang E, Choi S H, Ko G, Sim S, Sone C, Choi H J, Bae S, and Hong B H. Anomalous behaviors of visible luminescence from graphene quantum dots: interplay between size and shape. ACS Nano, 2012, 6(9): 8203-8208.

[40] Pan D, Zhang J, Li Z, and Wu M. Hydrothermal route for cutting graphene sheets into blue-luminescent graphene quantum dots. Advanced Materials, 2010. 22(6): 734-738.

[41] Zhu S, Zhang J, Qiao C, Tang S, Li Y, Yuan W, Li B, Tian L, Liu F, Hu R, Gao H, Wei H, Zhang H, Sun H, and Yang B. Strongly green-photoluminescent graphene quantum dots for bioimaging applications. Chemical Communications, 2011, 47(24): 6858-6860.

[42] Li Y, Hu Y, Zhao Y, Shi G, Deng L, Hou Y, and Qu L. An electrochemical avenue to green-luminescent graphene quantum dots as potential electron-acceptors for photovoltaics. Advanced Materials, 2011, 23(6): 776-780.

[43] Liu F, Jang M H, Ha H D, Kim J H, Cho Y H, and Seo T S. Facile synthetic method for pristine graphene quantum dots and graphene oxide quantum dots: origin of blue and green luminescence. Advanced Materials, 2013, 25(27): 3657-3662.

[44] Tetsuka H, Asahi R, Nagoya A, Okamoto K, Tajima I, Ohta R, and Okamoto A. Optically tunable amino-functionalized graphene quantum dots. Advanced Materials, 2012, 24(39): 5333-5338.

[45] Zhang M, Bai L, Shang W, Xie W, Ma H, Fu Y, Fang D. Sun H, Fan L, Han M, Liu C, and Yang S. Facile synthesis of water-soluble, highly fluorescent graphene quantum dots as a robust biological label for stem cells. Journal of Materials Chemistry, 2012, 22(15): 7461-7467.

[46] Yang F, Zhao M, Zheng B, Xiao D, Wu L, and Guo Y. Influence of pH on the fluorescence properties of graphene quantum dots using ozonation pre-oxide hydrothermal synthesis. Journal of Materials Chemistry, 2012, 22(48): 25471-25479.

[47] Hu C, Liu Y, Yang Y, Cui J, Huang Z, Wang Y, Yang L, Wang H, Xiao Y, and Rong J. One-step preparation of nitrogen-doped graphene quantum dots from oxidized debris of graphene oxide. Journal of Materials Chemistry B, 2013, 1(1): 39-42.

[48] Zhang L, Xing Y, He N, Zhang Y, Lu Z, Zhang J, and Zhang Z. Preparation of graphene quantum dots for bioimaging application. Journal of Nanoscience and Nanotechnology, 2012, 12(3): 2924-2928.

[49] Shen J, Zhu Y, Yang X, Zong J, Zhang J, and Li C. One-pot hydrothermal synthesis of graphene quantum dots surface-passivated by polyethylene glycol and their photoelectric conversion under near-infrared light. New Journal of Chemistry, 2012, 36(1): 97-101.

[50] Sun Y P, Zhou B, Lin Y, Wang W, Fernando K S, Pathak P, Meziani M J, Harruff B A, Wang X, Wang H, Luo P G, Yang H, Kose M E, Chen B, Veca L M, and Xie S Y. Quantum-sized carbon dots for bright and colorful photoluminescence. Journal of the American Chemical Society, 2006, 128(24): 7756-7757.

[51] Zhuo S, Shao M, and Lee S T. Upconversion and downconversion fluorescent graphene quantum dots: ultrasonic preparation and photocatalysis. ACS Nano, 2012, 6(2): 1059-1064.

[52] Peng J, Gao W, Gupta B K, Liu Z, Romero-Aburto R, Ge L, Song L, Alemany L B, Zhan X, Gao G, Vithayathil S A, Kaipparettu B A, Marti A A, Hayashi T, Zhu J J,

and Ajayan P M. Graphene quantum dots derived from carbon fibers. Nano Letters, 2012, 12(2): 844-849.

[53] Liu Z, Robinson J T, Sun X, and Dai H. PEGylated nanographene oxide for delivery of water-insoluble cancer drugs. Journal of the American Chemical Society, 2008, 103(33): 10876-10877.

[54] Geim A K, and Novoselov K S. The rise of graphene. Nature Materials, 2007, 6(3): 183-191.

[55] Kroto H W, Heath J R, O'Brien S C, Curl R F, and Smalley R E. C 60: buckminsterfullerene. Nature, 1985, 318(6042): 162-163.

[56] Boehm H P. The first observation of carbon nanotubes. Carbon, 1997, 35(4): 581-584.

[57] Novoselov K S, Jiang D, Schedin F, Booth T J, Khotkevich V V, Morozov S V, and Geim A K. Two-dimensional atomic crystals. Proceedings of the National Academy of Sciences of the United States of America, 2005, 102(30): 10451-10453.

[58] Brodie B C. Sur le poids atomique du graphite. Annales de Chimie et de Physique, 1860, 59: 466-472.

[59] Staudenmaier L. Verfahren zur darstellung der graphitsäure. Berichte der deutschen chemischen Gesellschaft, 1898, 31(2): 1481-1487.

[60] Hummers J, William S, and Offeman R E. Preparation of graphitic oxide. Journal of the American Chemical Society, 1958, 80(6): 1339-1339.

[61] Dreyer D R, Park S, Bielawski C W, and Ruoff R S. The chemistry of graphene oxide. Chemical Society Reviews, 2010, 39(1): 228-240.

[62] Hontoria-Lucas C, Lopez-Peinado A J, López-González J D, Rojas-Cervantes M L, and Martin-Aranda R M. Study of oxygen-containing groups in a series of

graphite oxides: physical and chemical characterization. Carbon, 1995, 33(11): 1585-1592.

[63] Akhavan O. The effect of heat treatment on formation of graphene thin films from graphene oxide nanosheets. Carbon, 2010, 48(2): 509-519.

[64] Paredes J I, Villar-Rodil S, Solis-Fernandez P, Martinez-Alonso A, and Tascon J M D. Atomic force and scanning tunneling microscopy imaging of graphene nanosheets derived from graphite oxide. Langmuir, 2009, 25(10): 5957-5968.

[65] Huang P, Xu C, Lin J, Wang C, Wang X, Zhang C, Zhou X, Guo S, and Cui D. Folic acid-conjugated graphene oxide loaded with photosensitizers for targeting photodynamic therapy. Theranostics, 2011, 1: 240.

[66] Wilson N R, Pandey P A, Beanland R, Young R J, Kinloch I A, Gong L, Liu Z, Suenaga K, Rourke J P, York S J, and Sloan J. Graphene oxide: structural analysis and application as a highly transparent support for electron microscopy. ACS Nano, 2009, 3(9): 2547-2556.

[67] Mattevi C, Eda G, Agnoli S, Miller S, Mkhoyan K A, Celik O, Mastrogiovanni D, Granozzi G, Garfunkel E, and Chhowalla M. Evolution of electrical, chemical, and structural properties of transparent and conducting chemically derived graphene thin films. Advanced Functional Materials, 2009, 19(16): 2577-2583.

[68] Park S, and Ruoff R S. Chemical methods for the production of graphenes. Nature Nanotechnology, 2009, 4(4): 217-224.

[69] Eda G, Mattevi C, Yamaguchi H, Kim H, and Chhowalla M. Insulator to semimetal transition in graphene oxide. The Journal of Physical Chemistry C, 2009, 113(35): 15768-15771.

[70] Cai D, and Song M. Preparation of fully exfoliated graphite oxide nanoplatelets

in organic solvents. Journal of Materials Chemistry, 2007, 17(35): 3678-3680.

[71] Paredes J I, Villar-Rodil S, Martinez-Alonso A, and Tascon J M D. Graphene oxide dispersions in organic solvents. Langmuir, 2008, 24(19): 10560-10564.

[72] Novoselov K S. Graphene: Materials in the flatland. Reviews of Modern Physics, 2011, 83(3): 837.

[73] Pavlidis I V, Patila M, Bornscheuer U T, Gournis D, and Stamatis H. Graphene-based nanobiocatalytic systems: recent advances and future prospects. Trends in Biotechnology, 2014, 32(6): 312-320.

[74] Zheng W, Shen B, and Zhai W. Surface functionalization of graphene with polymers for enhanced properties, INTECH Open Access Publisher, 2013.

[75] Kanchanapally R, Fan Z, Singh A K, Sinha S S, and Ray P C. Multifunctional hybrid graphene oxide for label-free detection of malignant melanoma from infected blood. Journal of Materials Chemistry B, 2014, 2(14): 1934-1937.

[76] Jain S L, and Kumar P. Photocatalytic reduction of carbon dioxide to methanol using ruthenium trinuclear polyazine complex immobilized to graphene oxide under visible light irradiation. Journal of Materials Chemistry A, 2014, 2: 11246.

[77] Ren X, Bai H, Pan Y, Tong W, Qin P, Yan H, Deng S, Zhong R, Qin W, and Qian X. A graphene oxide-based immobilized PNGase F reagent for highly efficient N-glycan release and MALDI-TOF MS profiling. Analytical Methods, 2014, 6(8): 2518-2525.

[78] Umasankar Y, Unnikrishnan B, Chen S M, and Ting T W. Graphene impregnated with horseradish peroxidase multimer for the determination of hydrogen peroxide. Analytical Methods, 2012, 4(11): 3653-3660.

[79] Jiang H, Lo C W, and Zhu D. Infrared light-and thermal-responsive graphene oxide hydrogel polymer composites. U.S. Patent Application 13/307,572, filed November 30, 2011.

[80] Wu M, Kempaiah R, Huang P J, Maheshwari V, and Liu J. Adsorption and desorption of DNA on graphene oxide studied by fluorescently labeled oligonucleotides. Langmuir, 2011, 27(6): 2731-2738.

[81] Zhang M, Yin B C, Tan W, and Ye B C. A versatile graphene-based fluorescence 'on/off' switch for multiplex detection of various targets. Biosensors and Bioelectronics, 2011, 26(7): 3260-3265.

[82] JamesáYang C. Graphene oxide-protected DNA probes for multiplex microRNA analysis in complex biological samples based on a cyclic enzymatic amplification method. Chemical Communications, 2012, 48(2): 194-196.

[83] Li S, Aphale A N, Macwan I G, Patra P K, Gonzalez W G, Miksovska J, and Leblanc R M. Graphene oxide as a quencher for fluorescent assay of amino acids, peptides, and proteins. ACS Applied Materials & Interfaces, 2012, 4(12): 7069-7075.

[84] Kagan M R, and McCreery R L. Reduction of fluorescence interference in Raman spectroscopy via analyte adsorption on graphitic carbon. Analytical Chemistry, 1994, 66(23): 4159-4165.

[85] Treossi E, Melucci M, Liscio A, Gazzano M, Samorì P, and Palermo V. High-contrast visualization of graphene oxide on dye-sensitized glass, quartz, and silicon by fluorescence quenching. Journal of the American Chemical Society, 2009, 131(43): 15576-15577.

[86] Lu C H, Li J, Liu J J, Yang H H, Chen X, and Chen G N. Increasing the sensitivity and single-base mismatch selectivity of the molecular beacon using

graphene oxide as the “nanoquencher”. Chemistry-A European Journal, 2010, 16(16): 4889-4894.

[87] Sheng L, Ren J, Miao Y, Wang J, and Wang E. PVP-coated graphene oxide for selective determination of ochratoxin A via quenching fluorescence of free aptamer. Biosensors and Bioelectronics, 2011, 26(8): 3494-3499.

[88] Swathi R S, and Sebastian K L. Long range resonance energy transfer from a dye molecule to graphene has (distance)−4 dependence. The Journal of Chemical Physics, 2009, 130(8): 086101.

[89] Swathi R S, and Sebastian K L. Resonance energy transfer from a dye molecule to graphene. The Journal of Chemical Physics, 2008, 129(5): 054703.

[90] Lu C H, Yang H H, Zhu C L, Chen X, and Chen G N. A graphene platform for sensing biomolecules. Angewandte Chemie, 2009, 121(26): 4879-4881.

[91] He S, Song B, Li D, Zhu C, Qi W, Wen Y, Wang L, Song S, Fang H, and Fan C. A graphene nanoprobe for rapid, sensitive, and multicolor fluorescent DNA analysis. Advanced Functional Materials, 2010, 20(3): 453-459.

[92] Orenstein A. The discovery and naming of Staphylococcus aureus. Gevonden op, 2011.

[93] Miao T, Wang Z, Li S, and Wang X. Sensitive fluorescent detection of Staphylococcus aureus using nanogold linked CdTe nanocrystals as signal amplification labels. Microchimica Acta, 2011, 172(3-4): 431-437.

[94] Leonard P, Hearty S, Brennan J, Dunne L, Quinn J, Chakraborty T, and O’Kennedy R. Advances in biosensors for detection of pathogens in food and water. Enzyme and Microbial Technology, 2003, 23(1): 3-13.

[95] Pinto B, Chenoll E, and Aznar R. Identification and typing of food-borne Staphylococcus aureus by PCR-based techniques. Systematic and Applied Microbiology, 2005, 28(4): 340-352.

[96] Quiel A, Jürgen B, Piechotta G, Le Foll A P, Ziebandt A K, Kohler C, Köster D, Engelmann S, Erck C, Hintsche R, Wehland J, Hecker M, and Schweder T. Electrical protein array chips for the detection of staphylococcal virulence factors. Applied Microbiology and Biotechnology, 2010, 85(5): 1619-1627.

[97] Storhoff J J, Marla S S, Bao P, Hagenow S, Mehta H, Lucas A, Garimella V, Patno T, Buckingham W, Cork W, and Müller U R. Gold nanoparticle-based detection of genomic DNA targets on microarrays using a novel optical detection system. Biosensors and Bioelectronics, 2004, 19(8): 875-883.

[98] Carbonnelle E, Beretti J L, Cottyn S, Quesne G, Berche P, Nassif X, and Ferroni A. Rapid identification of Staphylococci isolated in clinical microbiology laboratories by matrix-assisted laser desorption ionization-time of flight mass spectrometry. Journal of Clinical Microbiology, 2007, 45(7): 2156-2161.

[99] Hochel I, Slavíčková D, Viochna D, Škvor J, and Steinhauserová I. Detection of Campylobacter species in foods by indirect competitive ELISA using hen and rabbit antibodies. Food and Agricultural Immunology, 2007, 18(3-4): 151-167.

[100] Boujday S, Briandet R, Salmain M, Herry J M, Marnet P G, Gautier M, and Pradier C M. Detection of pathogenic Staphylococcus aureus bacteria by gold based immunosensors. Microchimica Acta, 2008, 163(3-4): 203-209.

[101] Grund S, Pietzonka S, Michel S, and Adams O. Serum antibodies against native and denaturated hemagglutinin glycoproteins detected by ELISA as correlates of

protection after influenza vaccination in healthy vaccinees and in kidney transplant recipients. Journal of Virological Methods, 2013, 193(2): 558-564.

[102] Hoffmann B, Harder T, Starick E, Depner K, Werner O, and Beer M. Rapid and highly sensitive pathotyping of avian influenza A H5N1 virus by using real-time reverse transcription-PCR. Journal of Clinical Microbiology, 2007, 45(2): 600-603.

[103] Alarcon B, Vicedo B, and Aznar R. PCR-based procedures for detection and quantification of Staphylococcus aureus and their application in food. Journal of Applied Microbiology, 2006, 100(2): 352-364.

[104] Brakstad O G, Aasbakk K, and Maeland J A. Detection of Staphylococcus aureus by polymerase chain reaction amplification of the nuc gene. Journal of Clinical Microbiology, 1992, 30(7): 1654-1660.

[105] Xiao X, Yang X, Liu T, Chen Z, Chen L, Li H, and Deng L. Preparing a highly specific inert immunomolecular-magnetic beads for rapid detection and separation of *S. aureus* and group G Streptococcus. Applied Microbiology and Biotechnology, 2007, 75(5): 1209-1216.

[106] Ruan M, Niu C G, Zeng G M, Qin P Z, Wang X Y, Huang D W, Huang J, and Fan C Z. Rapid detection of Staphylococcus aureus via a sensitive DNA hybridization assay based on a long-lifetime luminescent europium marker. Microchimica Acta, 2011, 175(1-2): 105-112.

[107] Niemeyer C M, and Blohm D. DNA microarrays. Angewandte Chemie International Edition, 1999, 38(19): 2865-2869.

[108] Mao X, Yang L, Su X L, and Li Y. A nanoparticle amplification based quartz crystal microbalance DNA sensor for detection of Escherichia coli O157: H7. Biosensors and Bioelectronics, 2006, 21(7): 1178-1185.

[109] Nawattanapaiboon K, Kiatpathomchai W, Santanirund P, Wongsakulyanon A, Sutapun B, and Srikhirin T. Label-free detection of meca-mediated methicillin-resistant Staphylococcus aureus (MRSA) using surface plasmon resonance spectroscopy. In The 15th International Conference on Biomedical Engineering, pp. 845-848. Springer International Publishing, 2014.

[110] Bally M, Halter M, Vörös J, and Grandin H M. Optical microarray biosensing techniques. Surface and Interface Analysis, 2006, 38(11): 1442-1458.

[111] Montecucco C, and Molgó J. Botulinal neurotoxins: revival of an old killer. Current Opinion in Pharmacology, 2005, 5(3): 274-279.

[112] Lamanna C. The Most Poisonous Poison What do we know about the toxin of botulism? What are the problems to be solved? Science, 1959, 130(3378): 763-772.

[113] Arnon S S, Schechter R, Inglesby T V, Henderson D A, Bartlett J G, Ascher M S, Eitzen E, …, and Tonat K. Botulinum toxin as a biological weapon: medical and public health management. Journal of American Medical Association, 2001, 285(8): 1059-1070.

[114] Pellizzari R, Rossetto O, Schiavo G, and Montecucco C. Tetanus and botulinum neurotoxins: mechanism of action and therapeutic uses. Philosophical Transactions of the Royal Society of London. Series B: Biological Sciences, 1999, 345(1381): 259-268.

[115] Lebeda F J, Adler M, Erickson K, and Chushak Y. Onset dynamics of type A botulinum neurotoxin-induced paralysis. Journal of Pharmacokinetics and Pharmacodynamics, 2008, 35(3): 251-267.

[116] Shapiro R L, Hatheway C, and Swerdlow D L. Botulism in the United States: a clinical and epidemiologic review. Annals of Internal Medicine, 1998, 129(3): 221-

228.

[117] Cai S, Singh B R, and Sharma S. Botulism diagnostics: from clinical symptoms to in vitro assays. Critical Reviews in Microbiology, 2007, 33(2): 109-125.

[118] Sharma S K, Ferreira J L, Eblen B S, and Whiting R C. Detection of type A, B, E, and F Clostridium botulinum neurotoxins in foods by using an amplified enzyme-linked immunosorbent assay with digoxigenin-labeled antibodies. Applied and Environmental Microbiology, 2006, 72(2): 1231-1238.

[119] Lindström M, and Korkeala H. Laboratory diagnostics of botulism. Clinical Microbiology Reviews, 2006, 19(2): 298-314.

[120] Gessler F, Hampe K, Schmidt M, and Böhnel H. Immunomagnetic beads assay for the detection of botulinum neurotoxin types C and D. Diagnostic Microbiology and Infectious Disease, 2006, 56(3): 225-232.

[121] Rivera V R, Gamez F J, Keener W K, White J A, and Poli M A. Rapid detection of Clostridium botulinum toxins A, B, E, and F in clinical samples, selected food matrices, and buffer using paramagnetic bead-based electrochemiluminescence detection. Analytical Biochemistry, 2006, 353(2): 248-256.

[122] Gessler F, Pagel-Wieder S, Avondet M A, and Böhnel H. Evaluation of lateral flow assays for the detection of botulinum neurotoxin type A and their application in laboratory diagnosis of botulism. Diagnostic Microbiology and Infectious Disease, 2007, 57(3): 243-249.

[123] Attrée O, Guglielmo-Viret V, Gros V, and Thullier P. Development and comparison of two immunoassay formats for rapid detection of botulinum neurotoxin type A. Journal of Immunological Methods, 2007, 325(1): 78-87.

[124] Sapsford K E, Sun S, Francis J, Sharma S, Kostov Y, and Rasooly A. A

fluorescence detection platform using spatial electroluminescent excitation for measuring botulinum neurotoxin A activity. Biosensors and Bioelectronics, 2008, 24(4): 618-625.

[125] Ligler F S, Sapsford K E, Golden J P, Shriver-Lake L C, Taitt C R, Dyer M A, Barone S, and Myatt C J. The array biosensor: portable, automated systems. Analytical Sciences, 2007, 23(1): 5.

[126] Kalb S R, Smith T J, Moura H, Hill K, Lou J, Geren I N, Garcia-Rodriguez C, … and Barr J R. The use of Endopep-MS to detect multiple subtypes of botulinum neurotoxins A, B, E, and F. International Journal of Mass Spectrometry, 2008, 278(2): 101-108.

[127] Lévêque C, Ferracci G, Maulet Y, Grand-Masson C, Blanchard M P, Seagar M, and El Far O. A substrate sensor chip to assay the enzymatic activity of Botulinum neurotoxin A. Biosensors and Bioelectronics, 2013, 49: 276-281.

[128] Schmidt J J, and Stafford R G. Fluorigenic substrates for the protease activities of botulinum neurotoxins, serotypes A, B, and F. Applied and Environmental Microbiology, 2003, 69(1): 297-303.

[129] Anne C, Cornille F, Lenoir C, and Roques B P. High-throughput fluorogenic assay for determination of botulinum type B neurotoxin protease activity. Analytical Biochemistry, 2001, 291(2): 253-261.

[130] Dong M, Tepp W H, Johnson E A, and Chapman E R. Using fluorescent sensors to detect botulinum neurotoxin activity in vitro and in living cells. Proceedings of the National Academy of Sciences of the United States of America, 2004, 101(41): 14701-14706.

[131] Gilmore M A, Williams D, Okawa Y, Holguin B, James N G, Ross J A, Aoki K

R, Jameson D M, and Steward L E. Depolarization after resonance energy transfer (DARET): a sensitive fluorescence-based assay for botulinum neurotoxin protease activity. Analytical Biochemistry, 2011, 413(1): 36-42.

[132] Mangru S, Bentz B L, Davis T J, Desai N, Stabile P J, Schmidt J J, Millard C B, Bavari S, and Kodukula K. Integrated bioassays in microfluidic devices: Botulinum toxin assays. Journal of Biomolecular Screening, 2005, 10(8): 788-794.

[133] Sun S, Ossandon M, Kostov Y, and Rasooly A. Lab-on-a-chip for botulinum neurotoxin a (BoNT-A) activity analysis. Lab Chip, 2009, 9(22): 3275-3281.

[134] Chen J T, Fu Y J, An Q F, Lo S C, Huang S H, Hung W S, Hu C C, Lee K R, and Lai J Y. Tuning nanostructure of graphene oxide/polyelectrolyte LbL assemblies by controlling pH of GO suspension to fabricate transparent and super gas barrier films. Nanoscale, 2013, 5(19): 9081-9088.

[135] Baeuerle P A, and Gires O. EpCAM (CD326) finding its role in cancer. British Journal of Cancer, 2007, 96(3), 417-423.

[136] Dalerba P, Dylla S J, Park I K, Liu R, Wang X, Cho R W, Hoey T, … and Clarke M F. Phenotypic characterization of human colorectal cancer stem cells. Proceedings of the National Academy of Sciences, 2007, 104(24): 10158-10163.

[137] Gastl G, Spizzo G, Obrist P, Dünser M, and Mikuz G. Ep-CAM overexpression in breast cancer as a predictor of survival. The Lancet, 2000, 356(9246): 1981-1982.

[138] Varga M, Obrist P, Schneeberger S, Mühlmann G, Felgel-Farnholz C, Fong D, Zitt M, … and Spizzo G. Overexpression of epithelial cell adhesion molecule antigen in gallbladder carcinoma is an independent marker for poor survival. Clinical Cancer Research, 2004, 10(9): 3131-3136.

[139] Li C, Heidt D G, Dalerba P, Burant C F, Zhang L, Adsay V, Wicha M, Clarke M F, and Simeone D M. Identification of pancreatic cancer stem cells. Cancer Research, 2007, 67(3): 1030-1037.

[140] Yamashita T, Ji J, Budhu A, Forgues M, Yang W, Wang H Y, Jia H, … and Wang X W. EpCAM-positive hepatocellular carcinoma cells are tumor-initiating cells with stem/progenitor cell features. Gastroenterology, 2009, 136(3): 1012-1024.

[141] World Cancer Report. International Agency for Research on Cancer. 2008. Retrieved 2011-02-26.

[142] World Cancer Report 2014. World Health Organization. 2014. pp. Chapter 1.1. ISBN 92-832-0429-8.

[143] Ross A A, Cooper B W, Lazarus H M, Mackay W, Moss T J, Ciobanu N, Tallman M S, Kennedy M J, Davidson N E, and Sweet D. Detection and viability of tumor cells in peripheral blood stem cell collections from breast cancer patients using immunocytochemical and clonogenic assay techniques. Blood, 1993, 82(9): 2605-2610.

[144] Dunphy C H, Orton S O, and Mantell J. Relative contributions of enzyme cytochemistry and flow cytometric immunophenotyping to the evaluation of acute myeloid leukemias with a monocytic component and of flow cytometric immunophenotyping to the evaluation of absolute monocytoses. American Journal of Clinical Pathology, 2004, 122(6): 865-874.

[145] Ghossein R A, and Bhattacharya S. Molecular detection and characterisation of circulating tumour cells and micrometastases in solid tumours. European Journal of Cancer, 2000, 36(13): 1681-1694.

[146] Gubala V, Harris L F, Ricco A J, Tan M X, and Williams D E. Point of care diagnostics: status and future. Analytical Chemistry, 2011, 84(2): 487-515.

[147] Mostert B, Sleijfer S, Foekens J A, and Gratama J W. Circulating tumor cells (CTCs): detection methods and their clinical relevance in breast cancer. Cancer Treatment Reviews, 2009, 35(5): 463-474.

[148] Schwartzberg L S. Clinical experience with edrecolomab: a monoclonal antibody therapy for colorectal carcinoma. Critical Reviews in Oncology/Hematology, 2001, 40(1): 17-24.

[149] Armstrong A, and Eck S L. A new therapeutic target for an old cancer antigen. Cancer Biology & Therapy, 2003, 2(4): 320-325.

[150] Song Y, Zhu Z, An Y, Zhang W, Zhang H, Liu D, Yu C, Duan W, and Yang J C. Selection of DNA aptamers against epithelial cell adhesion molecule for cancer cell imaging and circulating tumor cell capture. Analytical Chemistry, 2013, 85(8): 4141-4149.

[151] Bagalkot V, Zhang L, Levy-Nissenbaum E, Jon S, Kantoff P W, Langer R, and Farokhzad O C. Quantum dot-aptamer conjugates for synchronous cancer imaging, therapy, and sensing of drug delivery based on bi-fluorescence resonance energy transfer. Nano Letters, 2007, 7(10): 3065-3070.

[152] Huang P J, and Liu J. DNA-length-dependent fluorescence signaling on graphene oxide surface. Small, 2012, 8(7): 977-983.

[153] Wang Y, Li Z, Hu D, Lin C T, Li J, and Lin Y. Aptamer/graphene oxide nanocomplex for in situ molecular probing in living cells. Journal of the American Chemical Society, 2010, 132(27): 9274-9276.

[154] Stankovich S, Dikin D A, Dommett G H, Kohlhaas K M, Zimney E J, Stach E A, Piner R D, Nguyen S T, and Ruoff R S. Graphene-based composite materials. Nature, 2006, 442(7100): 282-286.

[155] Kim J, Cote L J, Kim F, Yuan W, Shull K R, and Huang J. Graphene oxide sheets at interfaces. Journal of the American Chemical Society, 2010, 132(23): 8180-8186.

[156] Ye W W, Shi J Y, Chan C Y, Zhang Y, and Yang M. A nanoporous membrane based impedance sensing platform for DNA sensing with gold nanoparticle amplification. Sensors and Actuators B: Chemical, 2014, 193: 877-882.

[157] Krishnamoorthy K, Mohan R, and Kim S J. Graphene oxide as a photocatalytic material. Applied Physics Letters, 2011, 98(24): 244101.

[158] Chen S, and Barbieri J T. Association of botulinum neurotoxin serotype A light chain with plasma membrane-bound SNAP-25. Journal of Biological Chemistry, 2011, 286(17): 15067-15072.

[159] Loh K P, Bao Q, Eda G, and Chhowalla M. Graphene oxide as a chemically tunable platform for optical applications. Nature Chemistry, 2010, 2(12): 1015-1024.

[160] Zhu S, Zhang J, Liu X, Li B, Wang X, Tang S, Meng Q, …and Yang B. Graphene quantum dots with controllable surface oxidation, tunable fluorescence and up-conversion emission. Rsc Advances, 2012, 2(7): 2717-2720.

[161] Feng L, Tang X Y, Zhong Y X, Liu Y W, Song X H, Deng S L, Xie S Y, Yan J W, and Zheng L S. Ultra-bright alkylated graphene quantum dots. Nanoscale, 2014, 6(21): 12635-12643.

[162] Yang R, Jin J, Chen Y, Shao N, Kang H, Xiao Z, Tang Z, Wu Y, Zhu Z, and Tan W. Carbon nanotube-quenched fluorescent oligonucleotides: probes that fluoresce

upon hybridization. Journal of the American Chemical Society, 2008, 130(26): 8351-8358.

[163] Tao Y, Lin Y, Huang Z, Ren J, and Qu X. DNA-templated silver nanoclusters–graphene oxide nanohybrid materials: a platform for label-free and sensitive fluorescence turn-on detection of multiple nucleic acid targets. Analyst, 2012, 137(11): 2588-2592.

[164] Konkena B, and Vasudevan S. Understanding Aqueous Dispersibility of graphene oxide and reduced graphene oxide through pK a measurements. The Journal of Physical Chemistry Letters, 2012, 3(7): 867-872.

[165] Feltrup T M, and Singh B R. Development of a fluorescence internal quenching correction factor to correct botulinum neurotoxin type A endopeptidase kinetics using SNAPtide. Analytical Chemistry, 2012, 84(24): 10549-10553.

[166] Frisk M L, Lin G, Johnson E A, and Beebe D J. Synaptotagmin II peptide-bead conjugate for botulinum toxin enrichment and detection in microchannels. Biosensors and Bioelectronics, 2011, 26(5): 1929-1935.

[167] Shu P, Gao Y, Li Y, Liu S, and Su X. A novel sensing strategy for the detection of Staphylococcus aureusDNA by using a graphene oxide-basedfluorescent probe, Analyst, 2013, 138: 2749.

[168] Hyunmin C, Jung J, and Chung B H. Scanometric analysis of DNA microarrays using DNA intercalator-conjugated gold nanoparticles, Chemical Communications, 2012, 48:7601–7603.

[169] Anger P, Bharadwaj P, and Novotny L. Enhancement and quenching of single-molecule fluorescence. Physical Review Letters, 2006, 96(11): 113002.

[170] Kühn S, Håkanson U, Rogobete L, and Sandoghdar V. Enhancement of single-molecule fluorescence using a gold nanoparticle as an optical nanoantenna. Physical Review Letters, 2006, 97(1): 017402.

[171] Mayilo S, Kloster M A, Wunderlich M, Lutich A, Klar T A, Nichtl A, Kurzinger K, Stefani F D, and Feldmann J. Long-range fluorescence quenching by gold nanoparticles in a sandwich immunoassay for cardiac troponin T. Nano Letters, 2009, 9(12): 4558-4563.

[172] Li L L, Ji J, Fei R, Wang C Z, Lu Q, Zhang J R, Jiang L P, and Zhu J J. A facile microwave avenue to electrochemiluminescent two-color graphene quantum dots. Advanced Functional Materials, 2012, 22(14): 2971-2979.

[173] Zhang Y, Zhang J, Huang X, Zhou X, Wu H, and Guo S. Assembly of graphene oxide–enzyme conjugates through hydrophobic interaction. Small, 2012, 8(1): 154-159.

[174] Lee D Y, Khatun Z, Lee J H, Lee Y K, and In I. Blood compatible graphene/heparin conjugate through noncovalent chemistry. Biomacromolecules, 2011, 12(2): 336-341.

[175] De M, Chou S S, and Dravid V P. Graphene oxide as an enzyme inhibitor: modulation of activity of α-chymotrypsin. Journal of the American Chemical Society, 2011, 133(44): 17524-17527.

[176] Rajesh C, Majumder C, Mizuseki H, and Kawazoe Y. A theoretical study on the interaction of aromatic amino acids with graphene and single walled carbon nanotube. The Journal of Chemical Physics, 2009, 130(12): 124911.

[177] Zuo G, Zhou X, Huang Q, Fang H, and Zhou R. Adsorption of villin headpiece onto graphene, carbon nanotube, and C60: effect of contacting surface curvatures on binding affinity. The Journal of Physical Chemistry C, 2011, 115(47): 23323-23328.

[178] Alwarappan S, Boyapalle S, Kumar A, Li C Z, Mohapatra S. Comparative study of single-, few-, and multilayered graphene toward enzyme conjugation and electrochemical response. The Journal of Physical Chemistry C, 2012, 116: 6556-6559.

[179] Squire P G, Moser P, and O'Konski C T. Hydrodynamic properties of bovine serum albumin monomer and dimer. Biochemistry, 1968, 7(12): 4261-4272.